

Cancer Therapy Optimization based on Unsupervised Learning and Multiple Model Adaptive Control

Francisco Manuel Ferreira Teles

Thesis to obtain the Master of Science Degree in
Electrical and Computer Engineering

Supervisor(s): Prof. João Manuel Lage de Miranda Lemos

Examination Committee

Chairperson: Prof. João Fernando Cardoso Silva Sequeira

Supervisor: Prof. João Manuel Lage de Miranda Lemos

Members of the Committe: Prof. Susana de Almeida Mendes Vinga Martins

November 2017

Keep your eyes on the stars, and your feet on the ground.

Theodore Roosevelt

Acknowledgments

Acknowledgments are always a tough and, perhaps, an ungrateful decision since several people and institutions contributed to my dissertation in a direct or indirect way. However, I am going to thank the ones that had the biggest impact during the last months. To the others not mentioned below I want also to express my heartfelt gratitude.

First and foremost, I would like to thank my supervisor Professor João Miranda Lemos for all his availability, assistance and guidance, not only during the last semester but since the day I showed interest in the topic of this work. Professor João, unquestionably, is the mind behind all the ideas developed in this dissertation due to his wise advices, tips and constant questions.

Secondly, I want to express my thankfulness to INESC-ID, for the full access to its facilities where most of this work was elaborated, and to the PERSEIDS project, where this work is inserted, especially to Prof. Susana Vinga (IDMEC) for her revision of the intermediate report and posterior advices, and to Prof. Irina Alho (IMM) and Prof. Julie Chesné (IMM) for their initial clarifications and knowledge transfer.

Last but not least, I want to give a special thanks to my family for making the last five years a huge opportunity and one of the greatest periods of time of my life. Aside from that, a special word for my friends and colleagues for supporting and encouraging me, in particular to Rui and Pedro.

The work of this dissertation was performed within the framework of the project PERSEIDS, Personalizing cancer therapy through integrated modeling and decision, financed by FCT under contract PTDC/EMS-SIS/0642/2014.

Abstract

During the last years several clinical decision support systems have been developed, some of which with clearly improved efficiency. However, this kind of decision computing process has not been quite explored in cancer treatment. In this work a control system that designs an optimal therapy based on adaptive control methods, allowing the eradication of a metastatic renal cell carcinoma as quickly and efficiently as possible and with lower associated toxicity, is developed.

In order to do so, a new mathematical model describing the growth of this kind of tumor is developed, taking into account the effects of two of the most promising therapies: anti-angiogenesis and immunotherapy. Additionally, models describing pharmacodynamical aspects of the organism are also included.

The therapy is designed through multiple model adaptive control. Together with a system of selection and aggregation of key classes of models, it allows to deal with the uncertainty associated with the patient, namely his intra and inter variability.

The results demonstrate that the built system presents robustness in terms of stability and performance. The reference following errors for the simulations are around 3 %, which allows a tumor eradication in less than a year and a half with mild and moderate toxicity levels.

Therefore, the tool developed allows to create new perspectives in the creation of decision support systems for cancer therapy, thus enhancing the medical choices.

Keywords

Cancer Therapy Design; Tumor Growth Model; Anti-angiogenesis; Immunotherapy; Multiple Model Adaptive Control; Model Clustering

Resumo

Nos últimos anos, vários sistemas de suporte à decisão clínica têm sido desenvolvidos, apresentando alguns deles uma clara melhoria de resultados. No entanto, este tipo de processo computarizado de decisão não tem sido muito explorado no tratamento do cancro. Neste trabalho, pretende-se desenvolver um sistema de controlo adaptativo, que projecte uma terapia óptima, permitindo a erradicação do cancro de carcinoma metastático de células renais, da forma mais rápida e eficiente possível e com menor toxicidade associada.

Para tal, um novo modelo matemático que descreve o crescimento deste tipo de tumor é desenvolvido, tendo em conta os efeitos de duas das mais promissoras terapias: anti-angiogénese e imunoterapia. Para além disso, modelos que descrevem aspectos farmacodinâmicos do organismo são também incluídos.

A terapia é projectada através de controlo adaptativo por múltiplos modelos que, juntamente com um sistema de selecção e agregação de classes chave de modelos, permite lidar com a incerteza associada ao paciente, nomeadamente à sua intra e inter variabilidade.

Os resultados demonstram que o sistema construído apresenta robustez em termos de estabilidade e desempenho. Os erros de seguimento de referência para as simulações efectuadas situam-se nos 3 %, o que permite uma erradicação do tumor em menos de um ano e meio e com níveis de toxicidade suaves ou moderados.

Desta forma, a ferramenta desenvolvida permite criar novas perspectivas na criação de sistemas de suporte de decisão para tratamento de cancro, potenciando assim as escolhas médicas.

Palavras Chave

Design de Terapias de Cancro; Modelo de Crescimento do Tumor; Anti-Angiogénese; Imunoterapia; Controlo Adaptativo por Múltiplos Modelos; Agregação de Modelos

Contents

1	Introduction	1
1.1	Motivation	2
1.2	Literature Review	2
1.3	Objectives and Main Contribution	4
1.4	Thesis Outline	5
2	A Tumor Model for Anti-Angiogenesis and Immunotherapy	7
2.1	Cancer Therapies Review	8
2.1.1	Immunotherapy	8
2.1.2	Anti-Angiogenesis	9
2.2	Tumor Growth and Immune System Model	10
2.2.1	Tumor Model for Anti-Angiogenesis Therapy	10
2.2.2	Tumor Model for Immunotherapy	12
2.2.3	General Tumor Model	12
2.3	General Tumor Model Simulations	13
2.4	Linearization and Trajectory Analysis	16
3	Pharmacodynamical Model	19
3.1	Pharmacokinetics	20
3.2	Pharmacodynamics	22
3.3	Drug Resistance	23
3.4	Toxicity	25
4	Patient Model	27
4.1	Summary of Patient Model	28
4.2	Patient Model Simulations	28
4.2.1	Intravenous (IV) Bolus Therapy	28
4.2.2	Effect of Dose	30
4.2.3	Effect of Drug Sensitivities η and κ	32
4.2.4	Effect of Periodicities d_g and d_i	33
4.2.5	Effect of Therapy Duration T	34

5 Controller Design for a Patient Model	35
5.1 Controller	36
5.1.1 Controllability and Observability	36
5.1.2 Controller Implementation	37
5.2 Pharmacodynamical Simulation	39
6 Multiple Model Adaptive Control	41
6.1 Architecture of Multiple Model Adaptive Control (MMAC)	43
6.2 Supervisor	44
6.2.1 Observer Bank	44
6.2.2 Filter Bank	44
6.2.3 Decision Logic	45
6.3 Controller Bank	47
6.3.1 Bumpless Transfer and Anti-Windup	47
6.3.2 Mean Filter	50
7 Model Clustering	51
7.1 Model Sensitivity Analysis	53
7.2 Vinnicombe Metric	54
7.3 Clustering Methods	55
7.3.1 Intuitive Clustering	55
7.3.2 <i>K</i> -Means	56
7.3.3 Complete Linkage	56
7.4 Results	57
8 Offline Bolus Therapy Design	61
9 Results and Simulations	65
9.1 Test A – Model Switch	66
9.1.1 Bolus Computation	70
9.1.2 Dwell Time Variation	71
9.1.3 Pharmacodynamical Simulation Error Variation	71
9.1.4 Noise and Disturbance Variation	72
9.2 Test B – Model Linear Time Varying	73
9.2.1 Bolus Computation	77
9.2.2 Dwell Time Variation	77
9.2.3 Pharmacodynamical Simulation Error Variation	78
9.2.4 Noise and Disturbance Variation	78
9.3 Test C – Model Non-Linear Time Varying	79
9.3.1 Bolus Computation	83
9.3.2 Dwell Time Variation	83

9.3.3	Pharmacodynamical Simulation Error Variation	84
9.3.4	Noise and Disturbance Variation	84
10	Conclusions and Future Work	87
10.1	Work and results analysis	88
10.2	Future Work	89
Bibliography		91
Appendix A	Approximation of Patient Model to Metastatic Renal Cell Carcinoma	A-1

List of Figures

2.2	Tumor model simulations for different initial conditions.	14
2.3	Summary of tumor volume growth for different values of V_0 and K_0 and $I_0 = 0.1$. Following the arrow direction, the values used in the simulation are: $(V_0, K_0) = (1000, 2000), (3000, 4000), (5000, 6000), (8000, 9000), (10000, 11000) \text{ mm}^3$	15
2.4	Summary of tumor volume growth for $V_0 = 4000 \text{ mm}^3$ and $K_0 = 4000 \text{ mm}^3$ and different values of I_0 . Following the arrow direction, the values used in the simulation are: $I_0 = 0.1, 0.3, 0.5, 0.7, 0.9, 1.4$	15
2.5	Behavior of the non-linear (NL) and linearized (L) systems for the equilibrium point. Test 1 is realized for $u = (0, 0)$, test 2 for $u = (0.1, 0.1)$ and test 3 for $u = (0.2, 0.2)$	17
2.6	Phase portrait of tumor dynamical system.	17
2.7	Eigenvectors of the linearized system plotted in x_{eq}	18
3.1	Two-compartment Pharmacokinetics (PK) model.	20
3.2	Drug concentration in the main compartment for a combined bolus of 15 mg/kg of bevacizumab and 15 mg/kg of atezolizumab, using equation (3.3).	22
3.3	Drug effect depending on drug concentration, according to (3.6).	23
3.4	Period of time (blue area) in which resistance is developed. Concentration threshold level with value $L_r = 4 \text{ mg/kg}$	24
3.6	Toxicity levels for bevacizumab, T_g , and atezolizumab, T_i . The blue and red marks are representing the drug concentration for which toxicity level is maximum (grade 5).	25
5.1	Controller architecture for a patient model.	36
5.2	Controller scheme.	37
5.3	Composition of the Pharmacodynamical Simulation and Patient Model blocks.	39
5.4	Composition of the Pharmacodynamical Simulation and Patient Model blocks with PK Control simplification.	40
6.1	Representation in the parameter space S of the parameters vectors $\hat{p}_i, \hat{p}_j, \hat{p}_k$, and p	43
6.2	Simplified architecture of the MMAC.	43
6.3	Architecture of the supervisor in the MMAC.	44
6.4	Correspondence between the prediction error \hat{e}_i and its filtration π_i	45
6.5	Computer diagram of the decision logic sequential process.	46

6.6	Architecture of the controller bank in the MMAC.	47
6.7	Illustrative example of a windup situation.	48
6.8	Architecture of the bumpless transfer scheme combined with anti-windup.	49
6.9	Illustration of the effect of the variable T_w in the anti-windup system.	49
6.10	Example of the bumpless transfer and anti-windup system operation.	50
6.11	Example of mean filtration for a sampling time of $t_s = 0.3$ days.	50
7.1	Clustering illustration for a set of models M_i – blue dots – resulting in five clusters M_j^c – red crosses.	52
7.2	Sensitivity of the model as a function of time, for $V_0 = 28000.4$ mm ³ , $K_0 = 29528.1$ mm ³ , $I_0 = 0.013$ and $u_0 = (0, 0)$.	54
7.3	Clustering of 100 different models into 6 clusters using 3 different methods.	58
7.4	Clustering of 100 different models into 12 clusters using 3 different methods.	60
8.1	State space representation of the linear PK model, having as input a set of N_b bolus.	62
8.2	Offline design of a bolus therapy for a constant reference and $d_g = 21$ days.	63
9.1	Partition of the model data set according to the four methods – Test A.	67
9.2	Simulation of the MMAC algorithm using the k -means with 6 clusters – Test A.	68
9.3	Simulation of the MMAC algorithm using the complete linkage with 6 clusters – Test A.	68
9.4	Simulation of the MMAC algorithm using the k -means with 12 clusters – Test A.	69
9.5	Simulation of the MMAC algorithm using the complete linkage with 12 clusters – Test A.	69
9.6	Designed bolus therapy for $C_g(t)$ with $d_g = 21$ days and $C_i(t)$ with $d_i = 7$ days – Test A.	70
9.7	Selected patient dynamics depending on the value of the dwell time τ_D – Test A.	71
9.8	Drug concentration and toxicity level of therapies computed for different values of $\Delta\theta_{PS}$ – Test A. The dashed curves in the left plot represent $C_i(t)$ and the solid curves $C_g(t)$.	72
9.9	Selected patient dynamics for the three different uncertain situations – Test A.	73
9.10	Partition of the model data set according to the four methods – Test B.	74
9.11	Simulation of the MMAC algorithm using the k -means with 6 clusters – Test B.	75
9.12	Simulation of the MMAC algorithm using the complete linkage with 6 clusters – Test B.	75
9.13	Simulation of the MMAC algorithm using the k -means with 12 clusters – Test B.	76
9.14	Simulation of the MMAC algorithm using the complete linkage with 12 clusters – Test B.	76
9.15	Designed bolus therapy for $C_g(t)$ with $d_g = 21$ days and $C_i(t)$ with $d_i = 7$ days.	77
9.16	Selected patient dynamics depending on the value of the dwell time τ_D – Test B.	78
9.17	Drug concentration and toxicity level of therapies computed for different values of $\Delta\theta_{PS}$ – Test B. The dashed curves in the left plot represent $C_i(t)$ and the solid curves $C_g(t)$.	78
9.18	Selected patient dynamics for the three different uncertain situations – Test B.	79
9.19	Partition of the model data set according to the four methods – Test C.	80
9.20	Simulation of the MMAC algorithm using the k -means with 6 clusters – Test C.	81
9.21	Simulation of the MMAC algorithm using the complete linkage with 6 clusters – Test C.	81

9.22 Simulation of the MMAC algorithm using the k -means with 12 clusters – Test C.	82
9.23 Simulation of the MMAC algorithm using the complete linkage with 12 clusters – Test C. .	82
9.24 Designed bolus therapy for $C_g(t)$ with $d_g = 21$ days and $C_i(t)$ with $d_i = 7$ days – Test C. .	83
9.25 Selected patient dynamics depending on the value of the dwell time τ_D – Test C.	83
9.26 Drug concentration and toxicity level of therapies computed for different values of $\Delta\theta_{PS}$ – Test C. The dashed curves in the left plot represent $C_i(t)$ and the solid curves $C_g(t)$. . .	84
9.27 Selected patient dynamics for the three different uncertain situations – Test C.	85
A.1 Tumor behavior window for $V_0 = 5000$ mm ³ . Maximum curve with a fit.	A-2

List of Tables

2.1	Constant terms of general tumor model composed by equations (2.7), (2.8) and (2.9). . .	13
3.1	Pharmacokinetics parameters for bevacizumab and atezolizumab.	21
3.2	Pharmacodynamics parameters for bevacizumab and atezolizumab.	22
7.1	Clustering results – number of models in each c_i , mean and worst distances of all the models to its centroid – for the three methods with $N_c = 6$ clusters. Last row shows the sum of models and the mean value of the Mean d_c and Worst d_c	59
7.2	Clustering results – number of models in each c_i , mean and worst distances of all the models to its centroid – for the three methods with $N_c = 12$ clusters. Last row shows the sum of models and the mean value of the Mean d_c and Worst d_c	59
9.1	Evaluation metrics for the designed bolus therapies – Test A.	70
9.2	Evaluation metrics for all the simulations performed in Test A.	73
9.3	Evaluation metrics for the designed bolus therapies – Test B.	77
9.4	Evaluation metrics for all the simulations performed in Test B.	79
9.5	Evaluation metrics for the designed bolus therapies – Test C.	83
9.6	Evaluation metrics for all the simulations performed in Test C.	85
A.1	Values of the tumor's initial volume and volume growth.	A-3
A.2	Values of the diameter variation for patients with the best and the worst tumor response with the respective time instants.	A-3

Abbreviations

WHO World Health Organization

TMT Targeted Molecular Therapy

PD Pharmacodynamics

DR Drug Resistance

PK Pharmacokinetics

MMAC Multiple Model Adaptive Control

LQG Linear Quadratic Gaussian

CDSS Computer-Based Clinical Decision Support System

IS Immune System

CTLA-4 Cytotoxic T-Lymphocyte-Associated Antigen 4

PD-1 Programmed Death 1

VEGF Vascular Endothelial Growth Factor

mRCC Metastatic Renal Cell Carcinoma

VHL Von Hippel-Lindau

IV Intravenous

CIT Constant Infusion Therapy

PO Oral Administration

CTCAE Common Terminology Criteria for Adverse Events

LQR Linear Quadratic Regulator

MAPE Mean Absolute Percentage Error

1

Introduction

Contents

1.1 Motivation	2
1.2 Literature Review	2
1.3 Objectives and Main Contribution	4
1.4 Thesis Outline	5

1.1 Motivation

Cancer is one of the most predominant causes of death with 14 million new cases globally, claiming 8.2 million lives yearly, as of 2012 [1]. If cancer-specific and sex-specific trends continue, an increase in the incidence of all-cancer cases by around 60%, will have reached 22.2 million cases in 2030, as predicted in [2]. This number can grow due to the aging and growth of the world population alongside with the adoption of unhealthy behaviors. This means that in the next few decades cancer is set to become the major cause of morbidity and mortality independently of the world region and level of resources [3].

A substantial part of the worldwide cancer cases can be prevented, according to the World Health Organization (WHO), through four key strategies [4]: modifying and avoiding risk factors, that can decrease death rate up to 30 %; early detection, preventing tumors from becoming malignant; effective treatments, that can cure cancer or prolong patient's life; and palliative care, allowing patients to relieve the suffering from symptoms caused by cancer.

The last fifteen years have seen remarkable progress in prevention, diagnosis and treatment of cancer, aided by technological advances and innovative research [5]. For example, due to large-scale collaborative projects and initiatives, we now have a much better understanding of genes and molecular pathways that are altered in cancer. Recent technological and scientific advancements have brought about plenty of innovative treatments, such as the Targeted Molecular Therapy (TMT) and immunotherapy, whose promising results are making these therapies to be seen as progress in the conventional treatments (surgery, radiotherapy and chemotherapy) [6–8].

Nevertheless, one of the biggest problems remains: how to find the right treatment that can destroy a tumor in an efficient and effective way in the shortest period possible and with the least impact on patient's life. This constitutes a strong motivation for the research and development of optimized cancer therapies using methods from control theory and clustering algorithms from unsupervised learning.

1.2 Literature Review

During the last decades, the scientific community has learned a lot from biological and natural systems, using that knowledge to develop new robust algorithms to solve complex problems, resulting in one of the most promising scientific topics, the so-called "intelligent systems" [9]. Successful solutions have been achieved in a wide variety of areas, like power flow optimization [10], review rating prediction in e-commerce [11], immune system characterization [12] or the diagnosis of diabetic patients [13].

Intelligent systems must make optimal decisions by evaluating the imposed restrictions and the attributed main goals, selecting one way in detriment of the others hypothesis. Living systems have exactly the same behavior by applying the principles of survival and selection of the theory of evolution and eliminating the weakest solutions [14]. Therefore, intelligence is a property of the computer aided decision makers or decision support systems, that complement the human thought process in solving

complex problems.

Automated decision makers or helpers are system-engineering tools that tend to make optimal decisions, taking into account the criteria and the parameterization of the problem. These tools have been widely used [15] to achieve considerable advancements in terms of quality and efficiency of products and services, particularly in uncertain environments with huge volumes of data. As an example, decision maker software has been developed for portfolio optimization [16] to maximize returns, for an automatic elaboration of hurricane mitigation plans [17], or for an automated selection of structural materials in the construction industry [18].

In the health care sector this digital transformation is happening slowly [15], although it has been shown to yield added value for health organizations [19, 20]. Aside from that, since the 90s it has been strongly believed that information and decision technologies are going to promote a better performance in the standards of care [21].

Some Computer-Based Clinical Decision Support Systems (CDSSs) have been successfully tested and implemented leading to an improvement of clinical decisions, as indicates an article from 1998 [22], showing that from 18 different studies of computerized drug dosing only 2 not keep or improved the health care practitioner performance. Another CDSSs review from 2005 [23] shows also that 62 % of the CDSSs studies related to single-drug dosing improved practitioner performance and some of them resulted in better patient outcomes. Notice that none of those studies are related to oncology.

There is a huge variety of factors that are challenging decision making along the cancer continuum, particularly in cancer treatment design. Therapy decisions are arduous not only because of the uncertainty associated with its effectiveness but also due to the possible negative outcomes that can arise for patients. Therefore, there are emotional factors and cognitive barriers that are limiting the implementation of CDSSs for cancer therapy design [24]. Nevertheless, some CDSSs have been implemented, like *CATIPO* [25], a system that through acquiring knowledge about chemotherapy protocols can produce customized therapy plans for children. Tools supporting decision making are also available, for instance *FabAct* [26], that helps the user by selecting the most appropriate chemotherapy anti-cancer drugs, or *LISA* [27] that assists the choice of drug dosage in acute lymphoblastic leukemia by facilitating access to blood information.

Apart from the clinical experiments mentioned above, the scientific community has been creating and developing algorithms for optimizing cancer therapies. High costs, long trial times, difficulty in multiple hypothesis testing and ethical barriers make the feasibility of clinical trials, for testing different approaches and finding the optimal, an expensive and ineffective solution [28]. Therefore, mathematical modeling is an economical and powerful way of testing hypothesis and confirming therapies effects. Not only does it simulate the behavior of such complex systems, like tumor growth, Pharmacokinetics (PK), Pharmacodynamics (PD) and Drug Resistance (DR), but also and most importantly their interactions.

Many tumor growth models have been developed in depth in order to incorporate all the biomedical phenomena and approximate them as much as possible to reality. Exponential linear models are the simplest approaches to tumor growth [29]. After that, logistic [30] and Gompertz [31] models were

introduced, by considering tumor growth with a sigmoid shape. Taking the next step up into complexity, a dynamic carrying capacity model appears [32], representing tumor vasculature. Another known model is the one from Von Bertalanffy that derives organic growth laws from basic principles of energy [33]. Besides that, different approaches have been made, e.g. considering the angiogenesis process [34, 35], apoptosis phenomena [36], immunotherapy [37] or three dimensional cellular automaton [38].

Empirical linear and non-linear models have been developed [39] for describing PK behavior, as well as other models using image processing [40]. Concerning PD models, since the basic Hill equation [41], other modulations have been made, especially considering signal transduction systems [42]. DR plays also an important role in the systematization of tumor behavior, being mathematically represented by different models with distinctive considerations, as for example in [43, 44].

Model based dynamics optimization or optimal control has been used in order to solve tumor eradication problems, using distinct techniques. For example, the optimal control study from Swan *et al.* [45] is critical for the understanding of the early modeling approaches for chemotherapy. Aside from that, Schättler *et al.* [46] applied geometrical optimal control to challenging problems. Subsequently, the same techniques were applied to a problem where a balance between cell kill and toxicity level was considered [47]. In [48], solutions are found using optimal control with different cost functions and also receding horizon control. Several other techniques are used such as model predictive control [49, 50], or model reference adaptive control [51].

To the best of the author's knowledge, there is no study approaching therapy optimization problem with Multiple Model Adaptive Control (MMAC), despite the fact that this control technique is used in several areas. Due to its robust performance, MMAC is a strategy that is used, as an example, for the control of blood pressure [52, 53], neuromuscular blockade [54–56], aircraft flight [57] or power systems [58].

Furthermore, MMAC combined with model clustering for finding a finite set of models that cover system dynamics is a technique that was used in [58]. A dynamic finite set of models has also been considered as for example using self-organizing map neural networks [59] or set-valued observers [60].

1.3 Objectives and Main Contribution

The objective of this dissertation is to develop a control based framework to design therapies for reducing tumor volume, optimizing and personalizing therapeutic, while minimizing toxic effects.

A tumor growth model is developed, using Metastatic Renal Cell Carcinoma (mRCC) clinical results, through a combination of two different treatments: anti-angiogenesis and immunotherapy. This model considers the tumor volume V to be dependent of the input drug effect u .

In addition to the tumor growth model, a PD and a DR models are also going to be developed in order to assess the relation between the drug effect u and the drug concentration in the patient's body C_p . Finally, in order to complete the patient model considered in this dissertation, PK, the relation

between the concentration C_p and an administered drug dose D , is included.

The way the patient is going to react to a treatment, what kind of resistance the organism is going to show or how developed the tumor is, are variables that cannot be predicted by any doctor, since the characteristics of the patient, not only before the beginning of the therapy, but also during its course, are unknown. In this way, inter and intra-patient variability is going to be taken into account by using MMAC, a control technique in which an optimal therapy is being constantly chosen by selecting, for each time t , from a large variety of models the one that, simultaneously, best fits the unknown patient model and has the lowest toxicity level. The optimal control problem for each possible linearized model is solved using the Linear Quadratic Gaussian (LQG).

Finally, for making this project scalable, *i.e.* to allow the selection of any positive number of models, unsupervised learning in the form of clustering is going to be used to agglomerate patient models that are similar. This objective implies a constant number of controllers regardless of the number of patient models.

To conclude, the main contribution of this dissertation consists of a simulation of a tool for clinical decision-making in cancer therapy design, using adaptive control techniques. An article was also submitted in the journal *Biomedical Signal Processing and Control*.

1.4 Thesis Outline

In this section, an introduction to the topic that is going to be approached in the following chapters was performed, including the motivation for this work, a review of the previous contributions, and the main objectives of this dissertation.

In Chapter 2, a new tumor growth model is built, considering a multi-drug administration with anti-angiogenesis and immunotherapy.

In Chapter 3, a summary of the pharmacodynamical models used is performed, comprising PK, PD, DR and toxicity.

Chapter 4 describes the patient model used in this work, by joining the tumor growth and the pharmacodynamical models. Apart from that, several tests are made.

In Chapter 5, a controller is developed to efficiently design a therapy for a fully known patient model.

Chapter 6 adapts the previous control framework to deal with the uncertainty in the patient model. For that, an algorithm of MMAC is used.

In Chapter 7, a clustering algorithm is added to the previous established MMAC approach, for choosing from a data set the best sample of models.

In Chapter 8, an offline bolus therapy system is established.

Chapter 9 summarizes the simulations performed. The results are presented and discussed.

In Chapter 10, the final conclusions are described as well as the topics that may be interesting to discuss in the future.

2

A Tumor Model for Anti-Angiogenesis and Immunotherapy

Contents

2.1 Cancer Therapies Review	8
2.2 Tumor Growth and Immune System Model	10
2.3 General Tumor Model Simulations	13
2.4 Linearization and Trajectory Analysis	16

2.1 Cancer Therapies Review

Despite the large investments in research, finding the right treatment that can cure cancer still continues to be a complex problem mainly because of two reasons that can be considered life hallmarks: selection and variation. Since every patient is different, even within homogeneous histological groups, and cancer can be in several particular growth phases as well as it can be composed by cells with a plenty of mutations types, it is an arduous job to predict the entire disease and act against it.

Another disadvantage is the cancer evolution over time. An initial prognosis and adjusted treatment can be extremely accurate at the beginning but cancer in a short period can become resistant to it. This global cancer capability is called "tumor progression" [61] and constitutes the biggest challenge of tumor right prognosis and implementation of effective therapies, as well as the reason of all research efforts in understanding cancer development.

Targeted Molecular Therapy (TMT) [62] is a modern and innovative therapy that combat cancer, not acting directly against mutant cells and inhibiting cell division, but by understanding cancer pathological processes and mechanisms and stimulating or blocking it. In this way, the actions performed and toxicities of TMTs differ from those used by the classic cytotoxic therapies.

Anti-angiogenesis and some kinds of immunotherapy are different types of TMTs that are considered in the tumor model of this work.

2.1.1 Immunotherapy

The Immune System (IS) is the first internal mechanism to respond against tumor cells. The IS aims at discriminating between self and exogenous body agents, and once detected, to neutralize possible threats. It includes an innate IS composed by cells that are immediately available to combat a wide range of pathogens, and an adaptive IS that results from a production of antibodies against a particular pathogen inducing an adaptation to infection. Both systems together provide a remarkably effective defense system. Tumor cells are mainly fought by the adaptive IS, since it is not a usual pathogen [63].

Immune responses depend upon lymphocytes, originated in bone marrow, which for innate IS include natural killer cells and for adaptive IS consist of T and B cells that provide the lifelong immunity that can follow exposure to different antigens. Mature T and B lymphocytes circulate in the blood or in the lymphatic system and when facing some antigen, B cells become antibody-secreting plasma cells, whereas T cells differentiate into effector T cells with a variety of defense roles. Effector T cells are the main responsible for fighting tumor cells [64].

For a better understanding of the key steps in antitumor immune response, Chen and Mellman developed a "cancer-immunity cycle" [65] – Figure 2.1. Dendritic cells are responsible for initiating this cycle, generating anticancer T cells responses by capturing tumor antigens. This acquisition process induces the activation of dendritic cells that lead them to travel to tumor-draining lymph nodes, where naïve T cells are primed to become effector T cells. T cells, after the traffic and infiltration through lymph nodes, can kill tumor cells. The death of the malign cells can trigger additional antigen detection

and then cancer-immunity cycle is restarted.

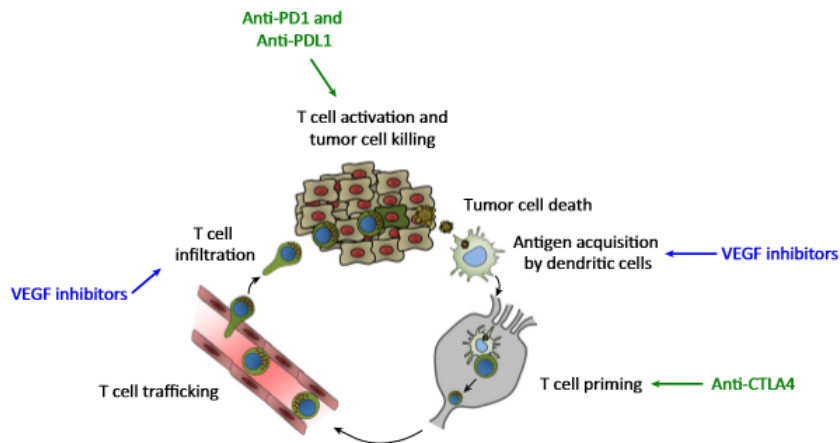


Figure 2.1: Illustration of cancer-immunity cycle. The green text represents the effect of T cell checkpoint therapies and the blue text VEGF inhibitors. Adapted from [66].

However, to prevent autoimmunity, several regulatory molecules or checkpoint pathways control T cells activation during immune response. This is a process known as peripheral tolerance, and it limits the IS capacity. Cytotoxic T-Lymphocyte-Associated Antigen 4 (CTLA-4) and Programmed Death 1 (PD-1) are the most important checkpoint pathways existing in the IS, however, playing different roles. CTLA-4 plays an important role in the priming phase, regulating naïve T cells activation. PD-1 manage pre-activated T cells found in the micro environment.

Immunotherapy has become an important way of fighting certain kinds of cancer, particularly melanoma, prostate, kidney and colorectal cancer [67].

Non-specific immunotherapies help IS fighting cancer by acting as an immune boost for example in combination with chemotherapy. Proteins like interferons or interleukins are used as an immune boost, triggering the protective defenses of the IS and consequently eradicating pathogens.

Monoclonal antibodies form another kind of therapy that can be used as a targeted therapy to block an abnormal protein in a malign cell or to be attached to specific proteins in cancer cells. This attachment can be seen as a flag to the IS, making easier the recognition and the destroying process [68].

More recently, T cell checkpoint therapies focused on acting directly on T cell priming or activation, cancer-immunity cycle key steps, by inhibiting specific immune checkpoint pathways as the ones mentioned before. New drugs have been approved such as ipilimumab (anti-CTLA-4) and nivolumab (anti-PD-1) for melanoma cancer [69].

2.1.2 Anti-Angiogenesis

Another promising treatment is called anti-angiogenesis. Angiogenesis is the process of formation of new blood vessels from pre-existing ones. The process occurs in the tumor initial growing phase. When the vascular transition is performed, tumor cells secrete angiogenic factors, such as the Vascular Endothelial Growth Factor (VEGF) that results in the stimulation of endothelial cells present in cardiovascular system surfaces. This process facilitates cell migration and proliferation, resulting

in the creation of new blood vessels that allow nutrients and oxygen transport directly to the tumor. Several drugs that block the protein VEGF-A, critical driver of tumor angiogenesis were approved like bevacizumab or sunitinib, being used for renal cell, gynecologic or head and neck cancers [70].

A remarkable discovery was the direct influence of VEGF-A on the immune cells in an inhibitory manner, aside from its effect on vasculature [66]. VEGF-A decreases adhesion molecule expression on endothelial cells, resulting in a dysfunction in tumor vasculature and in an inhibition of immune cells infiltration into the tumor, especially T cells [71, 72]. Studies have demonstrated that low levels of T cells in tumors are related to tumor angiogenesis, dysfunctions on vasculature or elevated VEGF-A concentrations [73, 74]. Aside from that, *in vitro* studies have shown the effect of VEGF-A in the suppression of dendritic cell differentiation, increase of checkpoint molecules on CD8 T cells, and in the control of T cells proliferation [75–77].

This new finding contributed to an important conclusion: immunotherapy can be antiangiogenic and anti-angiogenesis can stimulate the immune system, leading to a possible synergy that can enhance antitumor effects [78]. Several clinical studies were performed in the last few years combining immunotherapy with anti-angiogenesis. For example, in a study of bevacizumab with ipilimumab versus ipilimumab monotherapy in metastatic melanoma, combination therapy resulted in a higher level of infiltrated immune cells in tumors [79]. The same results were obtained when bevacizumab was combined with atezolizumab (anti-PD-1) [80] and for sunitinib with nivolumab (anti-PD-1) [81]. In a combined therapy with bevacizumab and interferon alfa, progression-free survival was significantly improved compared with interferon alfa single agent therapy, resulting in its approval for mRCC [82].

Due to its distinctive features, mRCC is certainly a type of cancer where immunotherapy combined with anti-angiogenesis can result in great improvements. A disruption of the Von Hippel-Lindau (VHL) tumor-suppressor gene originates an overexpression of hypoxia-inducible proteins, as VEGF, being the tumor highly vascularized regardless of tumor size, stage or grade [83].

The problem of choosing a concurrent or sequential therapy, optimizing dosing regimens, minimizing toxicities and selecting convenient endpoints is a key consideration for clinical development of a combined therapy between anti-angiogenesis and immunotherapy. In the following chapters this problem is going to be approached using a mathematical model to describe a patient and control techniques to optimize therapies.

2.2 Tumor Growth and Immune System Model

In order to build a tumor model susceptible to anti-angiogenesis therapy and immunotherapy, two different models were combined to reproduce cancer behavior in the presence of both treatments. Both models and a general model are described in the following subsections.

2.2.1 Tumor Model for Anti-Angiogenesis Therapy

A common model used to described tumor volume growth V is the dynamic rate equation so-called Gompertz growth, given by equation (2.1). This model has been verified in the last century, not only

in laboratory, but also in clinic, particularly due to the deceleration imposed with the population size.

$$\dot{V} = -\lambda V \log \left(\frac{V}{V_{max}} \right). \quad (2.1)$$

In this equation a tumor maximum volume V_{max} is considered, achieved when all the available support is being used, which limits tumor growth capability. The parameter λ is responsible for describing the rate of the tumor growth and depends on the type of tumor.

In 1999, Hahnfeldt *et al.* [84] developed a new experimentally validated approach of vascular tumor growth that persists as a milestone in the related literature, not only due to the experimental validation, but also because of the simplicity and minimal parameterization of the model proposed.

The authors proposed that a model with Gompertzian growth may be assumed as a bidirectional process: the tumor regulates its own vascular support system whereas this vascular system controls the tumor volume through a nutritive supply. The nutrition levels in equation (2.1) are quantified in the variable V_{max} , which is the limit of tumor volume for a maximum physiological supply. However, due to proangiogenic and antiangiogenic factors possibly secreted by the tumor or imposed by a treatment, this limit can change with time. That is why a change in the Gompertz model is proposed, introducing the concept of the time-dependent variable "carrying capacity", K , that corresponds to the effective vascular support received by the tumor. Tumor growth is thus described by

$$\dot{V} = -\lambda V \log \left(\frac{V}{K} \right), \quad \dot{K} = f(K, V, t), \quad (2.2)$$

where λ has units of day^{-1} and K in mm^3 .

The function \dot{K} can be characterized as

$$\dot{K} = -\mu K + bS(K, V) - dI(V, K) - \eta Kg(t), \quad (2.3)$$

where the first term describes the spontaneous loss of functional vasculature; the second term the stimulatory effect of the tumor on the vascular system; the third term reflects the inhibitory effect due to endogenous causes; and the last one represents the external inhibition of vasculature therapy-induced by some drug administrated at the effect rate $g(t)$.

A spatial analysis of the consumption-diffusion equation for the concentration of both the stimulator and inhibitor inside and outside the tumor was also performed in [84], leading to two main conclusions: inhibitors need to be released through tumor surface, so the impact of inhibition factor on endothelial cells, and thus on the carrying capacity, is proportional to r_o^2 or $V^{\frac{2}{3}}$, since a spherical symmetry is considered; inhibition tends to be faster than stimulation, being inhibition term $V^\alpha K^\beta$ faster, with $\alpha + \beta = \frac{2}{3}$ for which Hahnfeldt *et al.* have chosen $\alpha = 1$ and $\beta = -\frac{1}{3}$. From these assumptions, the inhibitor factor can be described as $I(V, K) = KV^{\frac{2}{3}}$ and the stimulator factor as $S(V, K) = V$. Therefore, equation (2.3) can be rewritten as

$$\dot{K} = -\mu K + bV - dKV^{\frac{2}{3}} - \eta Kg(t), \quad (2.4)$$

where μ is a constant representing the loss of endothelial cells due to natural causes [in day^{-1}], sometimes neglected for its small value, b is the "birth" rate [in day^{-1}], d is the "death" rate [in $day^{-1}mm^{-2}$] and η is the anti-angiogenesis killing parameter [in $kg mg^{-1} day^{-1}$].

It is possible to see that the system composed by equations (2.2) and (2.4) is cooperative, that is, $\frac{\partial \dot{V}}{\partial K} > 0$ and $\frac{\partial \dot{K}}{\partial V} > 0$, for $V, K > 0$. This means that if K increases, V follows the same behavior. Besides that, if $K = V$ the micro environment satisfies all tumor necessities, if $K > V$ tumor is growing, since one have more nutrients to give to the tumor beyond those strictly necessary, and if $K < V$ the tumor is regressing.

2.2.2 Tumor Model for Immunotherapy

For small cancer volumes, the IS can indeed be effective in tumor eradication, but for large volumes the dynamics suppresses defense responses, rendering a cancer therapy necessary. In this way, an analysis of tumor-immune system interactions can help in understanding tumor state and how to act against it.

Several models have been developed to describe this interaction, of which Stepanova's model stands out [85]. Although originally it accounts for an exponential tumor growth, Ledzewicz *et al.* [86] adapted it into a Gompertz growth used for a combination of cancer cytotoxic chemotherapy and immunotherapy in the form of an immune boost. This model gives a relation between tumor volume V and immunocompetent cell densities I (dimensionless) relating to activities of T cells, and is given by

$$\dot{V} = -\lambda V \log \left(\frac{V}{V_{max}} \right) - \gamma VI - \rho V c(t), \quad (2.5)$$

$$\dot{I} = \mu_I (V - \beta V^2) I - \delta I + \alpha + \kappa I i(t). \quad (2.6)$$

Equation (2.5) describes tumor growth \dot{V} and has exactly the same structure of equation (2.2), with exception of the last term that describes the beneficial effect of the IS on cancer volume, being γ a constant denoting the elimination rate of cancer cells caused by the IS. Aside from that, since this model does not contemplate a varying carrying capacity, a constant value for the maximum volume V_{max} is considered.

A summary of the immune reaction \dot{I} is performed in equation (2.6). The influx rate of generated tumor cells is given by the constant α , and δ denotes the lymphocytes death rate. The first term in this equation describes the evolution of immunocompetent cells density. It takes into account that for small tumors, cells proliferation can be proportional to the tumor volume and for large tumors a suppression of immune activity can occur, described by the subtracting term. This influence is regulated by constants μ_I and β .

Finally, chemotherapy and immunotherapy are represented by the effects $c(t)$ and $i(t)$, respectively. The terms ρ and κ are constants symbolizing treatment sensibilities.

2.2.3 General Tumor Model

In order to develop a dynamic model that describes the dependency of tumor behavior on anti-angiogenesis and immunotherapy, a fusion between Hahnfeldt *et al.* and Ledzewicz *et al.* models is proposed, resulting in the following equations

$$\dot{V} = -\lambda V \log \left(\frac{V}{K} \right) - \gamma VI, \quad (2.7)$$

$$\dot{K} = -\mu K + bV - dKV^{\frac{2}{3}} - \eta Kg(t), \quad (2.8)$$

$$\dot{I} = \mu_I(V - \beta V^2)I - \delta I + \alpha + \kappa Ii(t). \quad (2.9)$$

The term corresponding to chemotherapy was removed since this kind of therapy is not being applied and a variable carrying capacity is again considered. Furthermore, the original constant terms were modified – Table 2.1 – in order to have the system following an approximation of a mRCC cancer clinical behavior (see Appendix A). Furthermore, an interval of acceptable values for therapy effect sensibilities η and κ were defined to assure that the system response to therapy is in accordance with the clinical results considered. Aside from that, a range for tumor's initial volume was defined between 0.3 and 10 cm^3 . It is worth noticing that in this model the tumor volume V represents the aggregated sum of tumors (main tumor and its metastases). Aside from that, $g(t)$ and $i(t)$ represent anti-angiogenesis and immunotherapy, respectively, as an effect, *i.e.* are between 0 and 1, where 0 means that no therapy is being applied, and 1 the maximum effect is achieved.

Table 2.1: Constant terms of general tumor model composed by equations (2.7), (2.8) and (2.9).

Constant	Value	Units
λ	0.025	day^{-1}
γ	0.1	day^{-1}
μ	0.2	day^{-1}
b	8.7	day^{-1}
d	8.73×10^{-3}	$day^{-1}mm^{-2}$
μ_I	3×10^{-5}	-
β	5×10^{-4}	-
δ	0.37451	-
α	0.15	-
η	[1.35, 11.25]	$kg/mg/day$
κ	[0.1, 0.5]	kg/mg

2.3 General Tumor Model Simulations

Model simulations were performed for different initial conditions (V_0 , K_0 and I_0) in order to evaluate model behavior in the absence of therapy – Figure 2.2.

There is an initial fast growth in curve K in all the tumor model simulations represented in Figure 2.2, due to the secretion of angiogenic factors by the tumor and therefore, a stimulation of endothelial cells. Furthermore, tumor grows depending on its carrying capacity behavior, stagnating when it achieves its maximum value, that is, when the peak of nutrients supply is reached.

This dependency of tumor volume V on carrying capacity can be also observed in equation (2.7). Since tumor growth stops when the derivative of V cancels, it is possible to express in an equation the stagnated value of tumor volume, V_s . Equating equation (2.7) to zero and after some manipulation, the following equation results

$$V_s = Ke^{-\frac{\gamma I}{\lambda}}. \quad (2.10)$$

The stagnated value of tumor volume V_s is proportional to the carrying capacity K and to another exponential term that is dependent on the immunocompetent cells density I . Since $I \in \mathbb{R}_+$, the

exponential term is always between $[0, 1]$, being the unitary value achieved when an immune system reaction does not exist, *i.e.* when $I = 0$. This means that V_s is, up to a positive constant factor less than one, always dependent on the carrying capacity K , so if a peak of nutrients supply is achieved, the tumor is going to stop its growth.

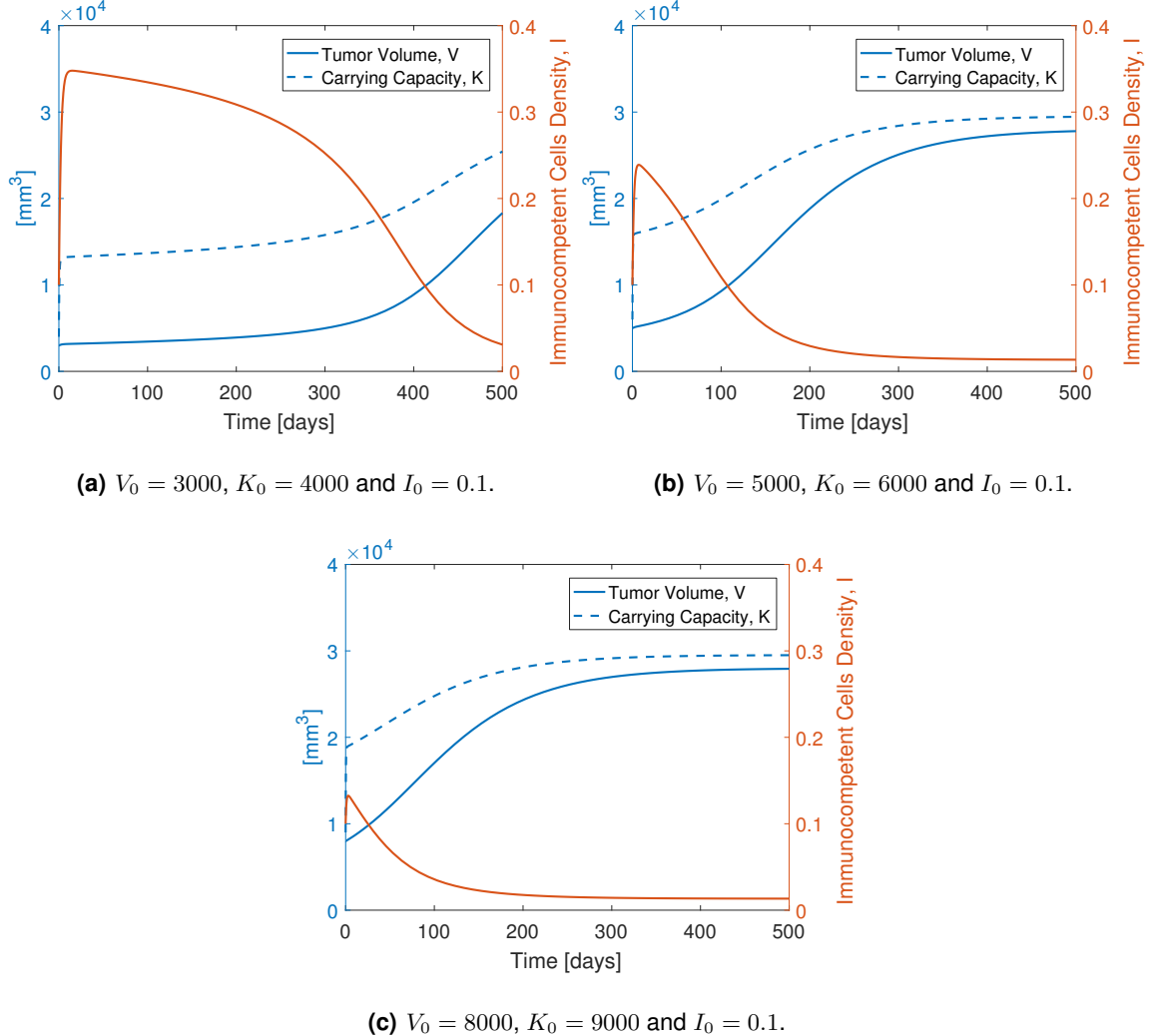


Figure 2.2: Tumor model simulations for different initial conditions.

The immunocompetent cells reaction is dependent on the initial conditions, being higher in the presence of small tumors. When tumor volume is not too large, the immune system has the capability of reacting in order to control the tumor initial growth, as it is seen in Figure 2.2(a), where during the first approximately 300 days, tumor growth is almost insignificant due to an effective reaction of the immunocompetent population. However, this reaction is not evident in Figure 2.2(b) and 2.2(c), since the tumor volume initial conditions are higher. Besides that, the steepness of the Gompertzian curve of tumor volume V depends also on the immune reaction, however, in the absence of therapy, this immune system control capacity is quickly superseded by the tumor's growth rate due to its adaptation against T cells action.

In Figure 2.3 a summary of tumor volume V growth for different initial conditions is illustrated. As

it is possible to see, only the tumor with smaller V_0 , i.e. with $V_0 = 1000 \text{ mm}^3$, can be controlled by the immune system. All the other tumors with higher initial conditions aim at the same maximum plateau, nevertheless with different growth rates.

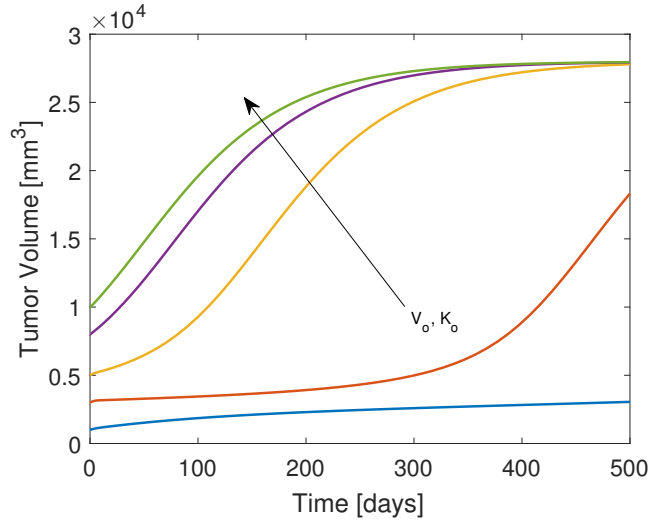


Figure 2.3: Summary of tumor volume growth for different values of V_0 and K_0 and $I_0 = 0.1$. Following the arrow direction, the values used in the simulation are: $(V_0, K_0) = (1000, 2000), (3000, 4000), (5000, 6000), (8000, 9000), (10000, 11000) \text{ mm}^3$.

The variation of I_0 influences also the way tumor grows as Figure 2.4 shows, which remains in accordance with the biological point of view: the greater the initial density of immunocompetent cells, the greater its capacity of reaction against tumor cells. However, I_0 does not influence the plateau achieved by the tumor, only the rate at which the plateau is reached.

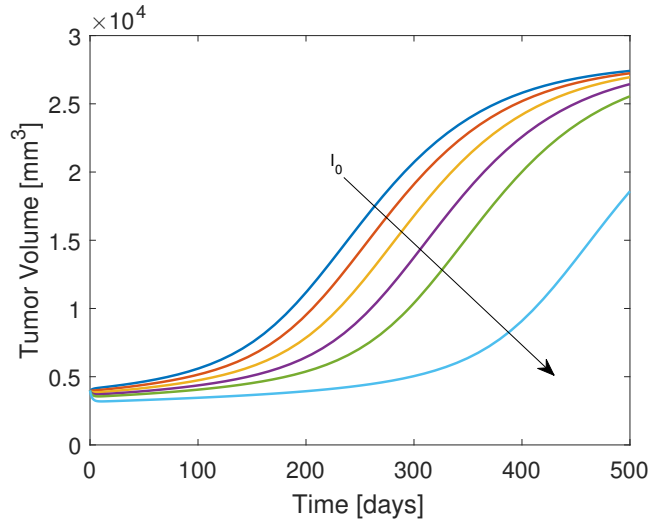


Figure 2.4: Summary of tumor volume growth for $V_0 = 4000 \text{ mm}^3$ and $K_0 = 4000 \text{ mm}^3$ and different values of I_0 . Following the arrow direction, the values used in the simulation are: $I_0 = 0.1, 0.3, 0.5, 0.7, 0.9, 1.4$.

2.4 Linearization and Trajectory Analysis

Considering that the state variables of the previously defined model can be represented as $x = [V \ K \ I]^T$ and the input rate as $u = [g \ i]^T$, the model can then be seen as

$$\dot{x} = f(x, u) . \quad (2.11)$$

In this way, the system linearization around the equilibrium point, that is, for $x_{eq} = [V_{eq} \ K_{eq} \ I_{eq}]^T$ and $u_{eq} = [g_{eq} \ i_{eq}]^T$, is given by the following linear system

$$\frac{d}{dt} \Delta x = A \Delta x + B \Delta u , \text{ where } A = \left[\frac{df}{dx} \Big|_{x=x_{eq}, u=u_{eq}} \right], B = \left[\frac{df}{du} \Big|_{x=x_{eq}, u=u_{eq}} \right] , \quad (2.12)$$

where Δx is the increment around x_{eq} and Δu around u_{eq} .

For the general tumor model described in the previous sections, the matrices A and B are given by

$$A = \begin{bmatrix} -0.1I - \mu - \mu \log(V/K) & V\mu/K \\ 8.7 - 0.0058K/V^{1/3} & -9g(t) - 0.00873V^{2/3} - 0.2 \\ -I(3 \times 10^{-8}V - 3 \times 10^{-5}) & 0 \\ & -0.1V \\ & 0 \\ & 3 \times 10^{-5}V + 0.3i(t) - 1.5 \times 10^{-8}V^2 + 0.3745 \end{bmatrix} , \quad (2.13)$$

$$B = \begin{bmatrix} 0 & 0 \\ -9K & 0 \\ 0 & 0.3I \end{bmatrix} . \quad (2.14)$$

By equating tumor differential equations to zero as following

$$\begin{cases} \dot{V} = 0 \\ \dot{K} = 0 \\ \dot{I} = 0 \end{cases} , \quad (2.15)$$

one can obtain the system equilibrium points. In absence of therapy, the only real solution of the system (2.15) corresponds to $V_{eq} = 28000.4 \text{ mm}^3$, $K_{eq} = 29528.1 \text{ mm}^3$ and $I_{eq} = 0.013$. This point is an important mark in the dynamical system since it corresponds exactly to the tumor plateau previously analyzed.

To compare the behavior of the non-linear and the linearized systems, simulations were performed for both systems at the equilibrium point – Figure 2.5 – regarding three different input rates.

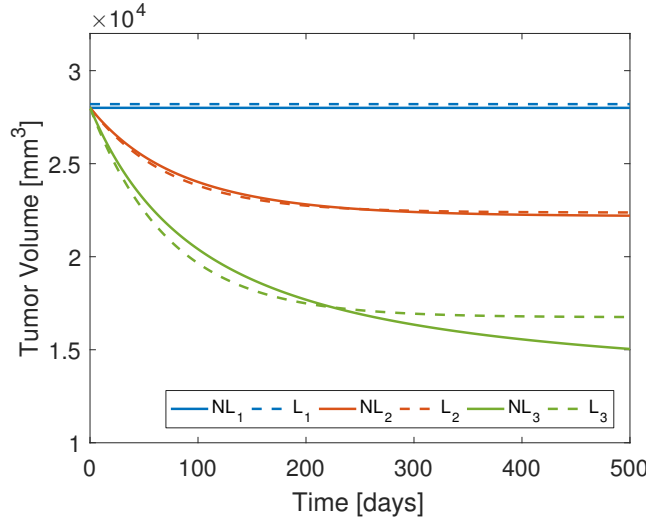


Figure 2.5: Behavior of the non-linear (NL) and linearized (L) systems for the equilibrium point. Test 1 is realized for $u = (0, 0)$, test 2 for $u = (0.1, 0.1)$ and test 3 for $u = (0.2, 0.2)$.

As expected, the non-linear and the linear curves are very similar for small variations, meaning for low input rates. For higher input rates, *e.g.* for the third test where $u = (0.2, 0.2)$, some small differences can be noticed. The similarity between both curves is important for the work that is going to be addressed in the next chapters, since the linearized tumor model is going to be used in the control framework.

In order to analyze the trajectories of the three state variables (V , K , I) of the non-linear tumor model – equations (2.7), (2.8), and (2.9) – the phase portrait of the tumor dynamical system was performed – Figure 2.6.

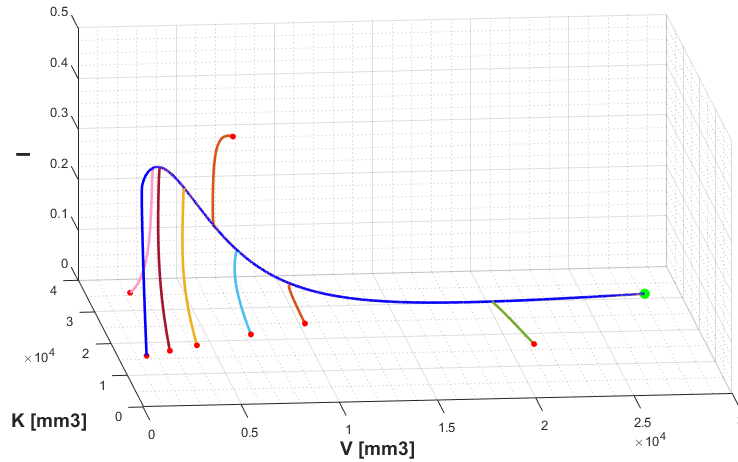


Figure 2.6: Phase portrait of tumor dynamical system.

Independently of the initial conditions, the system demonstrates a tendency towards a "common" trajectory leading the tumor to the plateau level – the equilibrium point in the absence of therapy – marked as green in Figure 2.6. In other words, in absence of therapy, there exists a predominant trajectory which is always going to be followed. Aside from that, once more, an initial immune reaction is obtained for small tumors resulting in an increase in the immunocompetent cells density and, con-

sequently, in a slower initial tumor growth. However, since IS cannot alone successfully fight cancer cells, as described before, IS population tends to disappear.

Considering the linearized system and evaluating the eigenvalues of matrix A , which have the same value as the system poles, the results obtained are

$$\begin{cases} \lambda_1 = -0.0136 \\ \lambda_2 = -8.2580 \\ \lambda_3 = -11.2975 \end{cases} . \quad (2.16)$$

Since all the eigenvalues are negative, the equilibrium point x_{eq} is a stable focus, that is, x_{eq} is an attractive equilibrium point. Furthermore, λ_2 and λ_3 are much larger than λ_1 , meaning that the system has a much faster response in the directions corresponding to eigenvectors V_2 and V_3 . This means that, independently of the tumor initial conditions, the system is aiming at a point in the line defined by the eigenvector V_1 . Figure 2.7 shows the direction of these vectors plotted in the equilibrium point.

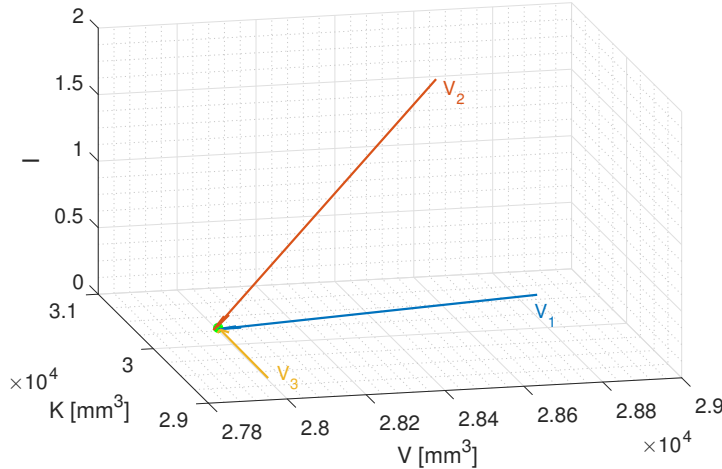


Figure 2.7: Eigenvectors of the linearized system plotted in x_{eq} .

3

Pharmacodynamical Model

Contents

3.1 Pharmacokinetics	20
3.2 Pharmacodynamics	22
3.3 Drug Resistance	23
3.4 Toxicity	25

In order to formulate a patient model, a pharmacodynamical model has to be taken into consideration. This model incorporates pharmacological systems and physiological processes that influence drug concentration time profile and its effect in the organism. In the following sections, the considered biological aspects – PK, PD, DR and toxicity – are described.

3.1 Pharmacokinetics

Pharmacokinetics (PK) is the one being responsible for determining the fate of substances administered to the organism and thus drug-concentration time profiles in the body. These profiles depend on a variety of factors related to the substance properties and the way the organism reacts to it, as well as with the drug administration method which is usually one of the following: Intravenous (IV), Constant Infusion Therapy (CIT) or Oral Administration (PO).

PK is divided into 4 processes: absorption, distribution, metabolism and excretion. The first phase is usually disregarded for IV and CIT. However, it is crucial when a PO therapy is applied because only part of drug concentration is going to the blood. During the second phase, the drug spreads all over the body, possibly reaching the target site. The last two phases are responsible for the elimination of the drugs either in the liver – metabolism – or through the kidneys – excretion.

In this section, the PK behavior is going to be explored for an IV therapy, since it is the administration mode approached in this work.

After IV bolus administration, a certain drug is immediately distributed to the blood stream and other highly perfused tissues. After this initial spread, drug concentration quickly decreases due to the distribution to the organs and tissues, as well as to the elimination from the organism. After reaching an equilibrium point, the fading rate decreases in a way that exactly corresponds to the rate of elimination, which is slower than the initial one.

This process can be incorporated in a compartmental model, which quantitatively describes the pharmacokinetic behavior of a drug in the organism [87]. The entire body is subdivided in one or more interconnected compartments, each one having its own volume of distribution and clearance rates. Considering it as a two-compartment model – Figure 3.1 – the main compartment represents the blood and the heavily vascular organs supplied, while the peripheral compartment the rest of the body. Besides that, drug administration and elimination are considered to occur in the central compartment, since drug is introduced to the organism intravenously and its elimination takes place in two of the most "vascularized" organs.

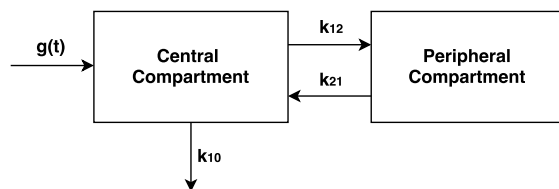


Figure 3.1: Two-compartment PK model.

Since all the transfer processes are of first-order, drug quantity in the central (C_p) and in the

peripheral compartment (P) can be represented by the differential equations

$$\dot{C}_p = g + k_{21}P - k_{12}C_p - k_{10}C_p , \quad (3.1)$$

$$\dot{P} = k_{12}C_p - k_{21}P , \quad (3.2)$$

since drug in any compartment is given by the sum of drug transferred into it minus the sum of drug transferred out of the compartment. The transfer rates between both compartments and the elimination rate are represented by variables k_{12} , k_{21} , and k_{10} , respectively, and drug administration rate by g .

Integrating equation (3.1) and dividing by the compartment volume results in the profile of the central compartment drug concentration C_p [$mg/kg/ml$] given by

$$C_p = \frac{D(\alpha - k_{21})}{V_c(\alpha - \beta)} e^{-\alpha t} + \frac{D(k_{21} - \beta)}{V_c(\alpha - \beta)} e^{-\beta t} , \quad (3.3)$$

where D is the dose given to the patient in mg/kg . The constants α and β are the hybrid rates of distribution and elimination processes, respectively, and are given by

$$\alpha = \frac{1}{2} \left[(k_{12} + k_{21} + k_{10}) + \sqrt{(k_{12} + k_{21} + k_{10})^2 - 4k_{21}k_{10}} \right] , \quad (3.4)$$

$$\beta = \frac{1}{2} \left[(k_{12} + k_{21} + k_{10}) - \sqrt{(k_{12} + k_{21} + k_{10})^2 - 4k_{21}k_{10}} \right] . \quad (3.5)$$

For bevacizumab, the PK parameters estimated in [88] were used, and for atezolizumab, the two compartment model values were calculated from the experimental parameters presented in [89, 90]. In Table 3.1 these constants are summarized.

Table 3.1: Pharmacokinetics parameters for bevacizumab and atezolizumab.

Parameter	Bevacizumab	Atezolizumab	Units
k_{12}	0.223	0.3	day^{-1}
k_{21}	0.215	0.2455	day^{-1}
k_{10}	0.0779	0.0643	day^{-1}
V_c	2660	3110	ml

It is worth noticing that from equation (3.3) results a drug concentration in $mg/kg/ml$. However, drug doses are usually described in mg/kg . Therefore, in order to make a more straightforward analysis and to render an explicit comparison between tumor growth and PK models possible, the output of C_p is multiplied by the volume V_c , being C_p given also in $[mg/kg]$.

Some simulations were performed with the aim of perceiving the drug profile in the plasma after a combined bolus of bevacizumab and atezolizumab – Figure 3.2. As expected, two different phases of decay can be visualized in Figure 3.2(b): the first one corresponds to the distribution of drug in the body whilst the second one to the elimination at a constant rate. The differences between both drugs are not relevant, being the elimination rate the most notable distinction.

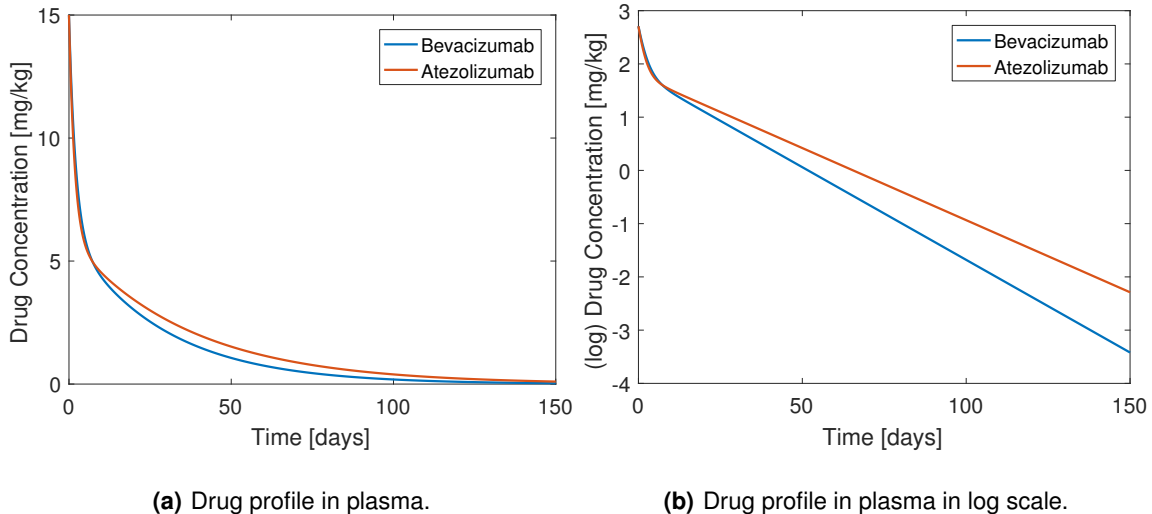


Figure 3.2: Drug concentration in the main compartment for a combined bolus of $15 \text{ mg}/\text{kg}$ of bevacizumab and $15 \text{ mg}/\text{kg}$ of atezolizumab, using equation (3.3).

3.2 Pharmacodynamics

Pharmacodynamics (PD) allows the description of the relationship between drug effect u and drug concentration C_p , which contributes to the understanding of a drug response and its effectiveness. It is worth to note that in this section the drug effect is described as u , representing then $g(t)$ and $i(t)$.

PD has been widely represented by the Hill Equation [41], a four parameter equation of a nonlinear relationship between concentration and drug effect, given by

$$u = u_{max} \frac{C_p^\alpha}{C_{50}^\alpha + C_p^\alpha}, \quad (3.6)$$

where u_{max} is the maximum effect, typically unitary, C_{50} is the drug concentration for which 50 % of maximum effect is obtained, and α is the Hill coefficient determining the steepness of the resulting sigmoid. The behavior of the drug effect curve depends on the current drug concentration, the size of the administration period intervals and some drug parameters, mainly its half-life and C_{50} . The C_{50} parameter for bevacizumab and atezolizumab was calculated from the values in [91, 92] using their respective molecular weight – Table 3.2. For simplicity, the constant α was considered unitary.

Table 3.2: Pharmacodynamics parameters for bevacizumab and atezolizumab.

Parameter	Bevacizumab	Atezolizumab	Units
MW	149168.82	144612.59	g/mol
C_{50}	72	40	pM
C_{50}	0.1074	0.0578	$\mu\text{g}/\text{mL}$
C_{50}	11.4274	7.1903	mg/kg
α	1	1	–

A typical behavior of the effect curve u is shown in Figure 3.3. It is observable that, as the drug concentration increases, it eventually reaches a maximum value, the effect saturation. The concentration needed to achieve the same effect for both drugs is higher for bevacizumab.

The inverse of the PD model is also an important point to emphasize, since given an effect it is possible to directly calculate the required concentration. For $\alpha = 1$, it is given by

$$C_p = C_{50} \frac{u}{u_{max} - u}. \quad (3.7)$$

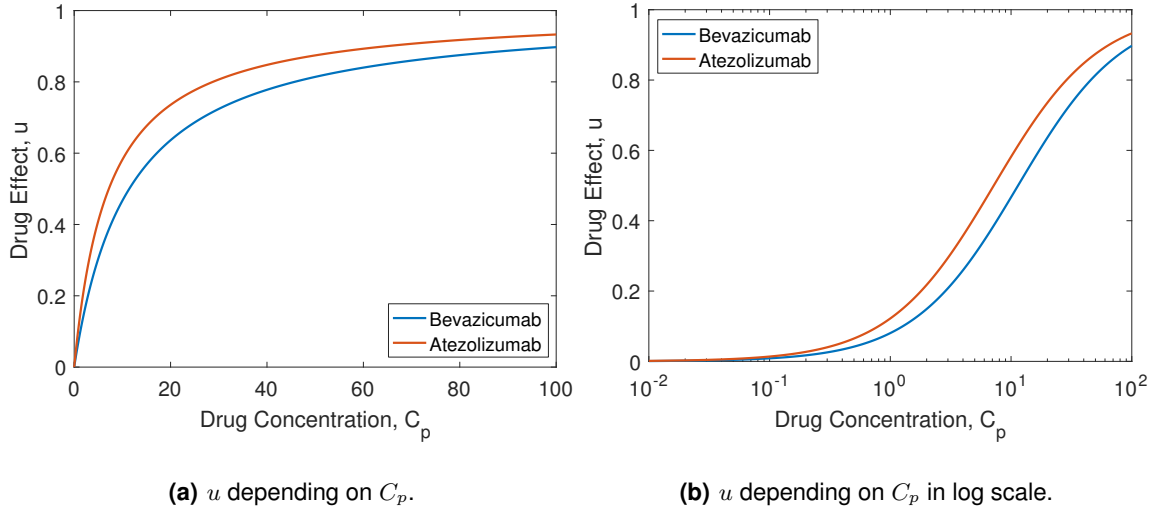


Figure 3.3: Drug effect depending on drug concentration, according to (3.6).

3.3 Drug Resistance

The development of new promising drugs is transforming the treatment of advanced cancers. However, in addition to therapy design, it is necessary to assure that the correct level of drug concentration is presented in the target, taking in consideration the way the organism reacts to drugs, particularly how tumor cells resist to it. Resistance to therapy results from host factors, such as poor absorption or rapid metabolism, or epigenetic alterations in the cancer cells [93].

The target cells of anti-angiogenesis is a differentiating point: since it deals with normal cells, drug resistance is not a key factor for therapy failure because tumor cell sensitivities are not being exploited and cells do not have additional adaptation abilities. However, some mechanisms of resistance to antiangiogenic drugs have been found recently, such as the amplification of pro-angiogenic genes, escape via different modes of vascularization, secretion of multiple pro-angiogenic factors and recruitment of pro-angiogenic BMDCs [94].

The likelihood of positive response to cancer immunotherapy differs across tumor types, indicating that intrinsic and acquired resistance are a key factors for treatment responsiveness [95].

For these reasons, a model for drug resistance was considered for both drugs, taking advantage of the capacity of malignant cells to proliferate into more resistant cells when low drug concentration is present in the plasma, since the weak cells are killed and the strong ones are going to reproduce. This means that when C_p is smaller than a threshold, drug resistance is acquired and a larger dose to achieve the same effect is necessary. Acquired resistance can be incorporated in the model by increasing the C_{50} parameter from PD [96], since it will directly decrease the drug effect.

The drug resistance model can be defined as

$$C_{50}(t) = f(t)C_{50}^{base}, \quad (3.8)$$

where C_{50}^{base} is the previously defined initial value and $f(t)$, which is a function that increases C_{50} if the drug concentration C_p is below the threshold L_r , is given by

$$f(t) = 1 + K_r \int_0^t \max[0, L_r - C_p(\tau)] d\tau. \quad (3.9)$$

The parameter K_r is a positive constant that measures the capacity of the malignant cells to develop resistance against a certain drug.

Figure 3.4 exemplifies the period in which resistance is developed.

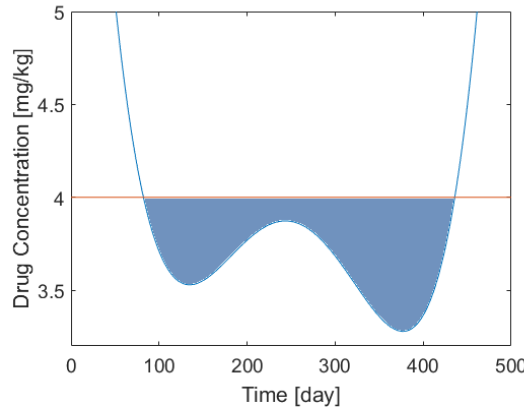


Figure 3.4: Period of time (blue area) in which resistance is developed. Concentration threshold level with value $L_r = 4 \text{ mg/kg}$.

The effect in parameter C_{50} induced by drug resistance is illustrated in Figure 3.5 for a double bolus therapy of bevacizumab.

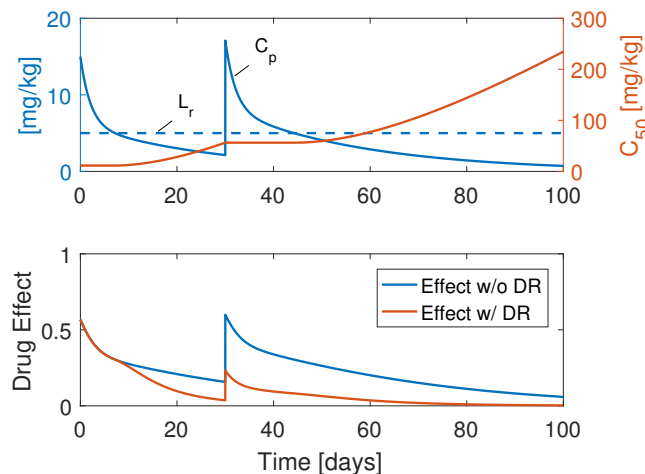


Figure 3.5: Variation of C_{50} due to acquired resistance and respective therapy effect with and without considering DR. $L_r = 5 \text{ mg/kg}$, $K_r = 0.1 \text{ mg/kg}$, $C_{50base} = 11.4274 \text{ mg/kg}$.

C_{50} is always constant except from the periods when concentration C_p is below the threshold L_r . The increase in C_{50} is proportional to the area given by the difference between L_r and C_p curves,

when C_p is smaller than the threshold. This increase affects therapy effect, since tumor cells become more resistant. This cells resistance can be seen in the second plot where the drug effect curve is illustrated with and without considering Drug Resistance (DR). The difference between both curves is accentuated, especially after given the second bolus.

3.4 Toxicity

A treatment where a large drug dosage is applied to the patient can be very effective. However, its side effects due to the quantity of drug administrated can lead the patient to death. Toxicity is thus a degree to which a drug can damage an organism.

One of the main advantages of antiangiogenic treatments is the low level of toxicity imposed to the patient organism. However, recently some additional side effects have been detected especially concerning the cardiovascular system [97]: hypertension, left ventricular systolic dysfunction and, in extreme cases, thromboembolic problems. In immunotherapy, several complications can also arise such as anorexia, thrombocytopenia, anemia and coagulopathy [98].

Clinical toxicity levels cannot be explicitly measured and there are no mathematical models for their evaluation. However, following the Common Terminology Criteria for Adverse Events (CTCAE) [99], toxicity in clinical trials can be graded as mild (grade 1), moderate (grade 2), severe (grade 3), life-threatening (grade 4) or death (grade 5).

By evaluating the concentration of drug induced in the body during therapy, toxicity levels T_g for anti-angiogenesis and T_i for immunotherapy, can be estimated by using a function yielding a certain small value until a certain amount of concentration is achieved. After this threshold, the function grows exponentially [96]. The toxicity curves considered in this work are illustrated in Figure 3.6.

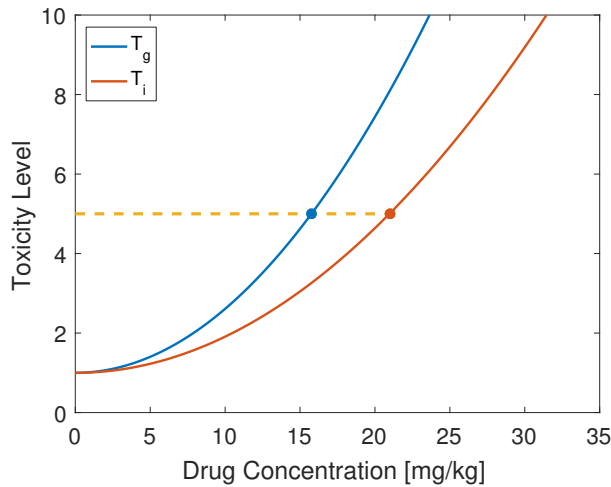


Figure 3.6: Toxicity levels for bevacizumab, T_g , and atezolizumab, T_i . The blue and red marks are representing the drug concentration for which toxicity level is maximum (grade 5).

These curves were selected so that the grade 5 of toxicity was reached when the drug concentration in the organism was over 5 % above the maximum dose allowed. These doses are 15 and 20 mg/kg , respectively, for bevacizumab [100] and atezolizumab [101].

Denoting T_x as the total toxicity in the organism, it can be measured by averaging between T_g and T_i , that is, by considering

$$T_x = \frac{T_g + T_i}{2}. \quad (3.10)$$

4

Patient Model

Contents

4.1 Summary of Patient Model	28
4.2 Patient Model Simulations	28

4.1 Summary of Patient Model

By joining the tumor growth model analyzed in Chapter 2 and the pharmacodynamical model composed by the systems described in Chapter 3 – Pharmacokinetics (PK), Pharmacodynamics (PD), Drug Resistance (DR) and toxicity – a final model for the patient can be formulated.

In Figure 4.1, a summary of the patient model is described. In each block the equation or system of equations representing each topic is also identified.

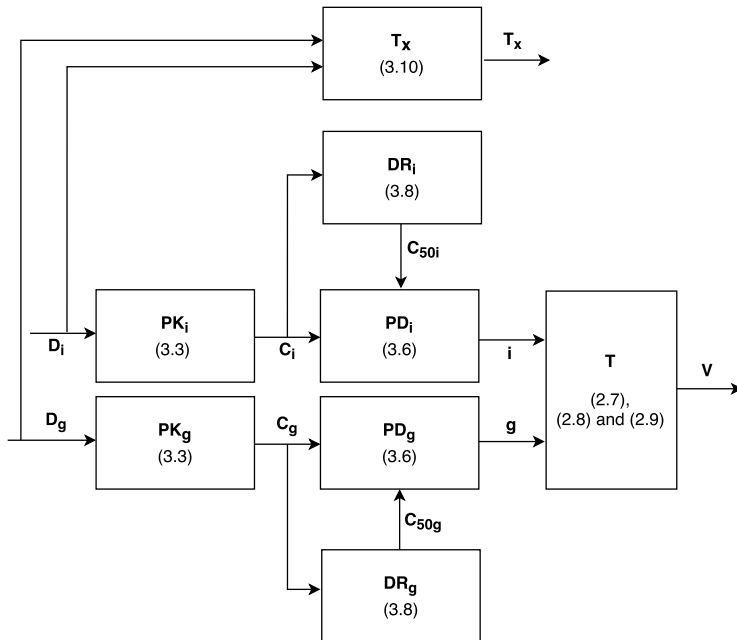


Figure 4.1: Summary of patient model.

It is noticeable that toxicity does not have direct influence on any of the other models, since it does not influence the drug effect, being only an organism response to therapy. However, those are toxicity levels that constitute an important measurement that is going to be used later in Chapter 5 during the treatment planning optimization.

4.2 Patient Model Simulations

In order to understand the behavior of the patient model, simulations were performed for several scenarios.

4.2.1 Intravenous (IV) Bolus Therapy

For a bolus therapy of $D_g = 15 \text{ mg/kg}$ of bevacizumab and $D_i = 20 \text{ mg/kg}$ of atezolizumab with a periodicity of 21 days, drug sensibilities of $\eta = 9 \text{ kg/mg/day}$ and $\kappa = 0.3 \text{ kg/mg}$, drug resistance thresholds $L_r = L_{rIT} = 6 \text{ mg/kg}$, $K_r = 0.1$, $K_{rIT} = 0.3$ and $V_0 = 5000 \text{ mm}^3$, $K_0 = 6000 \text{ mm}^3$, and $I_0 = 0.1$, the results in Figures 4.2 and 4.3 were obtained.

Figure 4.2 shows the effect of drug resistance in the model, particularly during the first interval between bolus (day 0 to 21). In this interval there is a fast growth of C_{50} since drugs concentration is

lower than the threshold L_r during some days. This fact impacts the drug effect, since the first bolus is the strongest and the following ones have about half the effect.

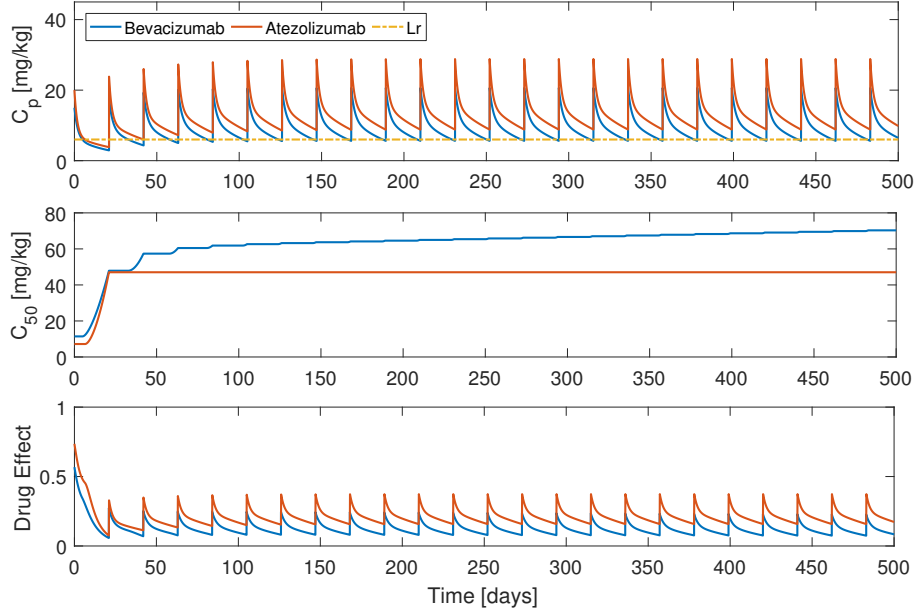


Figure 4.2: Drug concentrations, resistance and effect of the patient model for the following therapy: $D_g = 15 \text{ mg/kg}$, $D_i = 20 \text{ mg/kg}$, $d = 21 \text{ days}$, $\eta = 9 \text{ kg/mg/day}$, $\kappa = 0.3 \text{ kg/mg}$, $L_r = L_{rIT} = 6 \text{ mg/kg}$, $K_r = 0.1$, $K_{rIT} = 0.3$, $V_0 = 5000 \text{ mm}^3$, $K_0 = 6000 \text{ mm}^3$ and $I_0 = 0.1$.

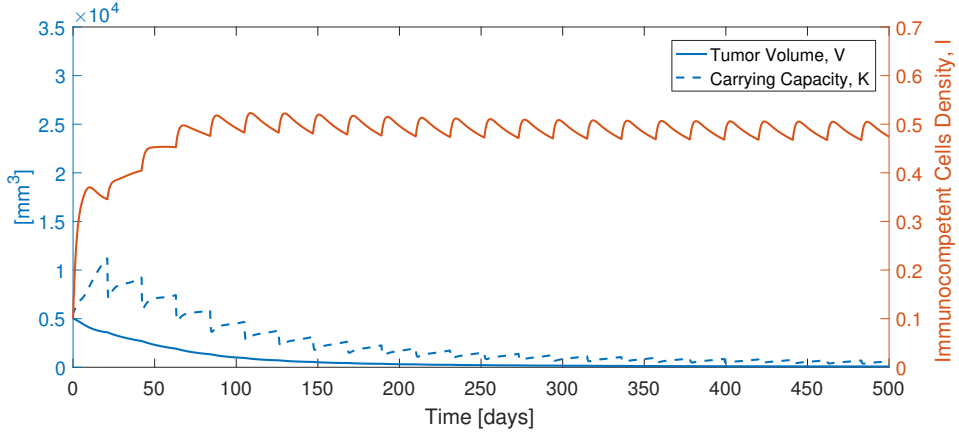


Figure 4.3: Tumor response of the patient model for the following therapy: $D_g = 15 \text{ mg/kg}$, $D_i = 20 \text{ mg/kg}$, $d = 21 \text{ days}$, $\eta = 9 \text{ kg/mg/day}$, $\kappa = 0.3 \text{ kg/mg}$ and $L_r = L_{rIT} = 6 \text{ mg/kg}$, $K_r = 0.1$, $K_{rIT} = 0.3$, $V_0 = 5000 \text{ mm}^3$, $K_0 = 6000 \text{ mm}^3$ and $I_0 = 0.1$.

It is estimated that the tumor is almost eradicated using this therapy, since the tumor volume tends slowly to zero – Figure 4.3. Having strong dosages applied since the beginning, this therapy takes advantage of the initial growth of the immunocompetent cells density – as illustrated in Figure 2.2(b) – to stimulate the action of the immune system against the tumor while preventing tumor to grow by inhibiting angiogenesis.

4.2.2 Effect of Dose

In the same conditions of the previous simulation, the patient model was tested for the four following therapies: only bevacizumab (15 mg/kg), only atezolizumab (20 mg/kg) and 7.5 and 10 mg/kg of bevacizumab combined with 12.5 and 15 mg/kg of atezolizumab, respectively.

The results obtained for the first two therapies are illustrated in Figures 4.4 and 4.5. Concentration, drug resistance and drug effect profiles are not shown since they have the same behavior as in the previous simulations.

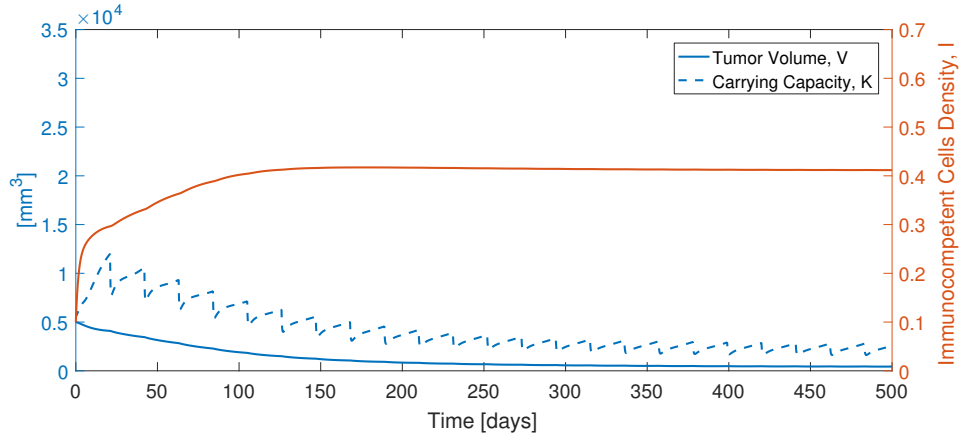


Figure 4.4: Tumor response of the patient model for the following therapy: $D_g = 15 \text{ mg/kg}$, $D_i = 0 \text{ mg/kg}$, $d = 21 \text{ days}$, $\eta = 9 \text{ kg/mg/day}$, $\kappa = 0.3 \text{ kg/mg}$ and $L_r = L_{rIT} = 6 \text{ mg/kg}$, $K_r = 0.1$, $K_{rIT} = 0.3$, $V_0 = 5000 \text{ mm}^3$, $K_0 = 6000 \text{ mm}^3$ and $I_0 = 0.1$.

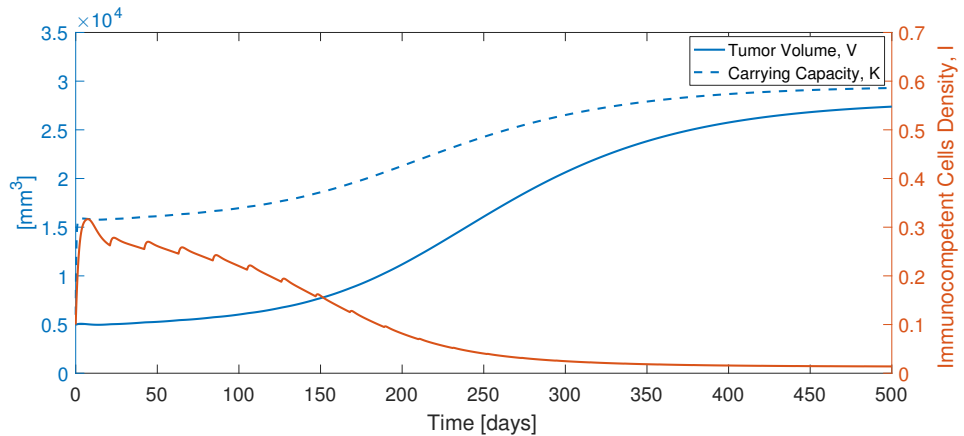


Figure 4.5: Tumor response of the patient model for the following therapy: $D_g = 0 \text{ mg/kg}$, $D_i = 20 \text{ mg/kg}$, $d = 21 \text{ days}$, $\eta = 9 \text{ kg/mg/day}$, $\kappa = 0.3 \text{ kg/mg}$ and $L_r = L_{rIT} = 6 \text{ mg/kg}$, $K_r = 0.1$, $K_{rIT} = 0.3$, $V_0 = 5000 \text{ mm}^3$, $K_0 = 6000 \text{ mm}^3$ and $I_0 = 0.1$.

It is possible to conclude that anti-angiogenesis has a bigger impact on the tumor than immunotherapy, since the immune boost cannot prevent tumor growth alone. However, the combined therapy is still a better approach than only anti-angiogenesis since eradication is faster despite the larger drug concentration in the body. This observation can be made if a comparison between Figures 4.3 and 4.4 is performed.

For the other two therapies the results shown in Figures 4.6, 4.7, 4.8 and 4.9 were obtained.

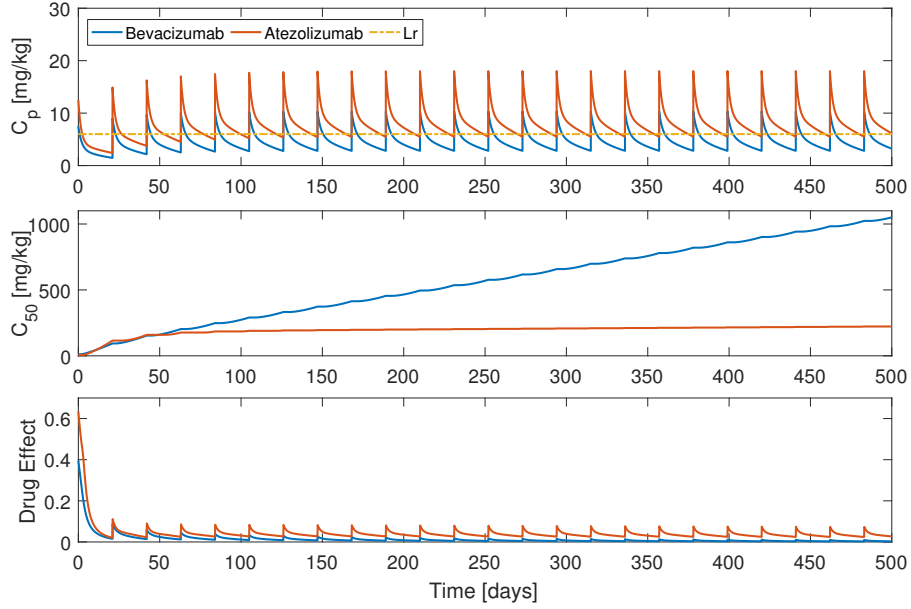


Figure 4.6: Drug concentrations and drug effect of the patient model for the following therapy: $D_g = 7.5 \text{ mg/kg}$, $D_i = 12.5 \text{ mg/kg}$, $d = 21 \text{ days}$, $\eta = 9 \text{ kg/mg/day}$, $\kappa = 0.3 \text{ kg/mg}$, $L_r = L_{rIT} = 6 \text{ mg/kg}$, $K_r = 0.1$, $K_{rIT} = 0.3$, $V_0 = 5000 \text{ mm}^3$, $K_0 = 6000 \text{ mm}^3$ and $I_0 = 0.1$.

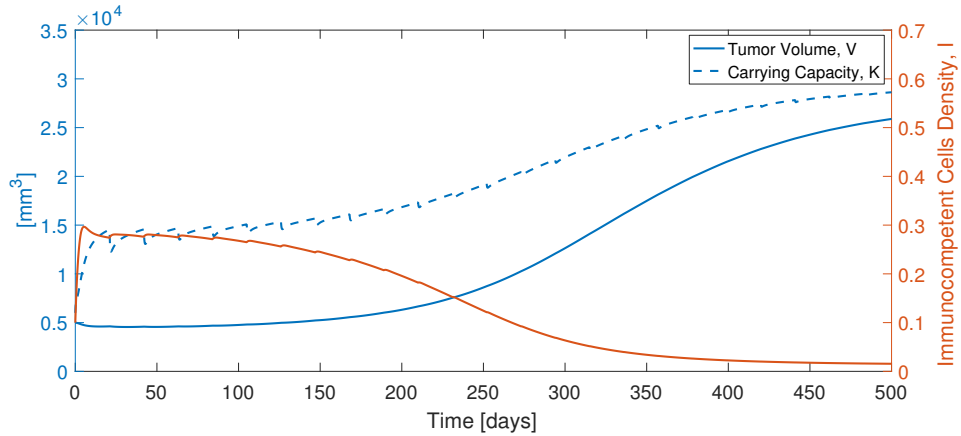


Figure 4.7: Tumor response of the patient model for the following therapy: $D_g = 7.5 \text{ mg/kg}$, $D_i = 12.5 \text{ mg/kg}$, $d = 21 \text{ days}$, $\eta = 9 \text{ kg/mg/day}$, $\kappa = 0.3 \text{ kg/mg}$ and $L_r = L_{rIT} = 6 \text{ mg/kg}$, $K_r = 0.1$, $K_{rIT} = 0.3$, $V_0 = 5000 \text{ mm}^3$, $K_0 = 6000 \text{ mm}^3$ and $I_0 = 0.1$.

A possible minimum dosage for therapy effectiveness can be predicted, since the results for the combined therapies are disparate. For the first combined therapy – $(D_g, D_i) = (7.5, 12.5) \text{ mg/kg}$ – dosages were smaller, so the effect was also expected to be lower. However, the average drug concentration, especially for bevacizumab, was inferior to the threshold L_r which had a big impact on effect of this therapy, which tends to zero as time goes by. For the second therapy – $(D_g, D_i) = (10, 15) \text{ mg/kg}$ – the effect was slightly higher and sufficient to shrink the tumor, however, with a slower decrease than in simulation of Figure 4.3.

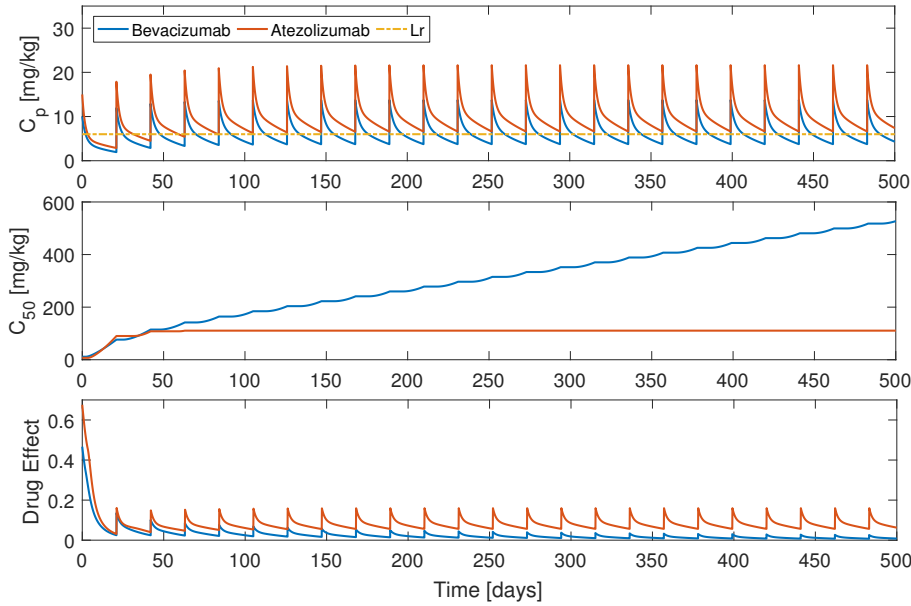


Figure 4.8: Drug concentrations and drug effect of the patient model for the following therapy: $D_g = 10 \text{ mg/kg}$, $D_i = 15 \text{ mg/kg}$, $d = 21 \text{ days}$, $\eta = 9 \text{ kg/mg/day}$, $\kappa = 0.3 \text{ kg/mg}$, $L_r = L_{rIT} = 6 \text{ mg/kg}$, $K_r = 0.1$, $K_{rIT} = 0.3$, $V_0 = 5000 \text{ mm}^3$, $K_0 = 6000 \text{ mm}^3$ and $I_0 = 0.1$.

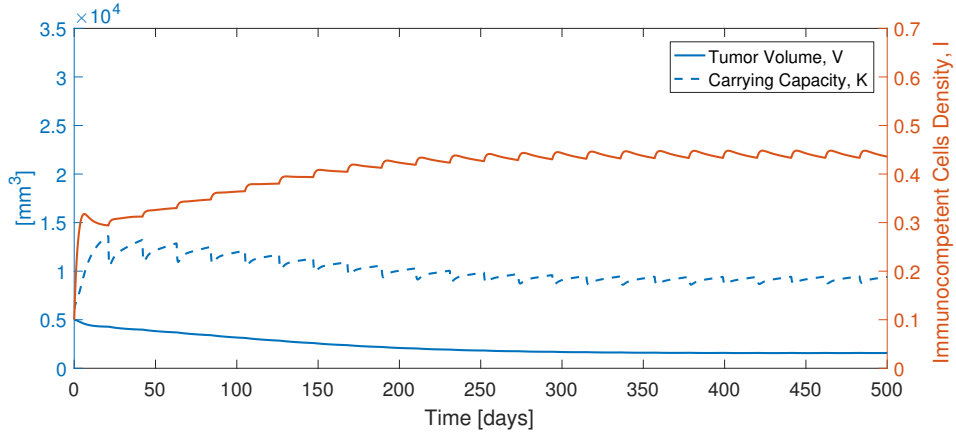


Figure 4.9: Tumor response of the patient model for the following therapy: $D_g = 10 \text{ mg/kg}$, $D_i = 15 \text{ mg/kg}$, $d = 21 \text{ days}$, $\eta = 9 \text{ kg/mg/day}$, $\kappa = 0.3 \text{ kg/mg}$ and $L_r = L_{rIT} = 6 \text{ mg/kg}$, $V_0 = 5000 \text{ mm}^3$, $K_0 = 6000 \text{ mm}^3$ and $I_0 = 0.1$.

4.2.3 Effect of Drug Sensitivities η and κ

In order to analyze the effect of the parameters η and κ , simulations for different combinations of sensitivities values were performed, for a therapy of 10 mg/kg of bevacizumab and 15 mg/kg of atezolizumab, remaining the values of the other parameters as before. It worth noticing that η and κ can have values between $[1.35; 11.25]$ and $[0.1; 0.5]$, respectively. Tumor response is illustrated in Figure 4.10 for distinct values of η and κ .

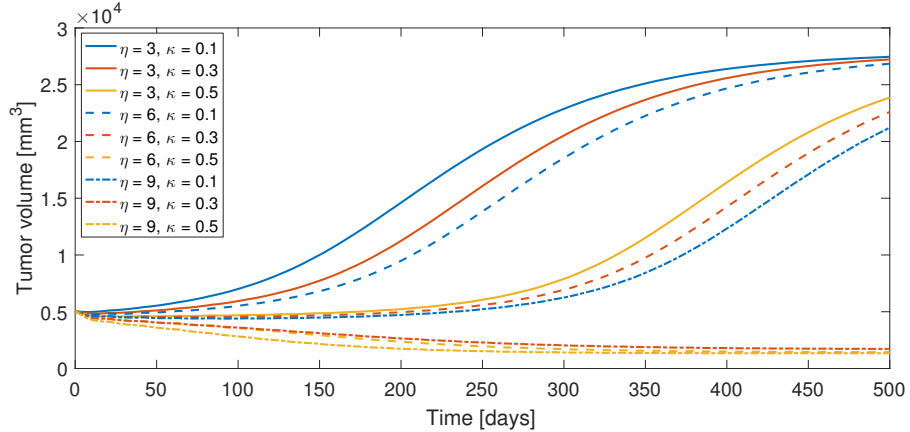


Figure 4.10: Tumor response of the patient model for different values of η and κ and for the following therapy: $D_g = 10 \text{ mg/kg}$, $D_i = 15 \text{ mg/kg}$, $d_g = d_i = 21 \text{ days}$, $L_r = L_{rIT} = 6 \text{ mg/kg}$, $K_r = 0.1$, $K_{rIT} = 0.3$, $V_0 = 5000 \text{ mm}^3$, $K_0 = 6000 \text{ mm}^3$ and $I_0 = 0.1$.

The results show the influence of both sensibilities η and κ in therapy. For low values of η , the tumor cannot be eradicated, independently of the value of κ , which only changes the tumor volume growth rate steepness. However, for example in the case of $\eta = 6$, tumor volume grows or decreases depending on the value of κ . For $\eta = 9$, tumor always shrinks, except for the minimum value of the immunotherapy sensitivity, *i.e.* $\kappa = 0.1$.

In conclusion, both parameters have impact on therapy effects, however, η renders a greater importance on the patient model since for low values of this parameter tumor volume never decreases. On the other hand, for high values of η , tumor eradication occur depending on κ values.

4.2.4 Effect of Periodicities d_g and d_i

Simulations were performed - Figure 4.11 - in order to test the influence of periodicity on patient model's results, that is, the way the interval between IV bolus, d_g for bevacizumab and d_i for atezolizumab, affects the tumor's response.

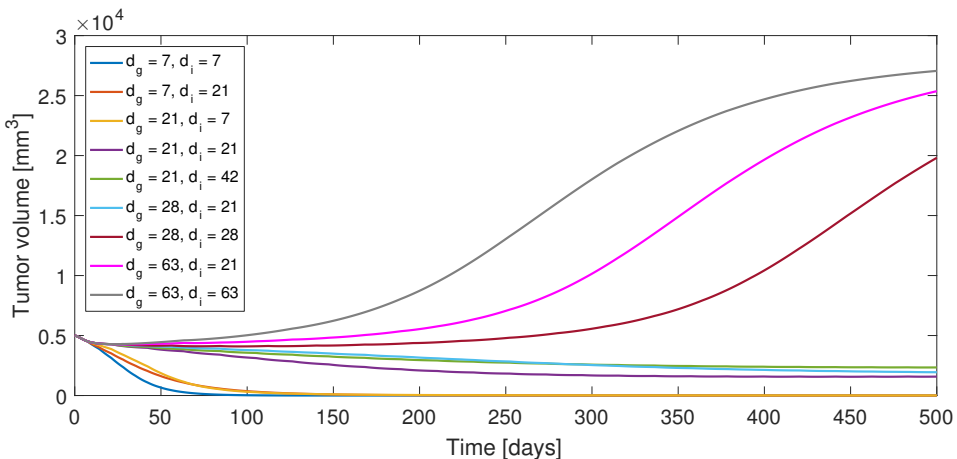


Figure 4.11: Tumor response of the patient model for different values of d_g and d_i and for the following therapy: $D_g = 10 \text{ mg/kg}$, $D_i = 15 \text{ mg/kg}$, $d_g = d_i = 21 \text{ days}$, $\eta = 9 \text{ kg/mg/day}$, $\kappa = 0.3 \text{ kg/mg}$, $L_r = L_{rIT} = 6 \text{ mg/kg}$, $K_r = 0.1$, $K_{rIT} = 0.3$, $V_0 = 5000 \text{ mm}^3$, $K_0 = 6000 \text{ mm}^3$ and $I_0 = 0.1$.

As expected, periodicity has an important influence on tumor's response. For this therapy, using small values of d_g can eradicate the tumor, or prevent its growth. However, when higher values are given to this parameter, therapy is not effective. On the other hand, the influence of d_i relates to the value of d_g , since for small intervals of administration of atezolizumab, the therapy effect depends on bevacizumab periodicity. For example, in the four cases where $d_i = 21 \text{ days}$, there is only an observed tumor's reduction for cases where d_g is less than or equal to 28 days .

Although the most effective therapy requires small periodicities, toxicity also has to be taken into consideration, since average drug concentration in blood is higher.

In conclusion, once more, anti-angiogenesis verifies a greater impact on therapy compared with immunotherapy. However, immunotherapy influences the way the tumor reacts to the therapy.

4.2.5 Effect of Therapy Duration T

In order to test the dependency of therapy effectiveness on its duration, several tests were performed – Figure 4.12.

For therapies starting at time $t = 0$, tumor growth can be stagnated and its final volume depends on the total duration of therapy since, for higher durations, tumor volume at time $t = 500$ has a smaller value. However, the difference between final tumor volume for therapies with durations $[0, 500]$ and $[0, 100]$ is only 1.28 cm^3 , which is not significant for a difference of 400 days on therapy duration. Therefore, if the therapy's goal is to stagnate the tumor growth while keeping a minimum toxicity level, therapy duration should have the smallest possible value.

For therapies which do not start on the initial time $t = 0$, that is, when the tumor is detected, tumor volume cannot be controlled regardless of the effect of therapy on slowing down its growth.

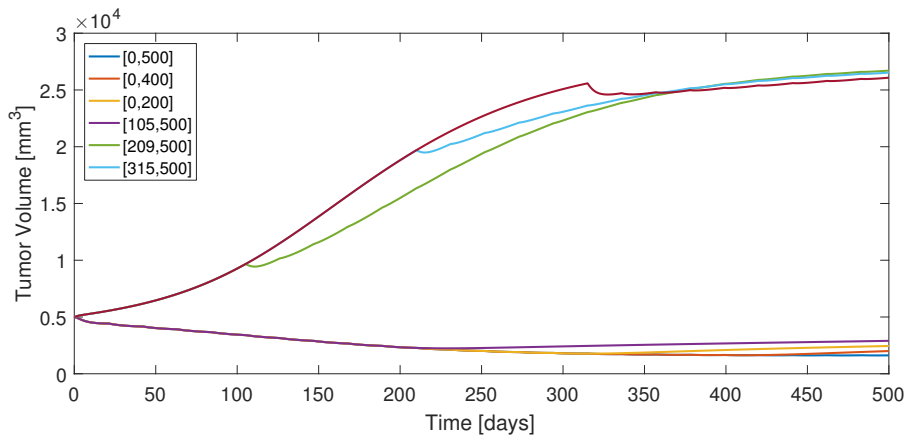


Figure 4.12: Tumor response of the patient model for different values of therapy duration T and for the following therapy: $D_g = 10 \text{ mg/kg}$, $D_i = 15 \text{ mg/kg}$, $d_g = d_i = 21 \text{ days}$, $\eta = 9 \text{ kg/mg/day}$, $\kappa = 0.3 \text{ kg/mg}$, $L_r = L_{rIT} = 6 \text{ mg/kg}$, $K_r = 0.1$, $K_{rIT} = 0.3$, $V_0 = 5000 \text{ mm}^3$, $K_0 = 6000 \text{ mm}^3$ and $I_0 = 0.1$.

5

Controller Design for a Patient Model

Contents

5.1 Controller	36
5.2 Pharmacodynamical Simulation	39

Considering that the patient model is fully understood, that is, all his parameters are known and do not vary over time, a controller framework can be established. In this way, within an optimal control law, the tumor volume V can be led to follow a certain reference R by administrating a therapy with the least possible toxicity. Since there is no uncertainty in the model, a feedback controller with proportional gains and a modified structure for following the tracking error can be used, as it is illustrated in Figure 5.1.

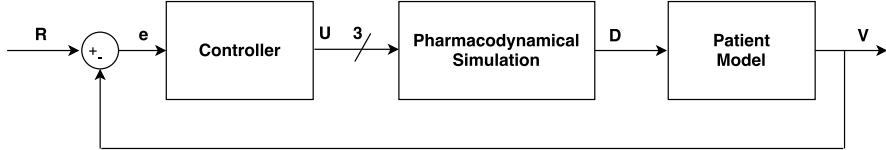


Figure 5.1: Controller architecture for a patient model.

The Patient Model block describes the characterized in the Section 4 with a linearized tumor growth model, for a patient with fully known characteristics.

The Controller block is responsible for producing three different optimal effects U_i with $i = 1, \dots, 3$ by analyzing the tracking error $e = R - V$. In this work, the Linear Quadratic Gaussian (LQG) design technique is used for designing a robust controller. This controller is based on a Linear Quadratic Regulator (LQR) with state variable feedback, being the state estimations provided by a Kalman Filter. This combined system of state feedback, contrary to an output feedback system, assures certain robustness properties, in terms of gain and phase margin, that are necessary for a proper system operation [102].

The Pharmacodynamical Simulation block is the one responsible for selecting, at each instant, the therapy with the lowest toxicity. Aside from this role, since in practice a drug effect cannot be directly induced in the patient, this block translates the effect U_i , given by the controller, in a drug dose D that is going to be administrated to the patient.

5.1 Controller

5.1.1 Controllability and Observability

For guaranteeing that the system is fully controllable, that is, to ensure that an external input can move, in a finite time interval, the internal state of the system from an initial to a final condition, the controllability matrix \mathcal{C} has to have rank equal to the dimension of the state vector x [103]. Since $\mathcal{C} = [B \ AB \ A^2B]$, a controllability matrix depending on the parameters of the tumor growth model can be derived, resulting in

$$\mathcal{C} = \begin{bmatrix} 0 & 0 & -V\eta\lambda & -IV\gamma\kappa \\ -K\eta & 0 & K\eta(\mu + \eta g(t) + V^{\frac{2}{3}}d) & 0 \\ 0 & I\kappa & 0 & I\kappa(\mu_I(-\beta V^2 + V) - \delta + i(t)\kappa) \\ & & -(V^2\eta\lambda^2)/K & IV^2\gamma^2\kappa \\ & & -K\eta(\mu + \eta g(t) + V^{\frac{2}{3}}d)^2 & 0 \\ & & 0 & I\kappa(\mu_I(-\beta V^2 + V) - \delta + i(t)\kappa)^2 \end{bmatrix}. \quad (5.1)$$

For the parameters values used in Section 4, matrix \mathcal{C} has rank 3. Therefore, it can be concluded that the system is controllable.

Since state direct measurements are not available, an observer has to be implemented. Thus, in order to certify that the system is fully observable, the observability matrix \mathcal{O} has to be computed. If the rank of the matrix \mathcal{O} is equal to the dimension of the state vector x [103], it is possible to say that the internal states can be inferred by analyzing the system input and output. Observability matrix is given by $\mathcal{O} = [C \; CA \; CA^2]^T$ and can also be specified in terms of tumor growth model parameters, being given by

$$\mathcal{O} = \begin{bmatrix} 1 & -\lambda - I\gamma - \lambda \log \frac{V}{K} & (\lambda + I\gamma + \lambda \log \frac{V}{K})^2 + \left(V\lambda \left(b - \frac{2Kd}{3V^{\frac{1}{3}}} \right) \right) / K + IV\gamma\lambda(2V\beta - 1) \\ 0 & V\frac{\lambda}{K} & -(V\lambda(\mu + \eta g(t) + V^{\frac{2}{3}}d)) / K - (V\lambda(\lambda + I\gamma + \lambda \log \frac{V}{K})) / K \\ 0 & -V\gamma & V\gamma(\lambda + I\gamma + \lambda \log \frac{V}{K}) - V\gamma(\mu_1(-\beta V^2 + V) - \delta + i(t)\kappa) \end{bmatrix}^T. \quad (5.2)$$

By using the same values as before, it can be noticed that the matrix \mathcal{O} has rank 3 and then that the system is also observable.

5.1.2 Controller Implementation

As mentioned before, the controller architecture is different from a typical feedback controller since the control action is not performed directly in the feedback loop. Instead, control action is executed depending on the process error. The controller used in the architecture presented is illustrated in Figure 5.2, where K_i with $i = 1, \dots, 3$ are constant vectors, whose product with the state estimation \hat{x} results in the design of three different therapies. These therapies are described in the effect vector $U = [U_1 \; U_2 \; U_3]$, where $U_i = [G_i \; I_i]^T$ with $i = 1, \dots, 3$, being G and I the desired effects of the anti-angiogenesis and the immunotherapy, respectively.

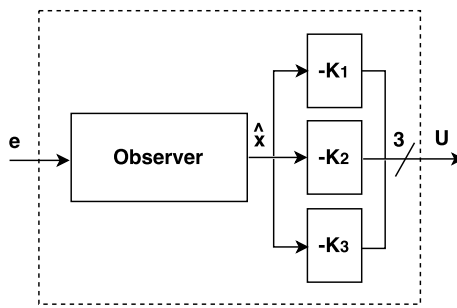


Figure 5.2: Controller scheme.

Considering the state space representation of the plant, *i.e.* of the linearized tumor growth model, the state space x can be represented by the system

$$\dot{x} = Ax + Bu, \quad (5.3)$$

$$y = Cx, \quad (5.4)$$

where, as previously denoted, $x = [V \; K \; I]^T$, $u = [g \; i]^T$ and the output y represents tumor volume. Since the state direct measurement is not available, the observer is responsible for calculating an estimation of x , named \hat{x} . The estimation \hat{x} can be obtained by including an additional term in the

equation (5.3). This term is proportional to the estimation error, and the multiplication by a matrix L ensures the asymptotic convergence of the state estimations to the real state [102]. The state estimation is thus obtained by

$$\dot{\hat{x}} = A\hat{x} + BU_T + L(y - C\hat{x}) , \quad (5.5)$$

$$\hat{y} = C\hat{x} , \quad (5.6)$$

where U_T is the least toxic therapy from the set of designed therapies U . Notice that, since u is not measurable, an approximation of it, U_T , is used for the state estimation.

In this work, the observer matrix L is calculated by using the Kalman estimator design for continuous-time systems. The Kalman filter assumes the inclusion of process noise w and measurement noise v , and, by optimizing a quadratic cost, computes the Kalman gain L with dimension $[3 \times 1]$. The covariance matrix of w , Q_o , and of v , R_o , can be defined and the values chosen were $Q_o = 1000I$, where I is the identity matrix, and $R_o = 0.1$.

The LQR controller consists of a state feedback control law whose gains are selected in order to minimize an infinite horizon quadratic cost J_i [102], given by

$$J_i = \int x^T Q x + U_i^T R_i U_i dt , \quad i = 1, \dots, 3 , \quad (5.7)$$

where $Q \succcurlyeq 0$ and $R_i \succ 0$ are matrices that can be tuned. Choosing a large value for Q means that the system is intended to stabilize with the least possible changes. On the other hand, decreasing R_i means increasing the power of the manipulated variable U_i , *i.e.* having a greater drug effect and an higher system bandwidth leading to a faster closed loop response.

The selected value for the matrix Q were $Q = C^T C$. The three different input signals U_i are performed by using different values for the matrix R_i . Since U_i has dimension $[2 \times 1]$, R_i can be chosen in order to balance the importance of anti-angiogenesis and immunotherapy in the treatment. The chosen matrices are

$$R_1 = \begin{bmatrix} 100 & 0 \\ 0 & 1000 \end{bmatrix} , R_2 = \begin{bmatrix} 100 & 0 \\ 0 & 100 \end{bmatrix} , R_3 = \begin{bmatrix} 1000 & 0 \\ 0 & 100 \end{bmatrix} .$$

Since $U_i = [G_i \ I_i]^T$, the effect of the immunotherapy in U_1 is smaller than in the same therapy in U_2 , whilst the effect of the anti-angiogenesis in U_3 is lower than in U_2 .

The input vector U_i is

$$U_i = -K_i \hat{x} , \quad i = 1, \dots, 3 , \quad (5.8)$$

where K_i is the feedback gain with dimension $[2 \times 3]$, computed by

$$K_i = (B^T S_i B + R_i)^{-1} B^T S_i A , \quad i = 1, \dots, 3 . \quad (5.9)$$

The matrix S_i in equation (5.9) is the only definite solution of the Riccati equation

$$A^T S_i A - A^T S_i B (B^T S_i B + R_i)^{-1} B^T S_i A + Q = 0 , \quad i = 1, \dots, 3 . \quad (5.10)$$

Since the controller has a non-null reference, changes in equations (5.5) and (5.6) have to be established for including additional terms that lead the system to follow the set point at each time

instant [104], resulting in the following equations

$$\dot{\hat{x}} = A\hat{x} + BU_i + L(y - C\hat{x}) + MR , \quad (5.11)$$

$$\hat{y} = C\hat{x} + NR , \quad (5.12)$$

where R is the reference and M and N are, respectively, a $[3 \times 1]$ vector and a scalar, that can be adjusted.

In order to use the tracking error e in the controller these tuning parameters were selected as $N = 0$ and $M = -L$, being the system controller defined by the following set of equations

$$\dot{\hat{x}} = (A - BK_i - LC)\hat{x} - Le , \quad (5.13)$$

$$\hat{y} = C\hat{x} , \quad (5.14)$$

$$U_i = -K_i\hat{x} . \quad (5.15)$$

In the following section, the process of selecting the least toxic treatment U_T , from the range of therapies U , is explained.

5.2 Pharmacodynamical Simulation

As mentioned before, the Pharmacodynamical Simulation block has two main roles: choosing the least toxic therapy and transforming a drug effect into a drug dose.

To accomplish this roles, the Pharmacodynamical Simulation block has to simulate pharmacodynamical processes of the patient before making any decision. Thus, one can consider this block as a software that aims to approximate patient behavior, being possible to have some discrepancy with reality. That is, the parameters of the DR and the PD belonging to this block, θ_{PS} , can differ from the ones in the Patient Model θ_{PM} . In this chapter, there is no discrepancy since the patient model is fully known. However, in Section 9 this topic is going to be approached with different values of uncertainty, that is described by the parameter $\Delta\theta_{PS}$ (in percentage).

The composition of the Pharmacodynamical Simulation and also its interconnection with the Patient Model are illustrated in Figure 5.3. It must be noticed, however, that only for illustrative purpose, the structure of the Patient Model is presented in a simplified form.

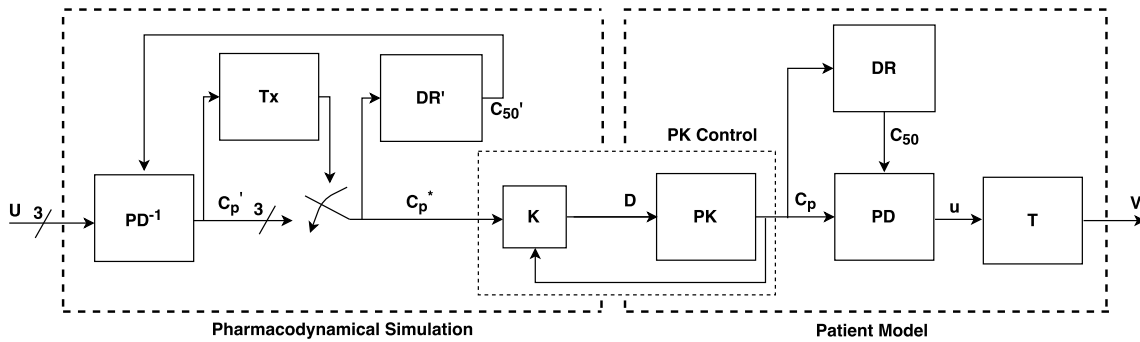


Figure 5.3: Composition of the Pharmacodynamical Simulation and Patient Model blocks.

It is of crucial importance to make a balance between the toxicity and the effectiveness of a therapy, since large drug concentrations can bring about a high damage. That is why the first role of the Pharmacodynamical Simulation block is exactly to choose, from the set of therapies U designed by the controller, the one that has the least impact on the patient, U_T . This process is executed by firstly transforming the effect vector U into a concentration vector C'_p , through the inverse of the PD, denoted PD^{-1} , described by equation (3.7). The parameter C_{50} necessary for this transformation is calculated through an approximation of the DR model, named DR' . In this case, both models have no difference due to the lack of deviation in its parameters.

After the concentration calculation, it is possible to measure the toxicity levels, as described in Section 3.4. Therefore, the least toxic drug concentration is the one chosen to be administered to the patient. This process of measurement and minimization of toxicity is performed by a block named Tx .

In practice, it is desired that the concentration C_p of the Patient Model follows the reference C_p^* , selected by the Pharmacodynamical Simulation block, since it is the least toxic drug concentration designed by the controller. This is achieved by the *PK Control* block that controls the PK model by using a linear feedback project. However, since PK information cannot be directly accessed and C_p tends to be equal or almost the same as C_p^* , one can assume *PK Control* as a unitary gain. In this way, the Pharmacodynamical Simulation and the Patient Model blocks can be simplified, as represented in Figure 5.4.

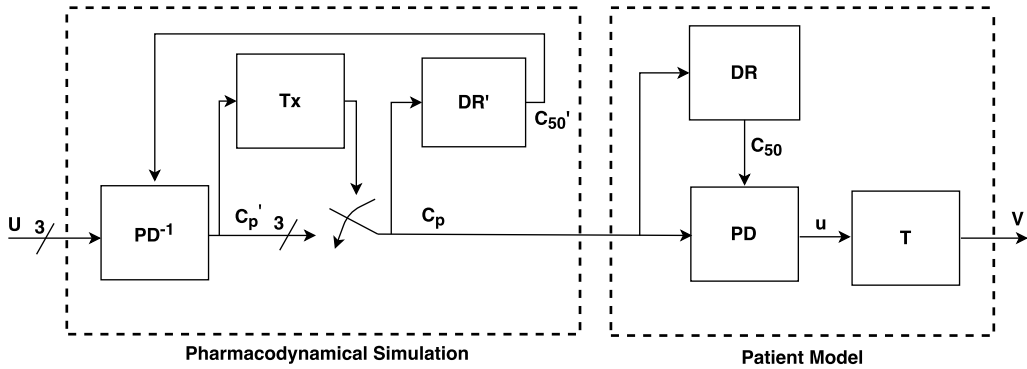


Figure 5.4: Composition of the Pharmacodynamical Simulation and Patient Model blocks with PK Control simplification.

By combining the structures presented in Figures 5.2 and 5.4, a final controller system for a fully known patient is achieved. Notice that, the input U has to be limited between 0 and 1. In this way, an input saturation is also necessary.

In the next chapter, this control framework is going to be adapted and developed in order to work also with varying patient models with a certain uncertainty $\Delta\theta_{PS}$. After that, the system operation is demonstrated in Chapter 9.

6

Multiple Model Adaptive Control

Contents

6.1	Architecture of Multiple Model Adaptive Control (MMAC)	43
6.2	Supervisor	44
6.3	Controller Bank	47

In Chapter 5, a control system for a known patient model was developed. However, almost all the complex systems are required to operate in distinct environments since plant models can be intrinsically inaccurate [105]. In oncology the uncertainty in the patient's behavior is significant not only at the beginning of therapy, when patient's characteristics are unknown, but mainly in its course, since the organism's response is time-variant [61]. In this way, this kind of models must be regulated by controllers that ensure an acceptable closed-loop performance in the presence of uncertainty, disturbances or noise that cannot be measured.

For models with large uncertainty, linear control theories, as pole placement or even LQR, cannot regulate the system in a satisfactory way, without an auxiliary mechanism, despite having full functionality, *i.e.* without a loss of performance, when the inaccuracy is relatively small. A controller should be designed in order to guarantee a robust stability and performance. However, this stability margin has limits and can deteriorate the performance. Usually, the controlled system is slowed down when the robustness of the stability is increased.

This problem led to the necessity of designing an adaptive control system sufficiently "smart" to operate in dynamic environments with a low degree of accuracy so as to yield an acceptable transient performance [106]. This controller must have the capacity of changing its behavior when variations in plant dynamics are perceived. Since those variations cannot be predicted, an online method for selecting or tuning the right controller has to be developed.

Multiple models can be used as a set of different models, each one describing a distinct environment or scenario. By using multiple models, control can then be made by switching to an appropriate controller depending on the performed analysis of the plant. The simplest way of choosing the closest model to the plant and the right controller to activate is by analyzing a scheduling variable, a process called gain scheduling [107]. However, for cases where the dynamics changes cannot be foreseen or there is no access to state, this technique is limited.

Multiple Model Adaptive Control (MMAC) overcomes this problem by using a supervisor, *i.e.* a mechanism that is capable of switching to the right controller by a three step process:

1. Exciting all the models of the bank by the manipulated variable in the plant input U_T ;
2. Continuously comparing models outputs \hat{y}_i with the actual plant output y , resulting in a performance index;
3. Activating the controller whose corresponding model yields the best performance index.

This supervised technique has led to the preference of use of MMAC instead of an exclusively adaptive mechanism [108], since MMAC has a faster adaptation, improving then the transient performance, moreover, it is a flexible and modular technique since the supervision is separated from the control.

In the next sections, the MMAC structure is explained as well as all the strategies, algorithms and considerations assumed.

6.1 Architecture of Multiple Model Adaptive Control (MMAC)

Assuming that the plant dynamics P is defined by a set of parameters p , one can consider $p \in S$, being S a closed and bounded set of parameter space with finite dimension. The objective of MMAC is to control the plant by switching between a finite set of models $M = \bigcup_{i=1}^N M_i$, being each model M_i characterized by a set of parameters \hat{p}_i , that also respect $\hat{p}_i \in S$, defined according to a convenient metrics. As performed in Subsection 5.1.1, all the models used in the MMAC are analyzed to confirm that all of them are controllable and observable.

It is considered that there exists a set of controllers $C = \bigcup_{i=1}^N C_i$, where C_i is a local controller designed in order to have a good closed-loop performance in $S_i \in S$, being S_i the neighborhood of the model parameter vector \hat{p}_i .

A switch between two different models in the parameter space is illustrated in Figure 6.1, where the system chooses the parameter vector \hat{p}_k , since the plant vector p belongs to its neighborhood S_k .

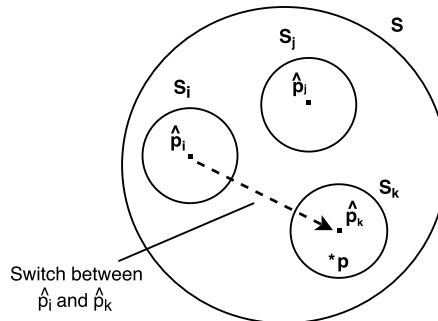


Figure 6.1: Representation in the parameter space S of the parameters vectors \hat{p}_i , \hat{p}_j , \hat{p}_k , and p . Adapted from [106].

Since the plant P is unknown, finding the model M_i that best fits the patient's dynamics is a role executed by the supervisor, that has as inputs the less toxic therapy effect U_T and the plant output y . Its output is the signal i^* , responsible for activating the controller C_{i^*} , which belongs to the controller bank, that is associated with the patient model M_{i^*} . This process is illustrated in the simplified MMAC architecture in Figure 6.2 and it is fully detailed in the next sections.

It is important to notice that the structure presented is the same as shown in Figure 5.1 but with the addition of the Supervisor block and the consideration of a Controller Bank instead of only one regulator.

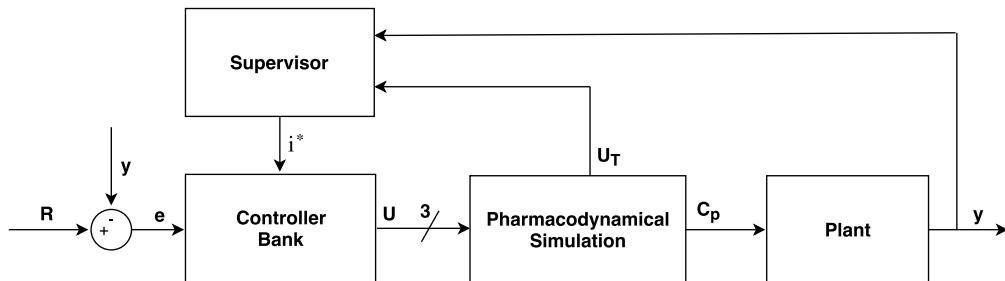


Figure 6.2: Simplified architecture of the MMAC.

6.2 Supervisor

As previously mentioned, the supervisor is the core behind MMAC strategy since it is the only block capable of making independent decisions. The supervisor decision making strategy is basically to choose, from time to time, for the output signal i^* , a value corresponding to the index i of the model M_i , whose performance index J_i is the smallest. Its architecture is represented in Figure 6.3.

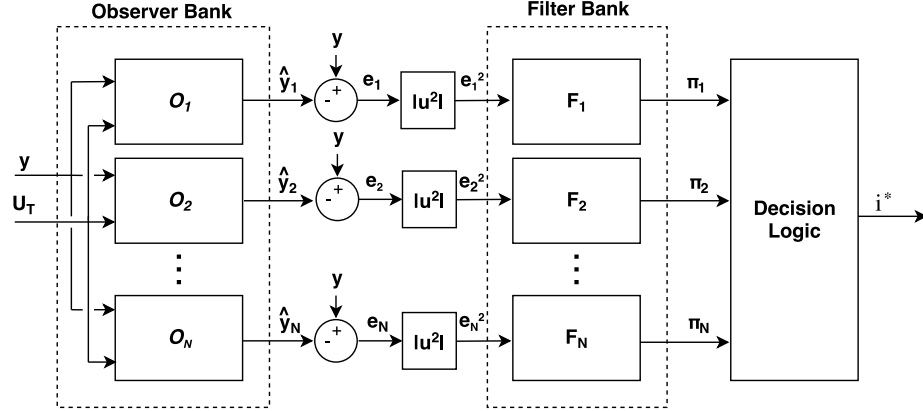


Figure 6.3: Architecture of the supervisor in the MMAC.

6.2.1 Observer Bank

The observer bank is the responsible for computing the output estimations \hat{y}_i for each of the N considered models. For that, it has as input the plant output y , and the signal U_T . This last signal is the estimation of the Pharmacodynamical Simulation for the variable u that is the input of the tumor growth model – Figure 5.4. Since u is not measurable, U_T works as an approximation of it.

The estimations of the state \hat{x}_i and the output \hat{y}_i are performed by the Kalman filter using, respectively, the equations (5.5) and (5.6). The matrix L was calculated using the same procedure as in Subsection 5.1.2, but considering $R_o = 10^6$ and $Q_o = 10^{-5}I$.

Since each model represents a certain parameterization of the model variables, in each estimation the state space matrices are going to be different, as well as the output y_i .

6.2.2 Filter Bank

Based on the models output estimations \hat{y}_i , a prediction error $\hat{e}_i = y - \hat{y}_i$ for each model M_i can be measured. The signal \hat{e}_i indicates how far the model is from the plant dynamics taking into account the input U_T . A filtration process can be established in order to build a signal that quantitatively compares the plant with the model's dynamics. Therefore, the prediction error \hat{e}_i , after computed, is squared in order to be always positive and to present a favorable shape. The filtered error signal π_i is calculated by filtering the squared signal \hat{e}_i^2 in order to smooth transactions and to remove high frequency components. A first-order low pass filter F_i is used, whose transfer function is given by

$$F_i = \frac{1}{1 + s/w_c}, \quad (6.1)$$

where $w_c = 2\pi f_c$. The cutoff frequency that has demonstrated better results was $f_c = 30 \text{ mHz}$.

In Figure 6.4, an example of the filtration process is illustrated, for four different models. The signal represented in Figure 6.4(b) is smoother and always positive which helps the decision logic to choose the right controller, avoiding possible errors due to the fast transactions of the prediction error.

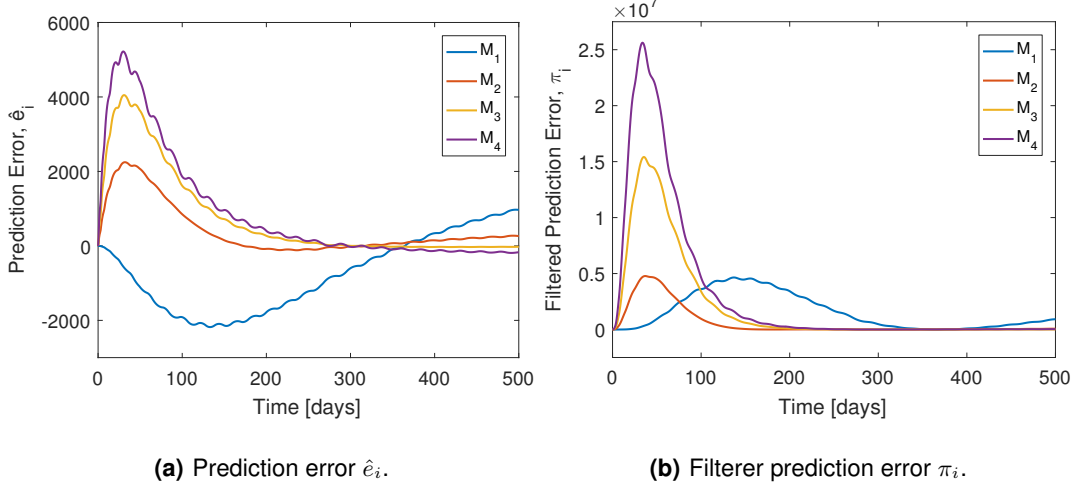


Figure 6.4: Correspondence between the prediction error \hat{e}_i and its filtration π_i .

6.2.3 Decision Logic

After obtaining the filtered signal π_i , a local controller can be chosen by using a decision logic, *i.e.* a network of connected information and knowledge that generates a final decision result. In this work, a three-step decision process is used by combining the following techniques: performance index, hysteresis and dwell time.

The performance index J_i is a cost function that evaluates which model should be chosen not only by looking for the current instant t , but also by balancing it with the past information. In previous works, this evaluation process has demonstrated great improvements in the transient response [109, 110]. In this way, a reliable and accurate model identifier can be built by using instantaneous and long-term empirical observations [109]. This feature is incorporated in the following equation

$$J_i(t) = \alpha\pi_i(t) + \beta \sum_{k=0}^K e^{-\lambda k} \pi_i(t-k) , \quad (6.2)$$

where K is the memory length, α and β determine, respectively, the importance of the current and past data, and λ is the forgetting factor. A large value of λ leads to a fast detection in the plant dynamics changes, however, concurrently to unnecessary switches due to disturbances. A small value of λ increases the delay of changes detection but prevents possible errors [111]. The values that demonstrated better results are $K = 300$ days, $\alpha = 1$, $\beta = 1$, and $\lambda = 0.65$. Important to notice is that a sampling time of 0.2 days were used due to computational limitations.

To prevent excessive and inappropriate arbitrarily fast switches, a hysteresis algorithm [112, 113] is used during the minimization of the performance index. Instead of simply minimizing at each instant the performance index, a hysteresis dead zone is considered. Therefore, switching takes place only if

$$\min_i J_i(t) < \delta J_i^{last}(t) , \quad (6.3)$$

where $J_i^{last}(t)$ is the last performance index and δ is the hysteresis constant, whose selected value was $\delta = 0.65$.

Chattering is avoided by using a dwell time condition [114, 115]. After a switch the system continues selecting the same model for a minimum amount of time τ_D , denoted by dwell time. By dwelling in each model for a certain interval, at least during that time, the same controller remains connected with the plant which prevents possible instabilities that can arise due to swift switching. Besides that, in [116], despite using a slightly different structure, additional stability conditions are guaranteed for three different scenarios:

Scenario 1 – System without noise, disturbances, and unmodelled dynamics;

Scenario 2 – System with bounded noise and disturbances and without unmodelled dynamics;

Scenario 3 – System with noise, disturbances, and unmodelled dynamics.

Hespanha *et al.* [116] assures that for **Scenario 1** all the signals belonging to the Supervisor are bounded for every initial condition and, thus, the model switching stops in finite time, *i.e.* the system tends to choose the model that best fits the plant in a finite interval.

For **Scenario 2**, by choosing a large value for τ_D , the stability margin of the global system tends to the smallest stability margin of the local controllers. In this way, in [116] it is guaranteed that for linear systems, a uniformly exponentially stability can be considered, *i.e.* there exists γ_1 and $\gamma_2 > 0$ such that

$$\|x(t)\| < \gamma_1 \|x_0\| e^{-\gamma_2(t-t_0)}, \quad (6.4)$$

where (t_0, x_0) represent the initial conditions, and γ_1 and γ_2 are constants independent of the initial conditions [117].

The situation is significantly different for **Scenario 3** because the analysis becomes more complex. However, the authors assure that the control algorithm is robust in the presence of plant dynamics that are not being taken into account in the model space.

The value for τ_D that showed better results in terms of stability, having thus a small number of switch errors, was $\tau_D = 30$ days. Simulations for various values of τ_D are shown in Chapter 9.

In the Figure 6.5, a computer diagram is illustrated, summarizing all the sequential steps performed by the decision logic.

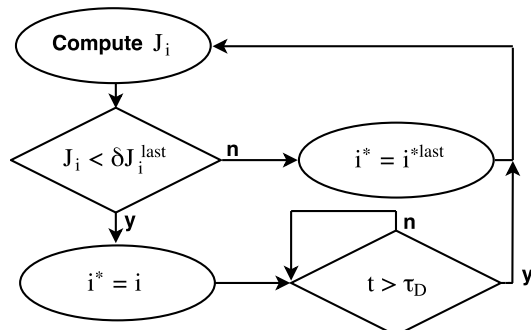


Figure 6.5: Computer diagram of the decision logic sequential process.

6.3 Controller Bank

The controller bank is a set of different controllers C_1, \dots, C_N , each one designed as mentioned in Section 5.1.2 by considering different patient models, being then a controller C_i optimized for a specific model M_i . In this way, the optimal control is always chosen by switching the activated controller C_{i^*} according to the switching signal i^* .

In Figure 6.6, a diagram of the controller bank composition is illustrated. In the following subsections this structure is going to be detailed. It is important to point out that each local controller C_i generates a set of three different signals. However, in order to simplify the explanations, from now on this set is going to be considered unitary.

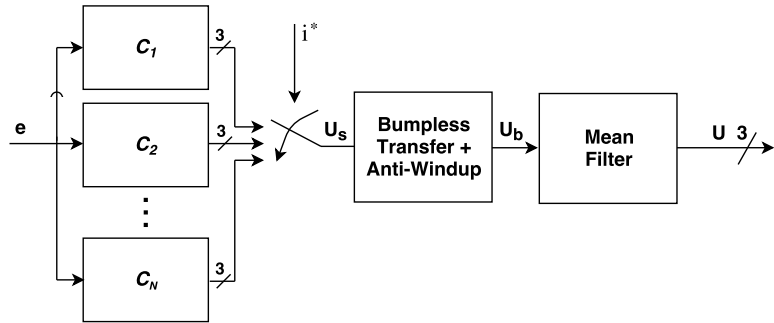


Figure 6.6: Architecture of the controller bank in the MMAC.

6.3.1 Bumpless Transfer and Anti-Windup

Each local controllers C_i is designed to work for a certain patient model or operating point and is expected to work optimally when the system enters its regime. When changes in the plant are detected, the current controller is switched to a new one with a much more satisfactory performance.

However, this ideal control process can be deteriorated by the switching since a degradation of the transient performance can be expected [118]. By swapping between one controller to another, abrupt changes in the manipulated variable U can occur resulting in doses that largely exceed the maximum values allowed. Bumpless transfer between different controllers can prevent this problem, for which several schemes have been developed in the literature and industrially implemented. From these, Turner and Walker [118] and Hanus *et al.* [119] works stand out.

In this work, the bumpless transfer problem is fixed by inserting after the switch an integrator common to all the controllers [107]. Therefore, if an abrupt change in U_s happens the integrator prevents U_b from drastically jump to higher values. The local controllers are thus generating increments that are going to be translated by the integrator into a smoother continuous signal U_b .

The addition of this integrator in the system has another implication since the local controllers design was performed without it. Therefore, the local controllers have to be redesigned by considering an augmented state space composed by the previously defined state x and the state of the integrator x_I . Since the integrator state x_I is exactly the variable U_b , the equations (5.3) and (5.4) can be modified, resulting in

$$\begin{bmatrix} \dot{x} \\ \dot{U}_b \end{bmatrix} = \begin{bmatrix} A & B \\ 0 & 0 \end{bmatrix} \begin{bmatrix} x \\ U_b \end{bmatrix} + \begin{bmatrix} 0 \\ 1 \end{bmatrix} U_s , \quad (6.5)$$

$$y = [C \ 0] \begin{bmatrix} x \\ U_b \end{bmatrix} , \quad (6.6)$$

where A , B and C are the previously defined state space matrices.

It is noticeable that the system composed by equations (6.5) and (6.6) is controllable but not observable. However, since U_b is computed in software, direct measurements are available, being only necessary to estimate the state x as is currently implemented. On the other hand, the matrices K and Q have also to be expanded for working with the new augmented system.

An actuator saturation has to be considered after the integrator, since the drug effect U must respect $U \in [0, 1]$. The actuator limits can be somehow achieved by the control variable leading the system to an open loop since the actuator is going to keep its maximum value independently of the system output. Besides that, when an integral action is used the control variable remains integrated leading to larger values. This process is called windup [104] and can cause large transients if the system is not correctly designed. In Figure 6.7 an illustrative example of integrator windup is shown.

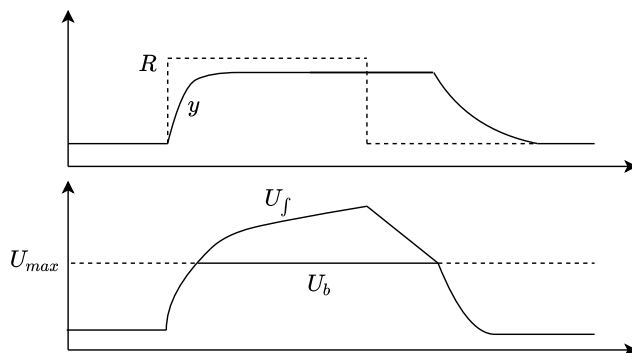


Figure 6.7: Illustrative example of a windup situation. Adapted from [120].

Figure 6.7 illustrates the process output y , its reference R , and the desired and true control signal, U_f and U_b , respectively. It is important to notice that the U_f is the signal exactly before the integrator. After the first reference change, the signal U_f increases until it reaches the upper limit U_{max} . This saturated value is not enough for eliminating the reference following error which leads U_f to keep increasing beyond the actuator limit, although U_b is stagnated. In this way, a difference between the true control input U_b and its desired value U_f is obtained [120].

When the reference R is lowered, the control signal U_f starts decreasing, but, due to the difference between the true and the desired value, this decrease is only noticed after a certain delay, causing a poor transient performance. In situations where the reference is too large, damped oscillations and large overshoots can also be obtained [120].

From the different anti-windup solutions, the scheme that is used in this work was introduced by Astrom and Wittenmark [121] and is shown in Figure 6.8. An extra feedback signal is added that measures the error e_s between the desired and the true control signal. The signal e_s is then fed back to the integrator through the gain $\frac{1}{T_W}$, being the integrator input given by

$$U_f = U_s - \frac{1}{T_W} e_s . \quad (6.7)$$

When there is no saturation, the error e_s is zero having no effect in the operation. However, when it is not null, the extra feedback path tries to drive the integrator input to zero, resetting the integrator so that the controller output is at the saturation limit, which prevents it from winding up.

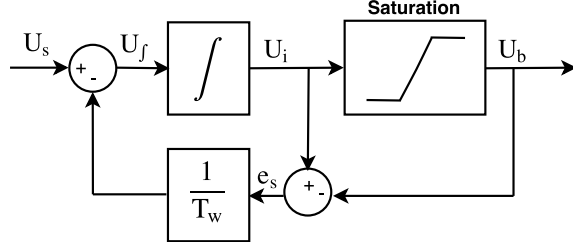


Figure 6.8: Architecture of the bumpless transfer scheme combined with anti-windup.

The integrator is reset at a rate dependent of the time constant T_w , so-called tracking-time constant that influences the way the anti-windup system works as it is represented in Figure 6.9.

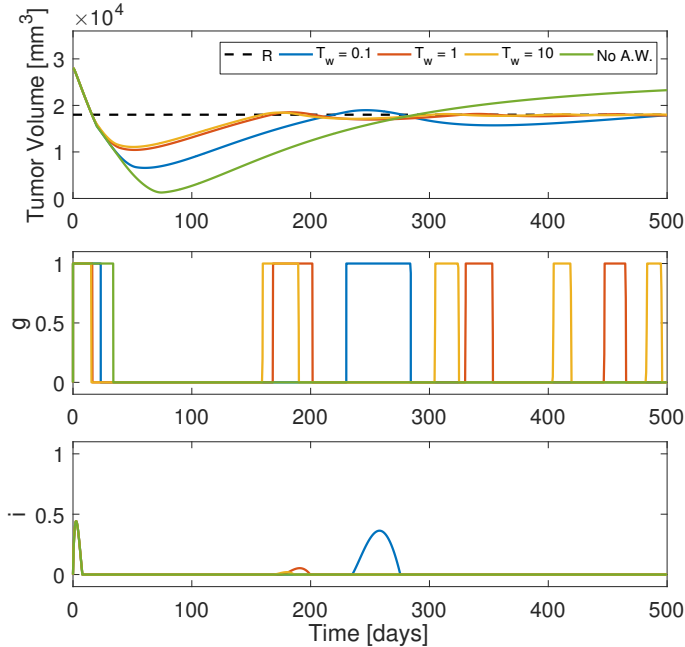


Figure 6.9: Illustration of the effect of the variable T_w in the anti-windup system.

In Figure 6.9, the system is trying to follow a constant reference R , what leads the input $g(t)$ to be always maximum, when the following error e is positive, or minimum, otherwise. For the situation where the anti-windup system is not implemented – green curves – the tumor volume does not correctly follow R , due to the large values of U_f that delay so much the system response that it only has the ability to act at the beginning of therapy. On the contrary, when the anti-windup scheme is considered, the system has a better response. The value used in this work is $T_w = 10$ that represented the best tested scenario.

In Figure 6.10 an example of the bumpless transfer and anti-windup system operation is illustrated.

As expected, the U_b curve is always between its allowed limits and does not follow U_s curve behavior during that interval because of the integral action. The integral action makes the U_b curve

smoother, preventing large bumps. Aside from that, the delay between U_s and U_b during the falling edges is not accentuated due to the anti-windup action that resets the integrator.

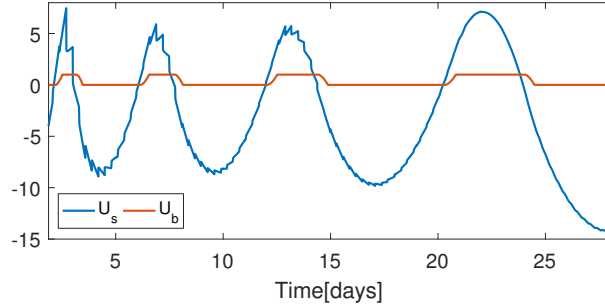


Figure 6.10: Example of the bumpless transfer and anti-windup system operation.

6.3.2 Mean Filter

Despite the inclusion of the bumpless transfer, there may still exist situations in which the system is not able to prevent the occurrence of peaks. Example of this situation is a switch between two models that are very distinctive. The bumpless transfer is capable of smoothing these peaks but not of removing them. In this way, a mean filtration was included.

The filter is based on a cumulative moving average that calculates for each time instant t_n the mean of all the iterations between the first instant t_0 and the previous one t_{n-1} . In this way, the drug effect for the time instant n , $U^{(n)}$, is given by

$$U^{(n)} = \frac{U_b^{(n)} + nU^{(n-1)}}{n}, \quad (6.8)$$

where $U_b^{(n)}$ is the output of the bumpless transfer and anti-windup system, and $U^{(n-1)}$ is the previous value of the drug effect U . In Figure 6.11, an example of this kind of filtration with a sampling time of $t_s = 0.3$ days is illustrated where the peaks are completely removed.

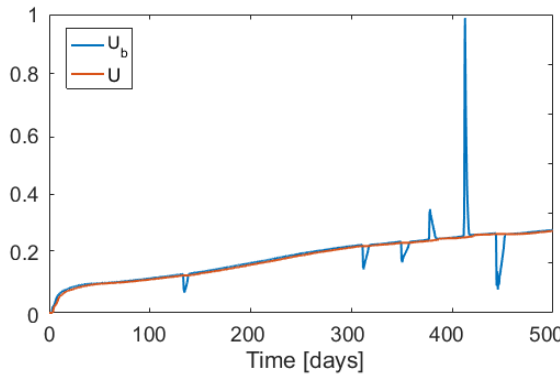


Figure 6.11: Example of mean filtration for a sampling time of $t_s = 0.3$ days.

It is worth noticing that the mean filtration showed better results when compared with the utilization of a median filter or a rate limiter, solutions that were also tested.

7

Model Clustering

Contents

7.1 Model Sensitivity Analysis	53
7.2 Vinnicombe Metric	54
7.3 Clustering Methods	55
7.4 Results	57

There exist some degrees of freedom for the designer in the specified MMAC architecture, for example concerning the model bank composition and whether to use fixed or adaptive models.

Adaptive models result from the use of online identification or learning methods. These methods generate models by computing at every instant the parameter vector \hat{p}_i due to an analysis of the plant input U and output y . In this way, a convergence to the neighborhood of the plant parameter vector p is expected. However, when there are changes in the plant dynamics, the parameter vectors have to be initialized having impact on the system transient performance.

This problem does not occur in the fixed models and, apart from that, they are computationally more efficient, since only the models outputs \hat{y}_i are calculated. On the other hand, to achieve the same steady state asymptotic accuracy as achieved by only one single adaptive model, a large number of fixed models is usually necessary [106].

The choice of the number of models, their selection and distribution in the parameter space S are design issues crucial for achieving a good performance. With prior information, as past experience, actual measurements, and physical limitations, some knowledge about S can be obtained helping the design decisions. By having this kind of information, an ideal model bank can be obtained where at least one fixed model is closer to each hypothesis of plant dynamics. However, due to computational limitations a bounded model bank is required, which suggests alternative methods to distribute the N fixed models. The simplest way is to locate the models uniformly in the parameter space S . Another solution is to distribute more models in highly sensitive zones.

In this work, it is essentially intended to use an algorithm where the controller bank is smaller than the model bank, *i.e.* where $N_c \ll N$, being N_c the number of local controllers. Following the work of Oliveira *et al.* [122], it is expected to select a set of local controllers C_j^c , with $j = 1, \dots, N_c$, that best cover all the models M_i , where $i = 1, \dots, N$. For that, clustering algorithms have to be implemented in order to agglomerate similar models into a single cluster c_j . The centroids of the clusters c_j form a new set of models M_j^c , from which the local controllers C_j^c are going to be designed. The clustering process is illustrated in the Figure 7.1 in \mathbb{R}^2 , where a set of N models M_i , represented by the parameters θ_1 and θ_2 , is partitioned into five clusters c_j with centroids M_j^c , where $j = 1, \dots, 5$.

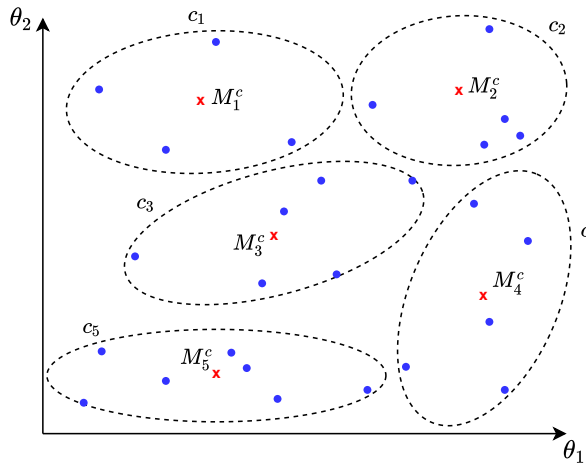


Figure 7.1: Clustering illustration for a set of models M_i – blue dots – resulting in five clusters M_j^c – red crosses.

Due to clustering, the candidate models M_j^c are located in highly dense zones of models. Therefore, M_j^c symbolize the models that are essential for the control operation, from which the controllers C_j^c are going to be designed. In this way, by using a small number of controllers, N_c , problems related with excessive switching does not occur. Aside from that, it is computationally more efficient to consider a small number of controllers instead of a linear proportionality between the set of models M_i and its respective controllers.

In the following sections, a sensitivity analysis of the patient model parameters is going to be performed, as well as a description of the metric used for the clustering, the implemented algorithms and a comparison between them.

7.1 Model Sensitivity Analysis

Sensitivity analysis aims to study how the variation of a model parameter affects the system output. In other words, it evaluates quantitatively what is the influence of each model parameter on the observed variable.

If a small variation in a parameter results in a large difference in the output, the system is sensitive to that parameter. This kind of information is useful for simplifying high order models or to help the model identification process. In this work, the sensitivity analysis is going to be used to choose from the set of 11 parameters of the patient model – Subsection 2.2.3 – the 2 most sensitive parameters. Therefore, clustering is then going to be performed based on these parameters because the largest differences between the models of the model bank can be detected based on them.

Following Coito *et al.* work [123], the patient model can be described as

$$\dot{x} = f(x, u, \theta) , \quad (7.1)$$

where $\theta \in \mathbb{R}^{11}$ is the parameter vector, x is the state vector, and u is the model input.

Deriving equation (7.1) with respect to the parameter θ_i , where $i = 1, \dots, 11$, results

$$\frac{\partial}{\partial \theta_i} \dot{x}(t, \theta) = \frac{\partial f}{\partial x} \frac{\partial x}{\partial \theta_i} + \frac{\partial f}{\partial \theta_i} . \quad (7.2)$$

Changing the order of derivatives, the following equation arises

$$\frac{d}{dt} \left(\frac{\partial x}{\partial \theta_i} \right) = \frac{\partial f}{\partial x} \frac{\partial x}{\partial \theta_i} + \frac{\partial f}{\partial \theta_i} , \quad (7.3)$$

that can be simplified by considering the definition of sensitivity, $S_i = \frac{\partial x}{\partial \theta_i}$, resulting in

$$\frac{d}{dt} S_i = \frac{\partial f}{\partial x} S_i + \frac{\partial f}{\partial \theta_i} . \quad (7.4)$$

The differential equation (7.4) represents the state sensitivity $S_i = (S_{V_i}, S_{K_i}, S_{I_i})$ as a function that varies with time and that depends on the initial conditions (x_0, u_0, θ_0) . By integrating it, simulations of the model sensitivity can be performed for different initial conditions. In Figure 7.2 an example is illustrated for the case where the initial conditions correspond to the equilibrium point in absence of therapy.

From the 11 parameters, only 3 have substantial influence – μ_I , β and d – in the model, since for 8 parameters the sensibility S_i is close to zero. For simulations with distinct initial conditions, the results illustrate the same sensitivity disparity between parameters. For this reason, it was chosen to use in the implemented clustering algorithm the parameters μ_I and β .

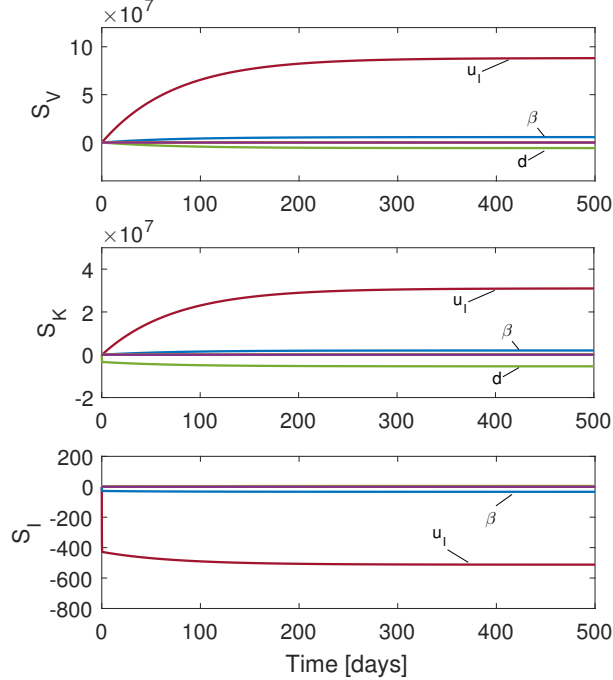


Figure 7.2: Sensitivity of the model as a function of time, for $V_0 = 28000.4 \text{ mm}^3$, $K_0 = 29528.1 \text{ mm}^3$, $I_0 = 0.013$ and $u_0 = (0, 0)$.

7.2 Vinnicombe Metric

An important factor regarding the classification and agglomeration of models is the choice of a good metric, *i.e.* a measurement of the closeness between linear time-invariant models [124]. If two models M_i and M_j , with $i \neq j$, are called similar by a metric, then if a controller stabilizes M_i , it must do the same with M_j , and the inverse process must work as well.

Since the Euclidean distance does not contain the desired properties, El-Sakkary [125] developed the *gap* metric in order to study the robustness of the stability of feedback systems. Later, Vinnicombe [126] improved the *gap* metric creating the *v-gap*, or the so called Vinnicombe metric. The *v-gap* metric has the same topology as the *gap* metric, although with more desirable properties than the *gap* metric, mainly because it gives less conservative robust stability results. More precisely, if the Vinnicombe metric shows that two models are distinct, then a controller that gives satisfactory results for one model will behave poorly or even destabilize the other model. In this way, the Vinnicombe metric is more relevant than the *gap* metric for the control domain [124].

Considering two models M_i and M_j , that are described by a transfer function with the same number of inputs and outputs, the Vinnicombe metric is then given by

$$\delta_v(M_i, M_j) = \|(I + M_j M_j^*)^{-1/2} (M_j - M_i) (I + M_i^* M_i)^{-1/2}\|_\infty , \quad (7.5)$$

where I is the identity matrix. The Vinnicombe metric can take values between $0 \leq \delta_v(M_i, M_j) \leq 1$.

If $\delta_v(M_i, M_j) = 0$ the models have the same composition. On the other hand, $\delta_v(M_i, M_j) = 1$ means that both models are very distinctive. In this way, values closer to 0 indicate that a controller designed for M_i can also stabilize M_j , having additionally similar closed loops gains.

Since this work deals with a two-input model, two transfer functions are obtained, meaning that two Vinnicombe metrics are available, one for each input. In the Section 7.4 this topic is approached.

7.3 Clustering Methods

Clustering is the unsupervised classification of patterns in groups, in which their elements should share common characteristics. Aside from being an unsupervised method, since there is no available knowledge of past classification results, clustering is also a nonparametric class of algorithms.

Before applying the clustering methods, a model data set is created. In this way, N values for the variables β and μ_I are generated by a log-normal distribution, creating combinations of values that result in N different patient models. It is worth to notice that those values are generated between the acceptable intervals $\beta \in [0, 0.05]$ and $\mu_I \in [0, 0.003]$ that were defined in accordance with the considered clinical results – Appendix A. In this way, each model can be represented in \mathbb{R}^2 by the referred parameters, since the remaining model parameters assume the values described in Table 2.1.

In this work, three different clustering methods are used. The first one is an intuitive partition of the model data set used as a basis for comparison with the other algorithms. The second method is a partitional clustering algorithm, known as k -means, in which a partition of data is obtained by optimizing a criterion function. The third technique is called complete-linkage, a hierarchical clustering in which a dendrogram is used to successfully classify and agglomerate models.

In the following subsections these algorithms are fully described.

7.3.1 Intuitive Clustering

In the intuitive clustering algorithm the data set is "intuitively" divided into N_c clusters, meaning that a visual and rough division is performed in order to create N_c groups with no overlap.

For each cluster c_i , a model is randomly chosen to be considered the centroid M_i^c of that class.

To guarantee stability conditions, the controller associated with each centroid M_i^c is connected to all the models belonging to the cluster c_i , and the respective closed-loop poles are computed [122]. If there exist unstable closed-loop poles (with negative real part) in at least one model of the cluster c_i then another model is chosen to be the cluster centroid. This process is repeated until the controller associated with the centroid M_i^c can stabilize all the models of c_i . In the last case, the clusters disposition has to be reformulated to achieve the desired results.

In the nutshell, the intuitive clustering is a three step process composed by the following steps:

- 1. Clusters Partition** – Visual and rough partition of N_c clusters;

- 2. Centroids Selection** – Random choice of N_c centroids;
- 3. Closed-Loop Poles Verification** – It is verified if the controller C_i^c associated with the centroid M_i^c stabilizes all the models belonging to c_i .

7.3.2 K-Means

The k -means algorithm is a reliable clustering procedure widely used in the literature, being originally developed by Macqueen [127] to compute the optimal partition, however, in general, this only happens in special cases.

It consists of starting with N_c clusters, each one composed by a single model randomly chosen. Thereafter, in each iteration all the models M_i compute the distance to all the centroids M_j^c and then they are added to the nearest c_j . After that, the centroids are updated by adjusting the mean of each cluster.

In this work, the distance evaluation is performed with the Vinnicombe metric and an additional verification at the end of each iteration is added to ensure the conditions of stability. The following topics summarize the k -means process:

- 1. Centroids Initialization** – Random initialization of N_c centroids;

Loop: (exit condition: $M_j^c = M_{j\text{last}}^c$, $\forall j$, $j = 1, \dots, N_c$)

- 2. Classification and Clustering** – The similarities between each model M_i and the centroids M_j^c are computed through the Vinnicombe metric and each M_i is classified into the nearest cluster c_j , according to

$$M_i \in c_j : j = \min_j \delta_v(M_j^c, M_i) ;$$

- 3. Centroids Update** – After the clusters recomposition, each centroid M_j^c is updated into

$$M_j^c = \frac{1}{|c_j|} \sum_{M_i \in c_j} M_i ;$$

- 4. Closed-Loop Poles Verification** – It is verified if the controller C_j^c associated with the centroid M_j^c stabilizes all the models belonging to c_j .

This four-step process ends when there are no modifications in the centroids M_j^c of all the clusters c_j in the **Step 3**, meaning that the best possible solution has been achieved.

7.3.3 Complete Linkage

The complete linkage algorithm, developed by King [128], differs from the last method in the way the similarities between a pair of clusters are characterized. By considering, at the beginning, each model as a cluster and sequentially combining it in larger clusters, a dendrogram can be drawn. At each step, the two clusters separated by the smallest distance are fused into a single cluster. The notion of distance between clusters in the complete linkage is what differentiates it from the other hierarchical methods. In this algorithm, the distance between clusters is measured as the distance

between the model M_i of the cluster c_i and M_j from cluster c_j , with $i \neq j$, that are farthest away from each other.

The process executed by the complete linkage method is described as follows:

- 1. Distance Matrix Initialization** – A matrix $D(c_i, c_j)$ is computed in order to measure the distances between all the pairs of clusters c_i and c_j , with $i \neq j$, through the Vinnicombe metric, since initially all the models are considered as single clusters;

Loop: (exit condition: $\#c_i = N_c, \forall i$)

- 2. Classification and Clustering** – The pairs of clusters that have the minimum distance are fused into the same cluster. In this way, all the models M_i from the cluster c_i are going to belong to c_j , following

$$\forall M_i \in c_i, \quad M_i \in c_j : j = \min_j D(c_i, c_j) ;$$

- 3. Distance Matrix Update** – The distance matrix is updated measuring the maximum distances between pairs of clusters c_i and c_j , being the notion of distance $D(c_i, c_j)$ given by

$$D(c_i, c_j) = \max_{M_i \in c_i, M_j \in c_j} \delta_v(M_i, M_j) ;$$

- 4. Centroids Computation** – At the end of the loop, the centroids have to be computed, using

$$M_j^c = \frac{1}{|c_j|} \sum_{M_i \in c_j} M_i ;$$

- 5. Closed-Loop Poles Verification** – It is verified if the controller C_j^c associated with the centroid M_j^c stabilizes all the models belonging to c_j .

The algorithm ends when the desired value of clusters N_c has been achieved in **Step 2**.

7.4 Results

The classes of models obtained for the three clustering algorithms are illustrated in the Figure 7.3 for a data set of $N = 100$ models and $N_c = 6$ clusters. In the Table 7.1, the quality of the clustering is evaluated through three criterion: number of models M_i in each cluster c_i , mean of distances d_c between M_i and its clusters, and the worst case of the same distance d_c . It is worth to notice that in the presented results the Vinnicombe metric for the first model input g was used.

When compared with the intuitive clustering, the k -means seems to have a greater performance in the test with 6 clusters, since the latter has almost all the values of the mean of d_c lower or similar than the same values in the first method. This aspect is evidenced when the mean of the last referred measure is performed – the last row in Table 7.1 – for all the clusters, being this value 21.28 % lower than in the case of the intuitive method. Aside from that, the worst cases of d_c in each cluster are always smaller for the k -means with the exception of cluster c_4 , whose elements are quite apart as seen in the Figure 7.3(b)

The complete linkage is the method that showed better performance, having substantial differences compared with the other methods. This algorithm tends to make partitions in areas where the models are further apart, as it is the case of the singles model clusters c_5 and c_6 . On the other hand, it creates clusters with a large number of elements in areas where they are closer to each other. Aside from that, the complete linkage is computationally more efficient since the Vinnicombe distances only have to be computed once, and not in every iteration as in k -means due to the required comparisons between all the models and the centroids.

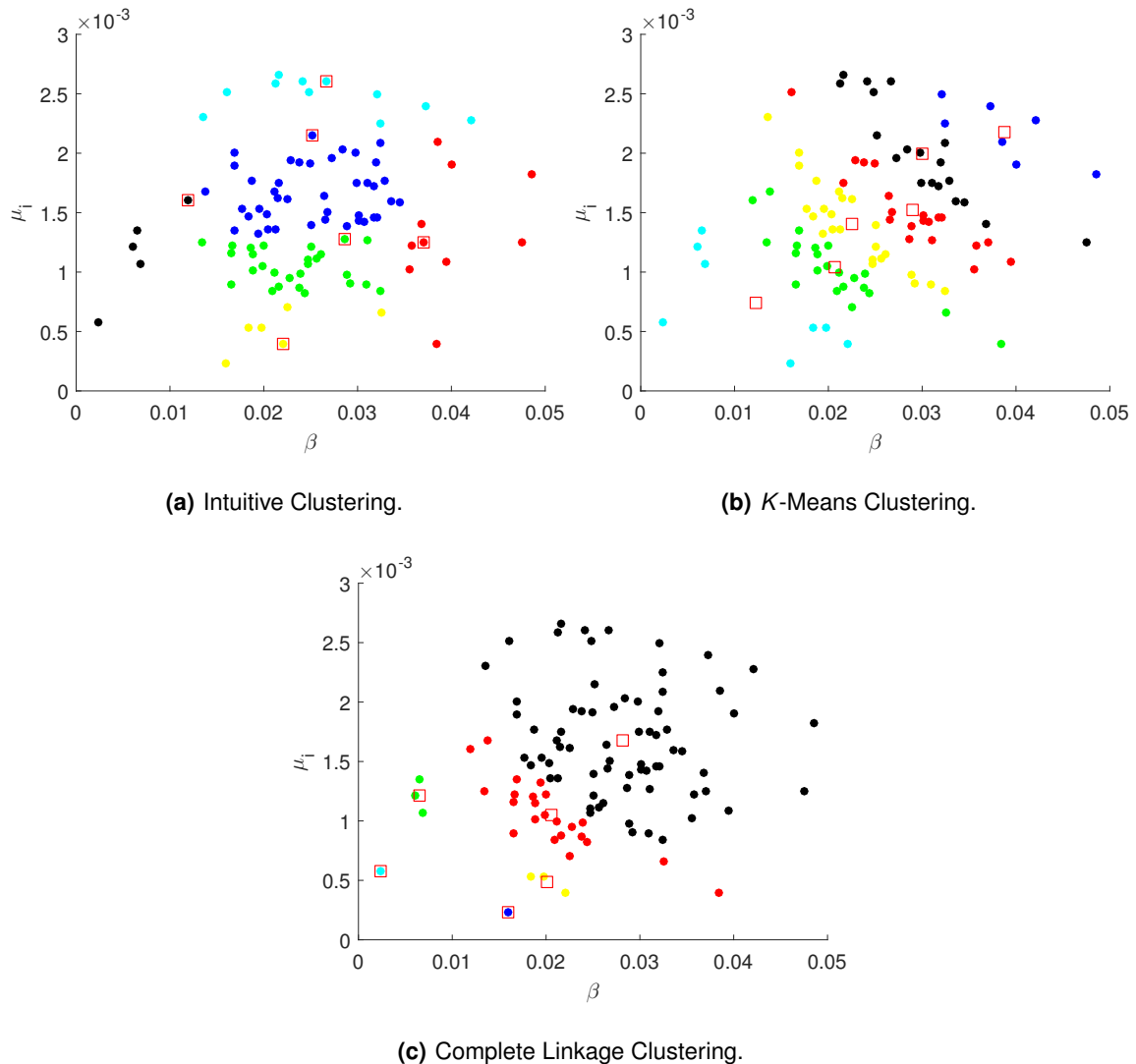


Figure 7.3: Clustering of 100 different models into 6 clusters using 3 different methods.

Table 7.1: Clustering results – number of models in each c_i , mean and worst distances of all the models to its centroid – for the three methods with $N_c = 6$ clusters. Last row shows the sum of models and the mean value of the Mean d_c and Worst d_c .

c_i	Intuitive			K-Means			Complete Linkage		
	# M_i	Mean d_c	Worst d_c	# M_i	Mean d_c	Worst d_c	# M_i	Mean d_c	Worst d_c
c_1	5	0.0065	0.0096	19	0.0044	0.0178	69	0.0058	0.0204
c_2	6	0.0046	0.0105	24	0.0040	0.0099	3	0.0014	0.0020
c_3	10	0.0038	0.0116	20	0.0044	0.0130	23	0.0040	0.0178
c_4	27	0.0064	0.0153	22	0.0042	0.0178	3	0.0003	0.0004
c_5	41	0.0051	0.0114	7	0.0042	0.0099	1	0	0
c_6	11	0.0076	0.0154	8	0.0068	0.0099	1	0	0
	100	0.0057	0.0123	100	0.0047	0.0130	100	0.0019	0.0068

By looking only at the partition in Figure 7.3, one can see that the k -means algorithm agglomerates the models in a more uniformed way, possibly yielding a better representation of the sample. The complete linkage by having single clusters is not really partitioning the dense zones of models. However, only the results of the control algorithm can say which algorithm is the best for the developed control framework.

To verify the influence of the number of clusters, the same tests were performed for $N_c = 12$ clusters and the results are described in the Table 7.2 and illustrated in the Figure 7.4.

Table 7.2: Clustering results – number of models in each c_i , mean and worst distances of all the models to its centroid – for the three methods with $N_c = 12$ clusters. Last row shows the sum of models and the mean value of the Mean d_c and Worst d_c .

c_i	Intuitive			K-Means			Complete Linkage		
	# M's	Mean d_c	Worst d_c	# M's	Mean d_c	Worst d_c	# M's	Mean d_c	Worst d_c
c_1	5	0.0026	0.0054	8	0.0068	0.0099	1	0	0
c_2	5	0.0029	0.0042	22	0.0042	0.0178	1	0	0
c_3	1	0	0	20	0.0045	0.0099	2	0.0004	0.0004
c_4	1	0	0	11	0.0036	0.0092	1	0	0
c_5	21	0.0038	0.0075	12	0.0040	0.0090	2	0.0007	0.0007
c_6	6	0.0015	0.0032	1	0	0	1	0	0
c_7	18	0.0045	0.01	10	0.0028	0.0060	3	0.0084	0.0126
c_8	23	0.0048	0.0094	4	0.0061	0.0121	7	0.0029	0.0053
c_9	7	0.0089	0.0131	2	0.0002	0.0002	13	0.0033	0.0133
c_{10}	4	0.005	0.0097	4	0.0015	0.0030	3	0.0010	0.0015
c_{11}	7	0.0022	0.0043	1	0	0	4	0.0035	0.0043
c_{12}	2	0.0012	0.0012	3	0.0040	0.0059	26	0.0053	0.0162
	100	0.0031	0.0057	100	0.0033	0.0074	100	0.0025	0.0057

The intuitive and k -means methods improved their performance in this test. However that did not happen for the complete linkage. The mean of the worst d_c for all the clusters is 17.24 % smaller than the one in the 6 clusters test, which indicates that the addition of new clusters allowed to subdivide the cluster with 69 models into a set of clusters with models that are even closer to each other. However, the mean of d_c is slightly bigger in the last test mainly because of the cluster c_3 , whose models are somewhat distant from their centroid.

The same tests were performed by using the Vinnicombe metric for the second input i and for the mean of the Vinnicombe with both inputs. However, the results obtained were equal in the case of the

k -means and 35 % worse for the complete linkage. For this reason, the results are not shown and it was chosen to use the first metric in the simulations of the MMAC algorithm.

After the clustering process, the initial model data set is turned into a data set of N_c models – the centroids – that represent classes of models with similar properties. This clustered data set is going to be combined with the MMAC algorithm in order to simplify the model and controller banks. The simulations are illustrated in Chapter 9.

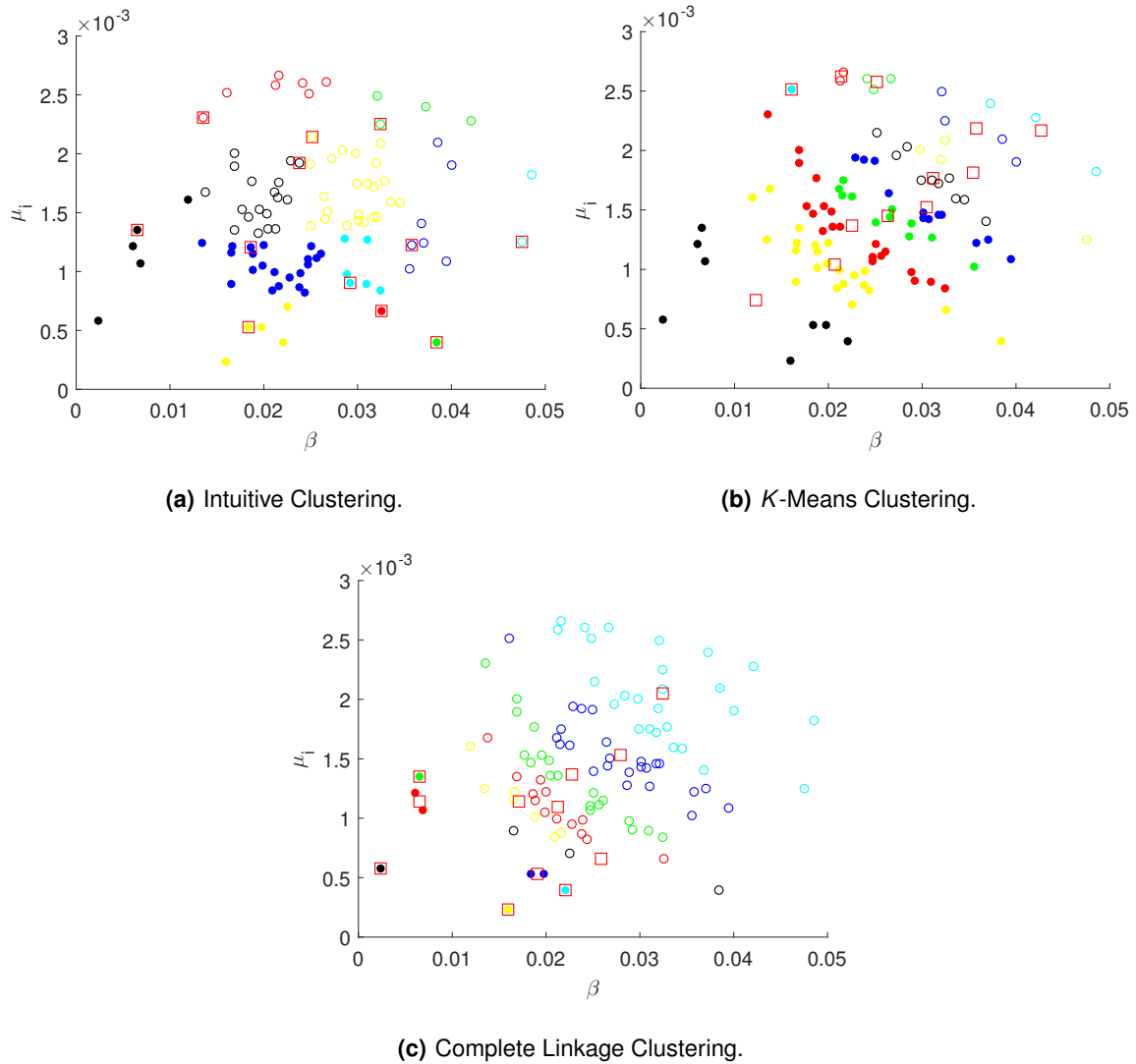


Figure 7.4: Clustering of 100 different models into 12 clusters using 3 different methods.

8

Offline Bolus Therapy Design

The therapy design approach developed does not consider the use of IV bolus, since it generates a drug concentration directly and not a set of IV bolus. In this chapter, it is intended to develop an offline algorithm to design IV bolus therapies, that is, to generate a set of N_b bolus based on a previous computation of a drug concentration C_p .

Ideally, this process would be executed in parallel with the computation of the MMAC algorithm. However, in this work it was chosen to make it in offline mode due to the available time frame.

A therapy with N_b IV bolus, each one with amplitude D_i , with $i = 1, \dots, N_b$, separated by equidistant intervals of t_i is given by

$$d(t) = \sum_{i=0}^{N_b-1} D_i \delta(t - t_i), \quad (8.1)$$

where $\delta(t)$ is the Dirac function.

The drug concentration in the organism $C_p(t)$ resulting from the bolus administration can be calculated based on the linear PK model – Section 3.1 – as it is illustrated in Figure 8.1 for the PK state space representation x_{PK} .

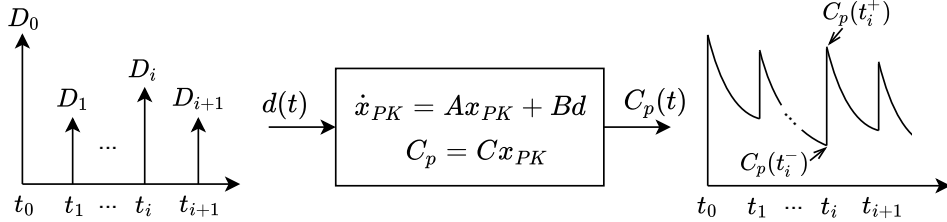


Figure 8.1: State space representation of the linear PK model, having as input a set of N_b bolus.

To determine the drug concentration in the moment exactly after the bolus administration, t_i^+ , information prior to the administration, that is, at the instant t_i^- , can be used. In this way, and taking into account the solution of the state space equations, it is intended to determine $x_{PK}(t_i^+)$, given the initial condition $x_{PK}(t_i^-)$, resulting in

$$x_{PK}(t_i^+) = e^{A(t_i^+ - t_i^-)} x_{PK}(t_i^-) + \int_{t_i^-}^{t_i^+} e^{A(t_i^+ - \tau)} B d(\tau) d\tau. \quad (8.2)$$

By joining equations (8.1) and (8.2), taking advantage of the Dirac properties, and considering $t_i^+ - t_i^-$ as a very small interval, equation (8.2) can be simplified into

$$x_{PK}(t_i^+) \simeq x_{PK}(t_i^-) + BD_i. \quad (8.3)$$

The drug concentration $C_p(t)$ at the instant t_i^+ is then given by

$$C_p(t_i^+) \simeq Cx_{PK}(t_i^-) + CBD_i. \quad (8.4)$$

With the computation of the drug concentration C_p for t_i^+ , it is possible to discover the optimal sequence of bolus D_i for every instant t_i , where $i = 1, \dots, N_b$. This optimal sequence leads the cumulative mean of concentration for the bolus therapy, $\hat{C}_p(t_i, D_i)$, to fit best the desired drug concentration designed by the developed algorithm $C_p^*(t)$.

This problem can be described by the following expression

$$\min_D \sum_{j=0}^{N_b-1} \left(C_p^*(t) - \hat{C}_p(t_i, D_i) \right)^2, \quad (8.5)$$

where $D = [D_1, \dots, D_{N_b}]^T$.

An algorithm was developed that chooses, for every instant t_i , the best dose D_i , given an administration periodicity d_g and a desired concentration C_p^* . For that, it compares, for every interval between 2 consecutive bolus $[t_i, t_{i+1}]$, all the possible means of drug concentration $\hat{C}_p(t_i, D_i)$ resulting from the administration of all possible doses D_i , with the desired value of mean of concentration C_p^* . In this way, a sequence of bolus D is obtained. It is worth noticing that the allowable doses intervals are those referred in Section 3.4. Aside from that, although the above description was made only for one input, it can be generalized for multiple-drug therapies as the one considered in this work.

Figure 8.2 illustrates an example of the algorithm execution, where C_p^* is a constant curve of bevacizumab with 5 mg/kg and the periodicity is $d_g = 21 \text{ days}$.

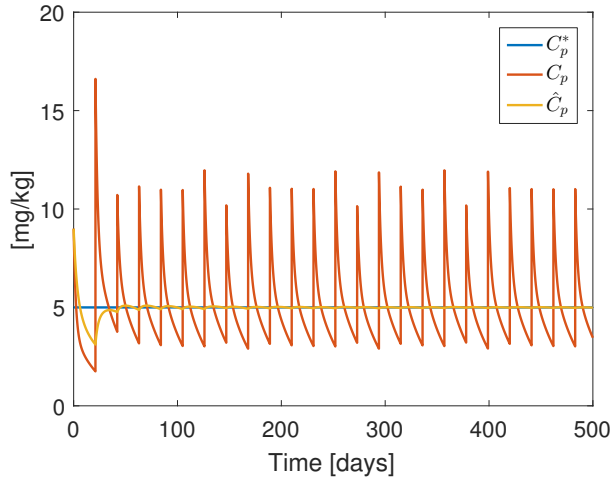


Figure 8.2: Offline design of a bolus therapy for a constant reference and $d_g = 21 \text{ days}$.

As it is possible to see, the obtained reference tracking is quite satisfactory, having in total 24 bolus with amplitudes that vary between 8 and 16 mg/kg . In the Chapter 9 more simulations are going to be performed with concentrations C_p^* that are directly obtained through the MMAC algorithm.

As mentioned before, ideally this process would be executed in real time. Nevertheless, an approximate version to the real time can be developed. Since it has to have a desired drug concentration C_p^* available for at least d_g days, the MMAC algorithm can be executed in intervals of d_g days, after which a bolus D_i could be computed. In this way, a real time solution with a d_g days delay would be obtained.

9

Results and Simulations

Contents

9.1 Test A – Model Switch	66
9.2 Test B – Model Linear Time Varying	73
9.3 Test C – Model Non-Linear Time Varying	79

In order to test the reliability of the control system described in the previous chapters, several simulations were performed using *MATLAB R2016a* and *Simulink*. Those simulations were computed for a model data set distinct from the test set used in Chapter 7 for testing the clustering process.

The quality of the results is evaluated not only through a visual inspection of the plots but also through quantitative metrics. Those comparison metrics include the number of true and false switches, the time delay τ between the reference model and the true switch, and also information related with the reference following, described by the Mean Absolute Percentage Error (MAPE), that is given by

$$MAPE = \frac{100}{N} \sum_{i=1}^N \left| \frac{R_i - V_i}{R_i} \right| , \quad (9.1)$$

where R is the reference and V the tumor volume output of the system.

In the following sections the system is tested for different combinations of algorithms and parameters. In particular, the control system in combination with the k -means and the complete linkage algorithm of 6 and 12 clusters is tested. Aside from that, offline bolus therapies are computed for different periodicities d_g and d_i , distinct values of the dwell time τ_D are tested, error $\Delta\theta_{PS}$ in the Pharmacodynamical Simulation is added, and noise n and disturbance d are included.

The intuitive clustering is not approached in this chapter since it was only used as a base for comparison with the other clustering methods. Aside from that, its results are quite similar with the ones from k -means.

9.1 Test A – Model Switch

This test simulates a case of a patient in which the dynamics, described by the equations summarized in Section 4.1, changes twice over time. The initial patient dynamics corresponds to the model M_{14} , but at the instants $t = 100$, and $t = 300$ days the dynamics changes instantaneously to the models M_{82} and M_{65} , respectively.

The models M_{14} , M_{82} , and M_{65} are represented with a black star in Figure 9.1, as well as the partitions of the model data set for the k -means with 6 and 12 clusters, and for the complete linkage also with the same number of clusters. The system simulations obtained for each of the four algorithms are illustrated by Figures 9.2, 9.3, 9.4, and 9.5 and the evaluation metrics are described in Table 9.2. It is worth pointing out that, by default, the model initially chosen is M_1 .

All the four simulations present satisfactory results, with levels of MAPE around 3 % and low toxicity levels. What directly stands out from the simulations is the large number of false switches for the 12 clusters' algorithms with 5 and 3 false switches, respectively, for k -means and complete linkage. This case happens because the computed centroids are closer to each other, which means that a small variation in the plant dynamics can result in a big oscillation in the selected model, until achieving the stabilization of the control system. This situation can be visualized for both model switches in the Figures 9.4 and 9.5.

On the other hand, it was expected that the MAPE would decrease with the increase of the clusters number, since each controller was designed for a smaller neighborhood, which could positively influ-

ence the performance. However, this situation does not happen at all, being the MAPE approximately equal or slightly greater for simulations with 12 clusters, probably due to the oscillations previously described.

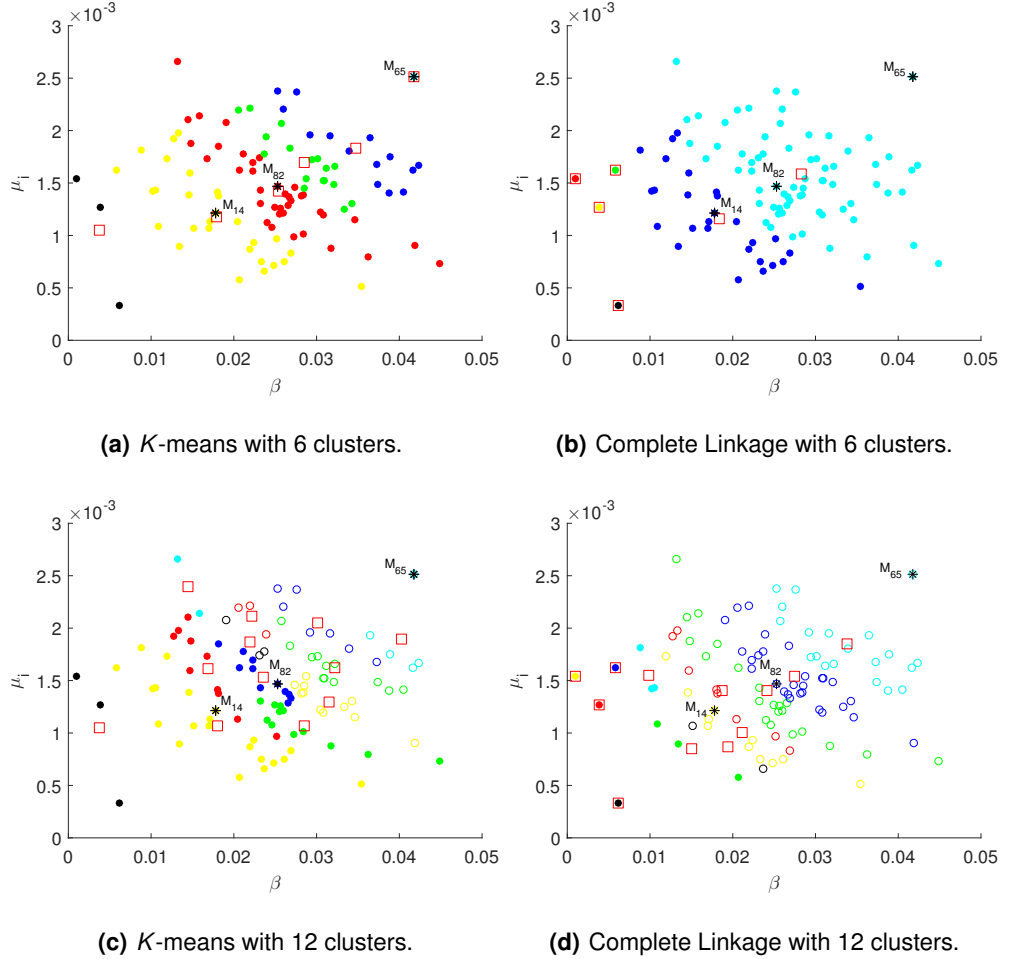


Figure 9.1: Partition of the model data set according to the four methods – Test A.

From the algorithms with 6 clusters, the k -means presents a slightly lower MAPE. However, what really sets them apart is the number of true and false switches and the associated time delay. The complete linkage with 6 clusters does not have false switches, presenting a rate of 2/2 true switches, and an average delay of 30.7 *days*. This case occurs because the models M_{82} and M_{65} belong to the same cluster – Figure 9.1(b) – which means that the system only has to react to one model switch. On the other hand, the k -means with 6 clusters has a rate of 3/3 true switches and 2 false switches with an average delay of 59.8 *days*. However, both false switches occur "halfway" through the true switch – Figure 9.2. This situation happens because the model M_{82} in the Figure 9.1(a) belongs to cluster c_3 and the model M_{65} to the cluster c_6 , hence the transition through clusters c_4 and c_5 takes place as a "bridge" to achieve the cluster destination c_6 .

Since the simulations for the complete linkage are not conclusive in this test, the k -means with 6 clusters was considered to be the method with the most satisfactory results, being used in the following subsections.

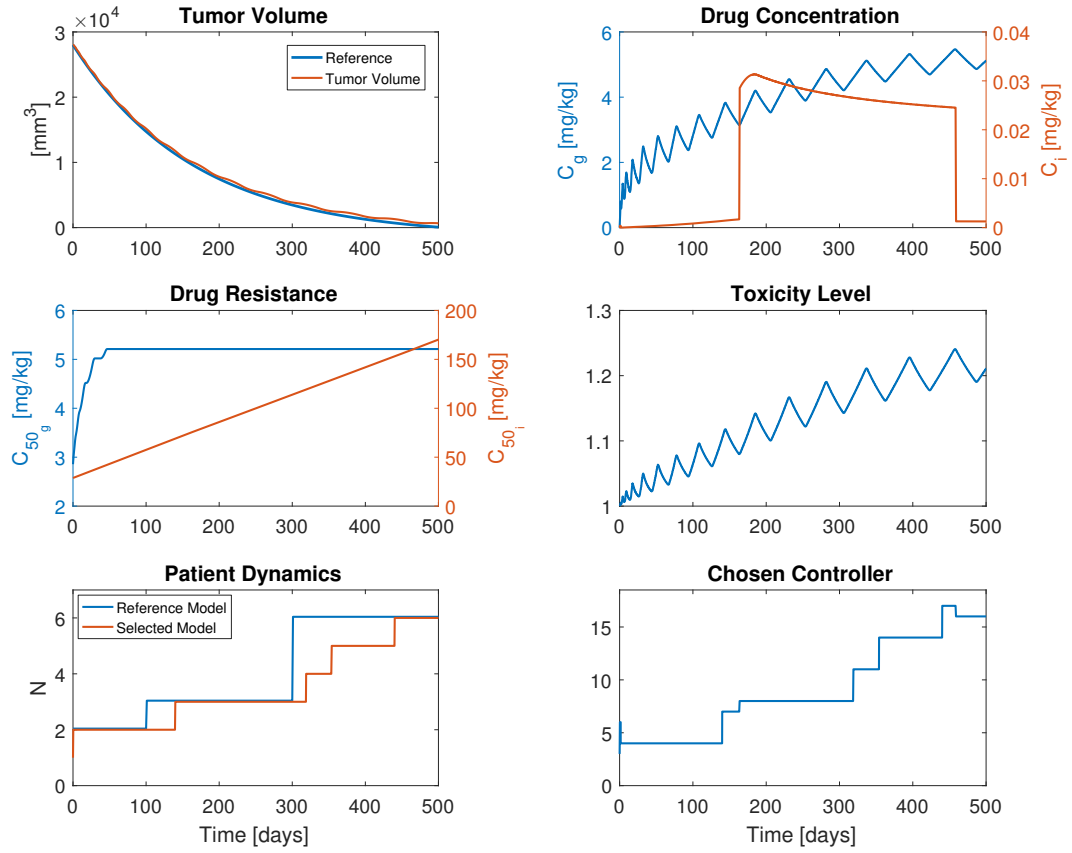


Figure 9.2: Simulation of the MMAC algorithm using the k -means with 6 clusters – Test A.

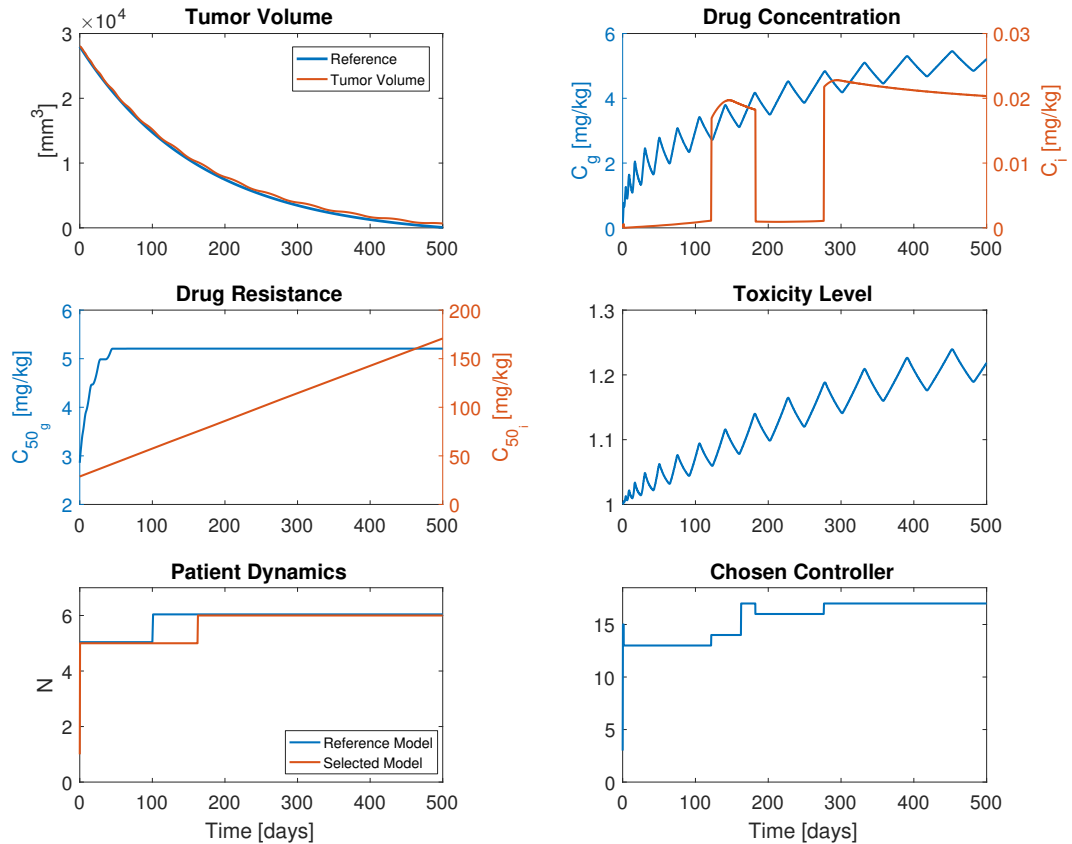


Figure 9.3: Simulation of the MMAC algorithm using the complete linkage with 6 clusters – Test A.

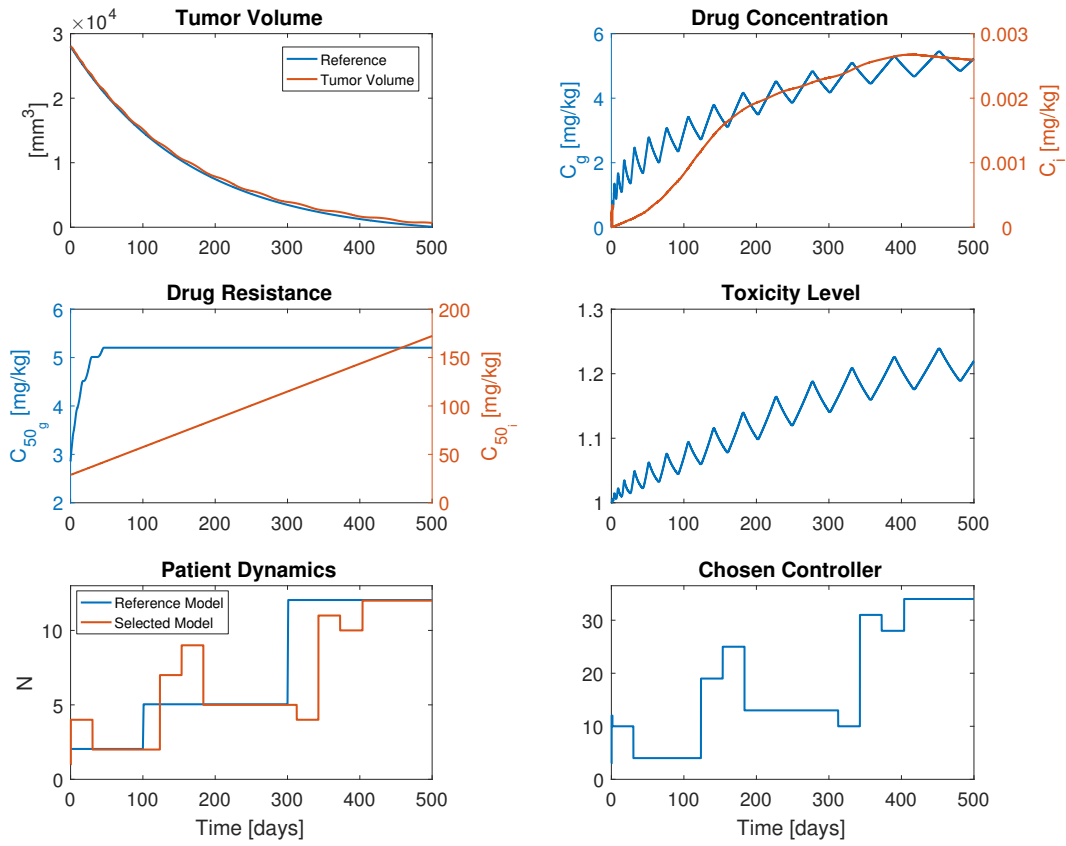


Figure 9.4: Simulation of the MMAC algorithm using the k -means with 12 clusters – Test A.

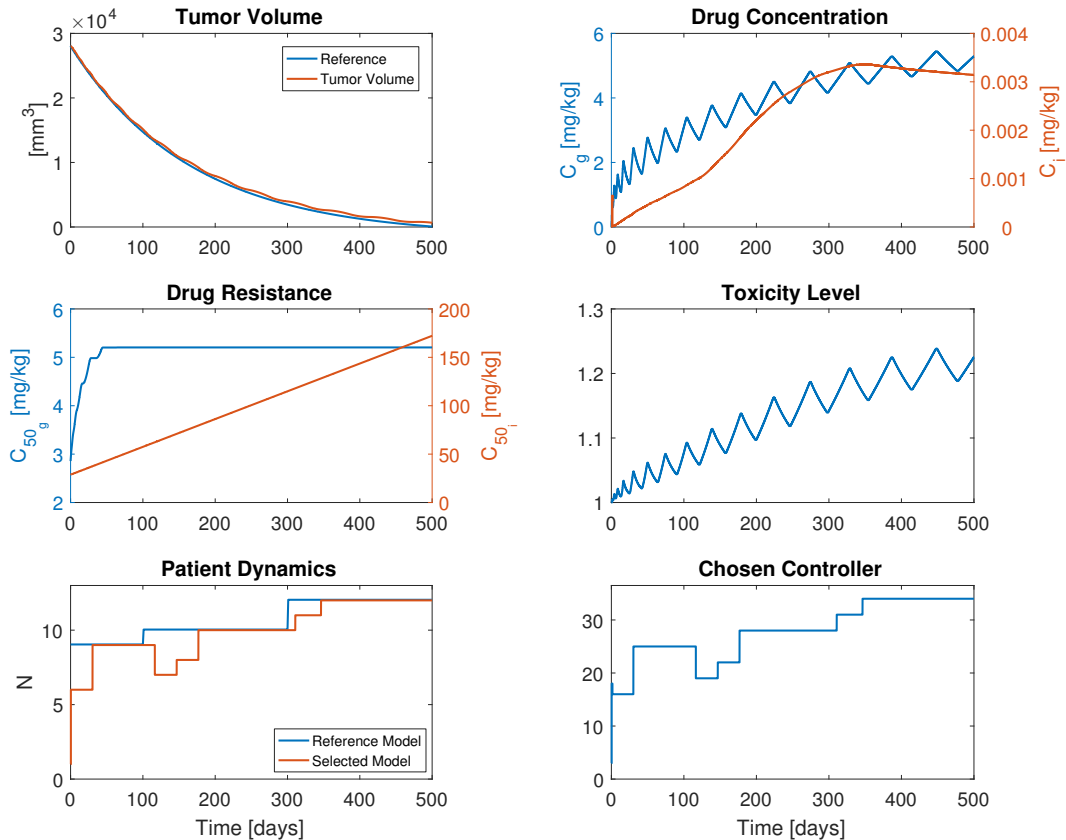


Figure 9.5: Simulation of the MMAC algorithm using the complete linkage with 12 clusters – Test A.

The abrupt changes in the concentration for the simulations with 6 clusters should be noted, in the Figure 9.2, at $t = 160$ and 460 days, and in the Figure 9.3, at $t = 115, 185$ and 275 days. These changes result from the variations in the controllers that were designed for the same model and that are performed directly in the Pharmacodynamical Simulation system – Section 5.2 – that is minimizing the toxicity levels. As an example, in the Figure 9.2, at $t = 160$ days, by performing the change from the controller 7 to 8, the LQR controller designed with the matrix R_1 is replaced by the one with the matrix R_2 – subsection 5.1.2 – which keeps the bevacizumab concentration but increases the atezolizumab input.

9.1.1 Bolus Computation

From the computed concentrations $C_g(t)$, for anti-angiogenesis, and $C_i(t)$, for immunotherapy, a bolus therapy can be calculated through the algorithm described in the Chapter 8. For both therapy concentrations, bolus were calculated for periodicities of 7, 21, and 42 days. The MAPE between the desired and obtained mean concentrations, and the maximum bolus dose administrated were the two factors chosen for the evaluation of the bolus therapy – Table 9.1.

Table 9.1: Evaluation metrics for the designed bolus therapies – Test A.

Periodicity [days]	$C_g(t)$			$C_i(t)$		
	7	21	42	7	21	42
MAPE [%]	10.14	7.93	16.42	157.18	163.58	165.37
Max Bolus [mg/kg]	15	15	15	0.08	0.09	0.11

As expected, with the exception of the therapy $C_g(t)$ for $d_g = 21$ days, the MAPE increases with the increase of the periodicity. This situation happens because with smaller periodicities one can get more accurate results. The values of MAPE for $C_i(t)$ are very large due to the abrupt changes that happen twice over the therapy duration, being the immunotherapy modulated by a bolus therapy with a large following error. However, it is the more feasible result considering the PK restrictions.

Aside from that, the maximum bolus dose is always the maximum dose allowed for $C_g(t)$, and for $C_i(t)$ is higher for larger values of d_i . For those reasons, the selected bolus therapy was a combination between bevacizumab with $d_g = 21$ days and atezolizumab with $d_i = 7$ days, whose simulations are illustrated in Figure 9.6.

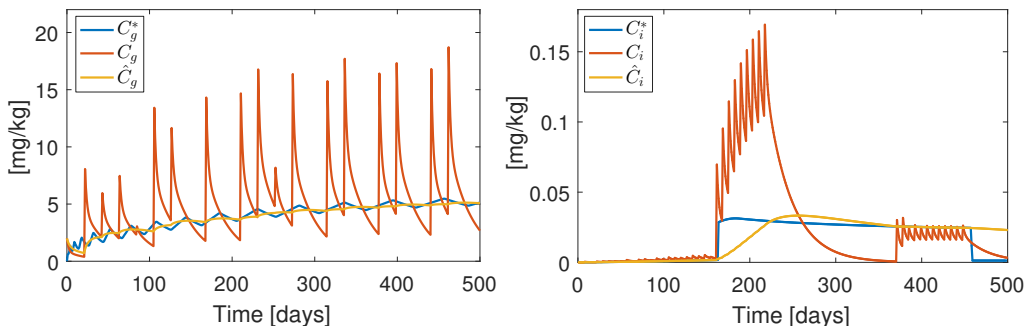


Figure 9.6: Designed bolus therapy for $C_g(t)$ with $d_g = 21$ days and $C_i(t)$ with $d_i = 7$ days – Test A.

9.1.2 Dwell Time Variation

To study the influence of the dwell time τ_D in the control system, simulations were performed for the values $\tau_D = 0$, and $\tau_D = 75 \text{ days}$ and compared with the default value used in the previous simulations, $\tau_D = 30 \text{ days}$.

The selected models for each simulation are illustrated in Figure 9.7 and their evaluation metrics described in Table 9.2.

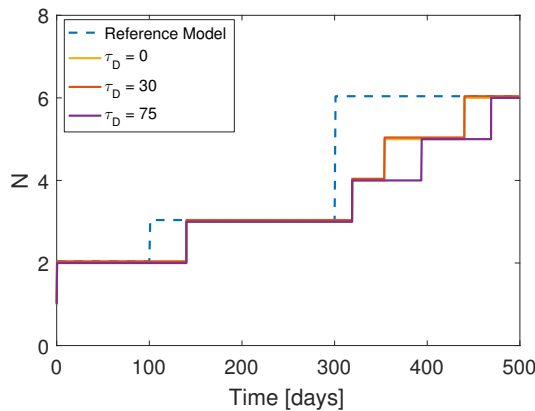


Figure 9.7: Selected patient dynamics depending on the value of the dwell time τ_D – Test A.

As it is possible to see, the curves of $\tau_D = 0$ and $\tau_D = 30 \text{ days}$ are exactly the same, having also the same metrics. This situation means that the used dwell time in the simulation from Figure 9.2 is not influencing the way the system reacts. That is, the obtained delays are exactly the time needed for system to stabilize.

For the simulation with $\tau_D = 75 \text{ days}$, the case is different, since an additional time is required before switching the model. However, this supplementary delay does not influence the reference following since the MAPE is almost the same for all simulations.

To conclude, the usage of the dwell time for this test has proven to be neither harmful for the control system nor beneficial, since there is no chattering in this simulation.

9.1.3 Pharmacodynamical Simulation Error Variation

In order to study the influence of the uncertainty in the parameters of Pharmacodynamical Simulation, several simulations were performed for different values of $\Delta\theta_{PS}$. The results are illustrated in Figure 9.8 and also quantitatively described in Table 9.2.

A higher value for $\Delta\theta_{PS}$ basically represents an increase in the parameters of the DR' system, belonging to the Pharmacodynamical Simulation, namely in the parameters L'_r , K'_r , and C'_{50base} – Section 5.2. Increasing L'_r means that the drug resistance threshold is higher, but the same variation in the other two parameters is a warning for the control system that the mutant cells are more drug resistant. In this way, the control system is going to react by administrating a higher concentration for both drugs in order to achieve the same desired effect, as it is visible in the Figure 9.8 where the drug concentration is higher for larger values of $\Delta\theta_{PS}$. Consequently, the toxicity maximum levels achieve

values of $T_x = 4$, for $\Delta\theta_{PS} = 150 \%$, and $T_x = 49.6$, for $\Delta\theta_{PS} = 250 \%$, that are graded, respectively, as life-threatening and death – Section 3.4.

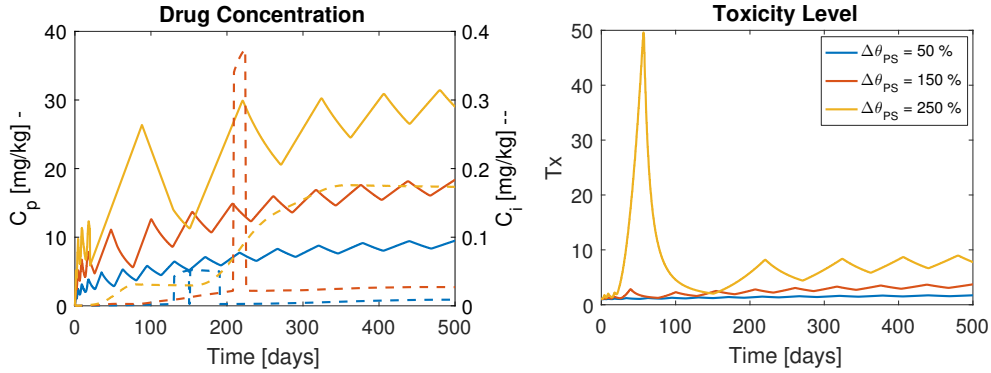


Figure 9.8: Drug concentration and toxicity level of therapies computed for different values of $\Delta\theta_{PS}$ – Test A. The dashed curves in the left plot represent $C_i(t)$ and the solid curves $C_g(t)$.

However, this higher cell resistance is not real, since it is only an error between the Pharmacodynamical Simulation parameters and the real ones from the patient. In this way, some repercussions in the system behavior are expected, more specifically, worse following errors for larger values of $\Delta\theta_{PS}$, which happens for $\Delta\theta_{PS} = 150$ and 250% . However, for $\Delta\theta_{PS} = 50 \%$ the case is distinct, since its computed MAPE is smaller than the one without uncertainty.

This decrease in the MAPE for small values of $\Delta\theta_{PS}$ may be due to the existence of an offset in the system. Having a small positive value of $\Delta\theta_{PS}$ means administrating a slightly higher drug concentration in the patient, which can dissipate the offset and, consequently, improve the reference following. Nevertheless, more tests have to be performed to prove its existence.

9.1.4 Noise and Disturbance Variation

In a real situation, the sensors that measure the tumor volume and the actuators that administrate the drug concentration can have some associated uncertainty. In this work, this discrepancy is going to be simulated by adding disturbance d and noise n , respectively, to the input and output of the system. The system is going to be tested for three different situations: R_1 with $n = 0.1$ and $d = 10^{-4}$, R_2 with $n = 1$ and $d = 10^{-3}$, and R_3 with $n = 10^3$ and $d = 1$. The results are illustrated in Figure 9.9 and described in Table 9.2.

As expected, by increasing the noise and disturbance, the quality of the control system deteriorates. That is verified with the increase in the MAPE and in the number of false switches for the disturbed situations when compared with R_0 (no noise or disturbance).

For the situation R_1 , although the MAPE is slightly higher than in R_0 , its curves for the selected model are very similar. This event indicates that the values of noise and disturbance of the situation R_1 are acceptable for keeping the good performance of the control system.

On the other hand, for the other two disturbed situations, this conclusion cannot be expressed. For the situation R_2 , there is an increase in the MAPE and, in addition, the switch between the models M_{14} and M_{82} is not correctly handled, since only false switches happen during the period where M_{82}

is representing the patient. For the situation R_3 , in addition to the achieved higher MAPE, the MMAC system does not react to any changes, except at the first instants. This is exclusively due to the hysteresis condition. With the addition of noise and disturbance of large amplitude to the system, an "offset" with large varying amplitude is added to all the signals of the filtered prediction error π_i , that had small amplitudes. In this way, a set of signals with high order amplitudes that are closer to each other is created. For this reason, once the first model is selected, it is preserved until the end of the therapy since any possible switch "stagnates" in the hysteresis condition.

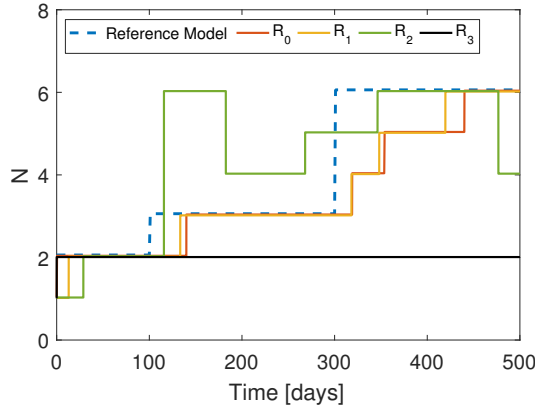


Figure 9.9: Selected patient dynamics for the three different uncertain situations – Test A.

Table 9.2: Evaluation metrics for all the simulations performed in Test A.

Algorithm	N_c	Test	MAPE [%]	True Switch	False Switch	τ_{min} [days]	τ_{mean} [days]	τ_{max} [days]
K-Means	6	-	3.0115	3/3	2	0.4	59.8	140
		$\tau_D = 0$	3.0115	3/3	2	0.4	59.5	139.2
		$\tau_D = 75$	3.0116	3/3	2	0.4	69.4	168
		$\Delta\theta_{PS} = 50\%$	2.9799	3/3	2	0.4	56.6	139
		$\Delta\theta_{PS} = 150\%$	3.1136	3/3	2	0.4	59.57	139.4
		$\Delta\theta_{PS} = 250\%$	5.1612	3/3	2	0.4	59.43	139.4
		$n = 0.1, d = 10^{-4}$	3.0362	3/3	2	13	54.93	118.5
		$n = 1, d = 10^{-3}$	3.0323	2/3	4	28.8	37.05	45.3
		$n = 10^3, d = 1$	25.0911	1/3	0	0.4	0.4	0.4
	12	-	3.0203	3/3	5	30.4	71.93	102.8
Complete Linkage	6	-	3.0206	2/2	0	0.4	30.7	61
	12	-	3.0205	3/3	3	30.3	50.5	75.8

9.2 Test B – Model Linear Time Varying

The test considered in this section simulates a patient dynamics with the same changes over time as the Test A, but instead of an instantaneous switch between two models, the models are time varying. In this way, the parameters β and μ_I vary approximately linearly over time, as it is represented in Figure 9.10 by the solid black line. Between 0 and 100 days, a variation from the model M_{14} to the M_{82} is performed, followed by another variation of 200 days until the model M_{65} . In the last 100 days of the simulation, this last model is kept. The simulations obtained for each of the four algorithms are illustrated in Figures 9.11, 9.12, 9.13, and 9.14 and the evaluation metrics are described in Table 9.4.

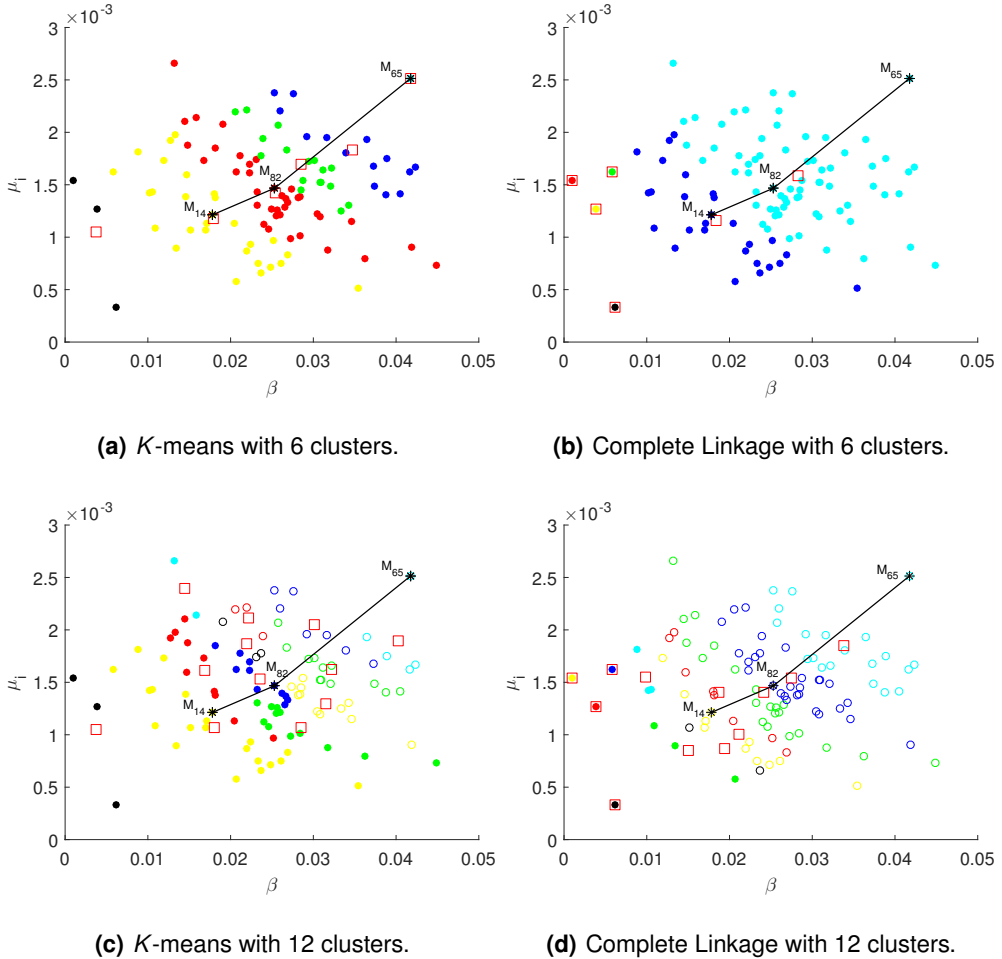


Figure 9.10: Partition of the model data set according to the four methods – Test B.

As in Test A, all the four simulations are satisfactory with MAPE around 3 % and low toxicity levels. Comparing the algorithm with 6 and 12 clusters, the same conclusions can be drawn: larger variations in the selected dynamics of the 12 clusters' algorithms, particularly in the k -means that has 8 false switches and a rate of 2/8 true switches. However, if a more detailed analysis is conducted, from Figure 9.13, one can see that 6 in 8 false switches are delayed true switches, *i.e.*, the right switches are performed but not in the correct time due to their delay. This situation indicates that the variations occur too fast, and since the system as to dwell 30 *days* after a switch, the performance is deteriorated. In the complete linkage with 12 clusters, the variations are not so fast, leading to only 1 false switch and a rate of 5/6 true switches, which is an improvement in the performance regarding Test A. The MAPE for the 12 clusters' algorithms are closer from values of Test A and are slightly higher comparing with the 6 clusters' algorithms, possibly for the same reasons expressed in the previous section.

A performance improvement was obtained for both of the 6 clusters' algorithms, regarding the same simulations in Test A. The MAPE levels for the k -means and complete linkage are somewhat smaller for this last test, as well as the time delay, whose means for both methods are significantly lower than the ones from Table 9.2.

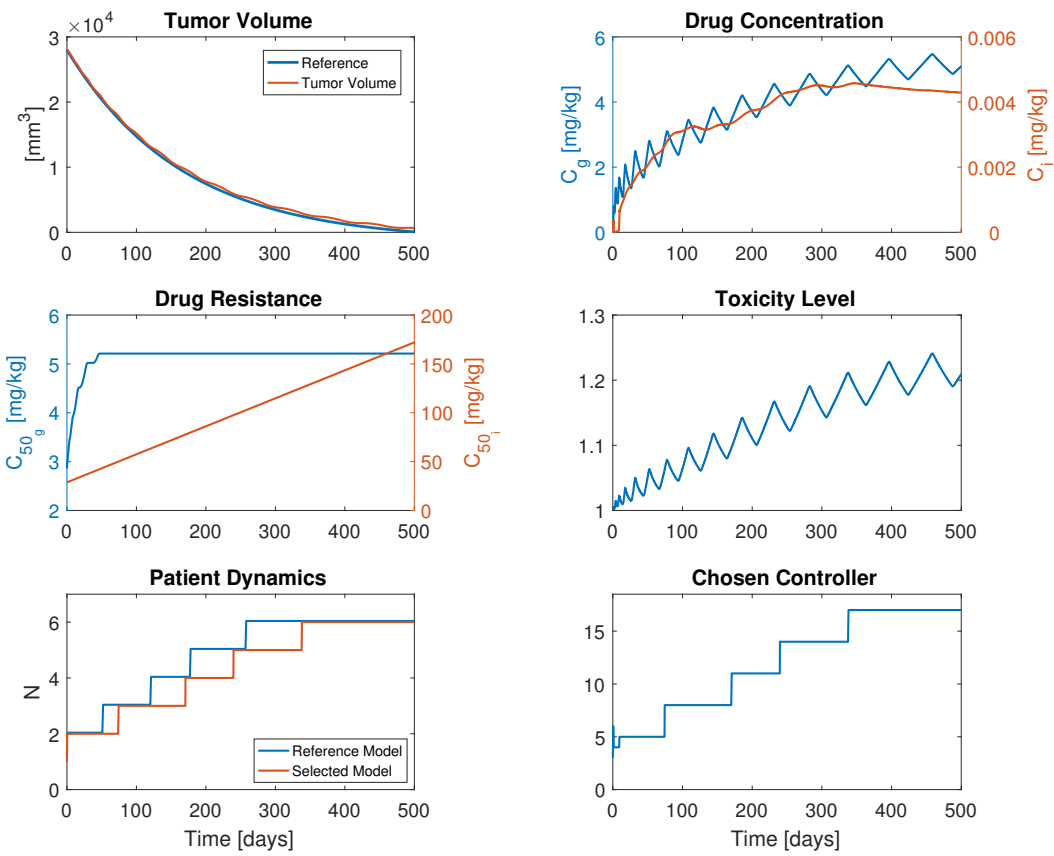


Figure 9.11: Simulation of the MMAC algorithm using the k -means with 6 clusters – Test B.

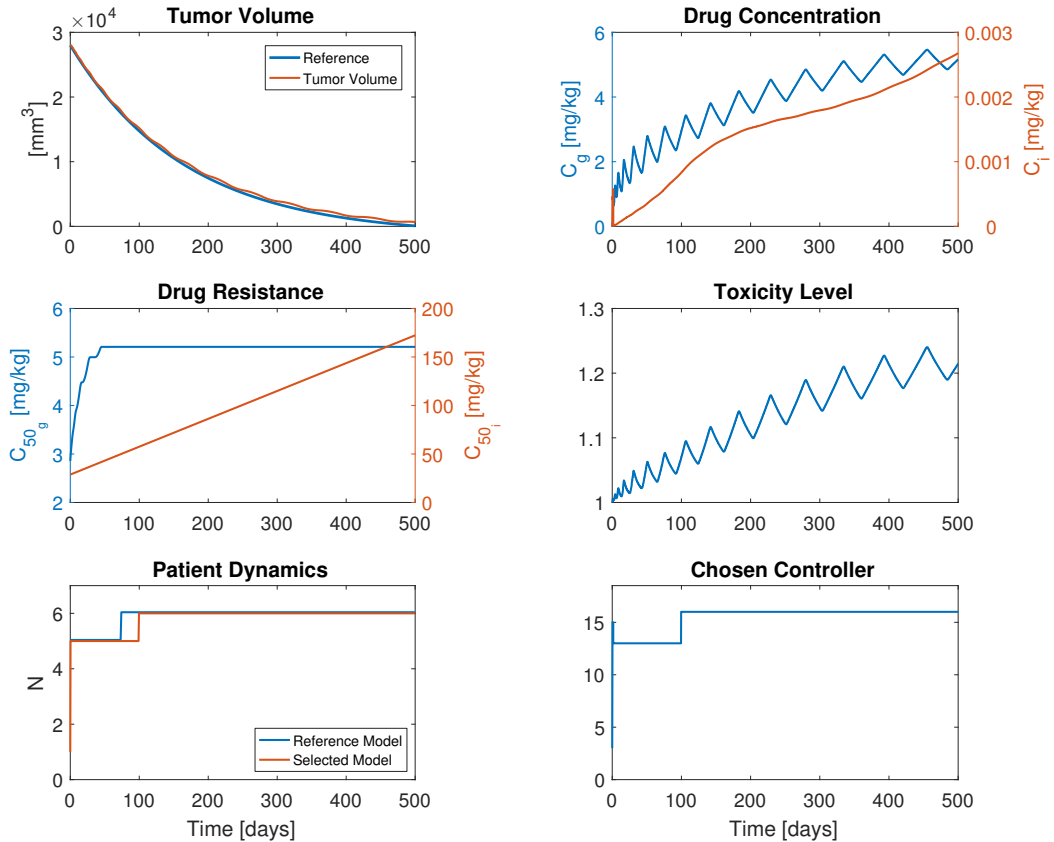


Figure 9.12: Simulation of the MMAC algorithm using the complete linkage with 6 clusters – Test B.

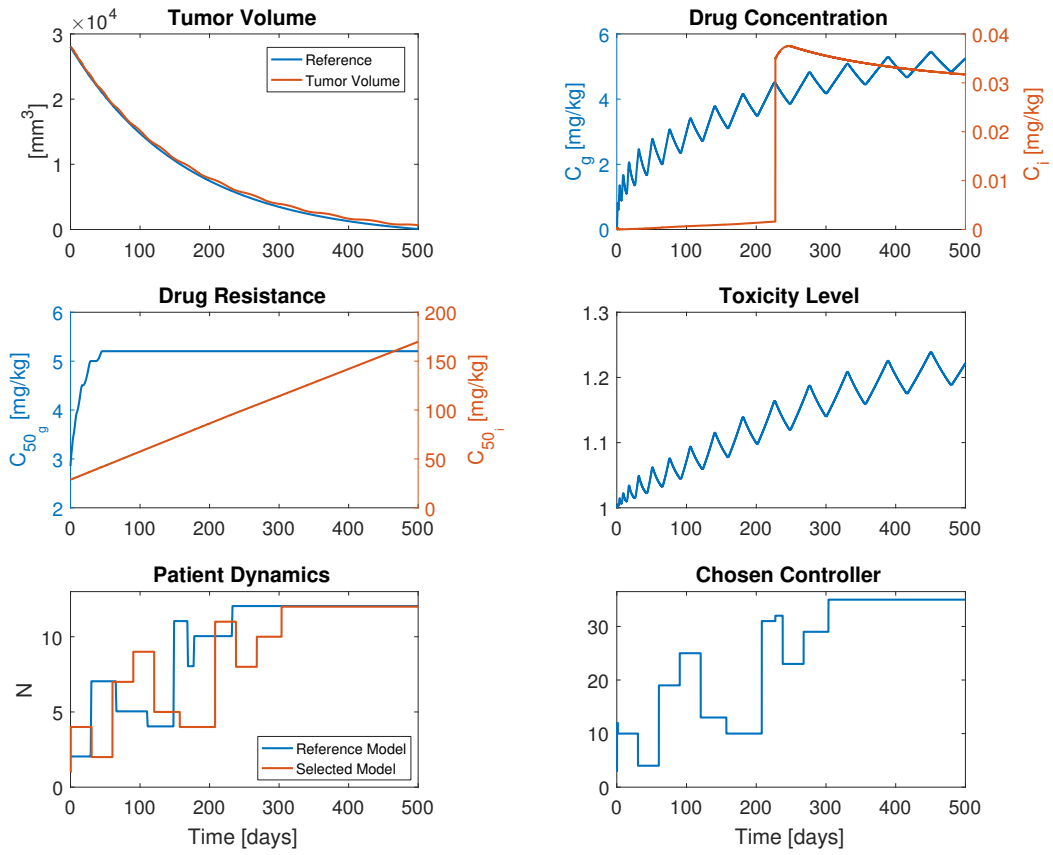


Figure 9.13: Simulation of the MMAC algorithm using the k -means with 12 clusters – Test B.

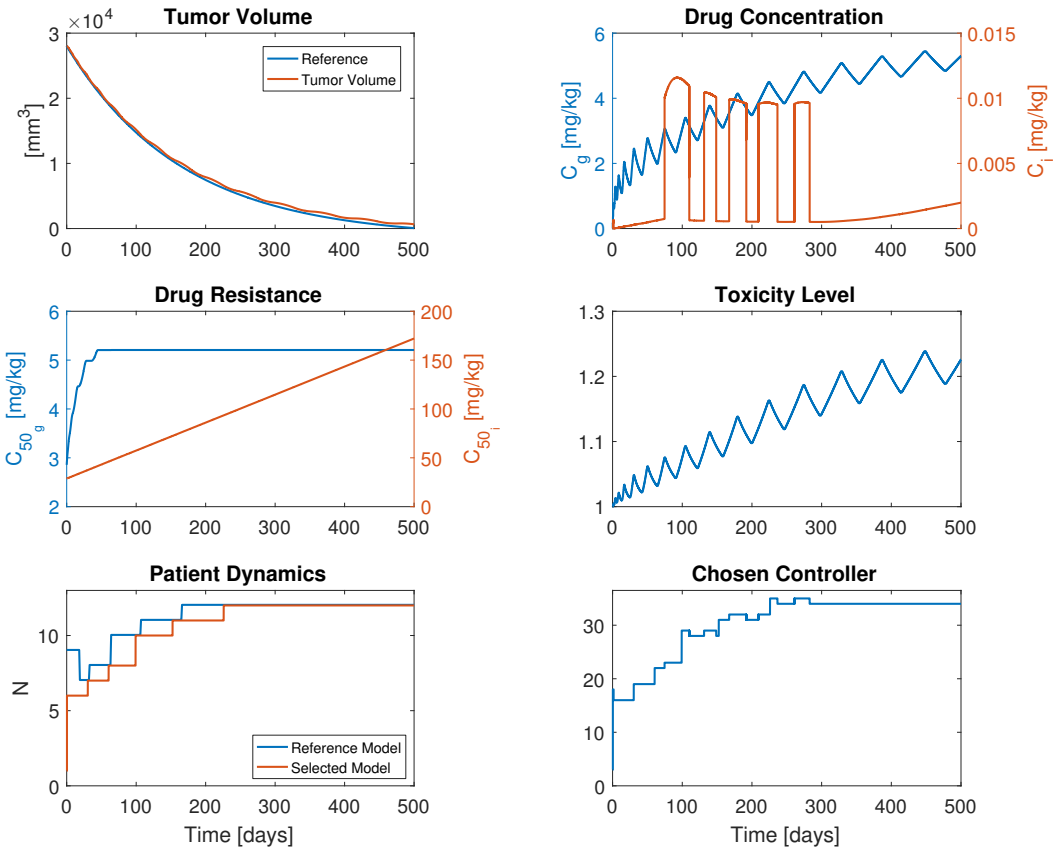


Figure 9.14: Simulation of the MMAC algorithm using the complete linkage with 12 clusters – Test B.

Aside from that, both algorithms have full accuracy, with no false switches and 5/5 or 2/2 rates of true switches, respectively, for k -means and complete linkage.

For the same reasons expressed in the last section, the k -means with 6 clusters was chosen to be the method with the most satisfactory results, being used in the following tests.

9.2.1 Bolus Computation

For the considered drug concentrations, the MAPE between the desired and obtained mean concentration and the maximum bolus dose administrated are described in the Table 9.3.

Table 9.3: Evaluation metrics for the designed bolus therapies – Test B.

	$C_g(t)$			$C_i(t)$		
Periodicity [days]	7	21	42	7	21	42
MAPE [%]	10.3	7.99	16.43	4.41	13.7	19.84
Max Bolus [mg/kg]	15	15	15	0.0067	0.018	0.022

As expected, and as in the Test A, for small periodicities one gets more accurate results, with lower MAPE, having also the same exception for $d_g = 21$ days. The maximum bolus dose follows the same behavior as in the last section, being the maximum dose allowed for $C_g(t)$ and growing with the increase of the periodicity. In this way, a therapy of bevacizumab with $d_g = 21$ days and atezolizumab with $d_i = 7$ days was chosen, as illustrated in Figure 9.15.

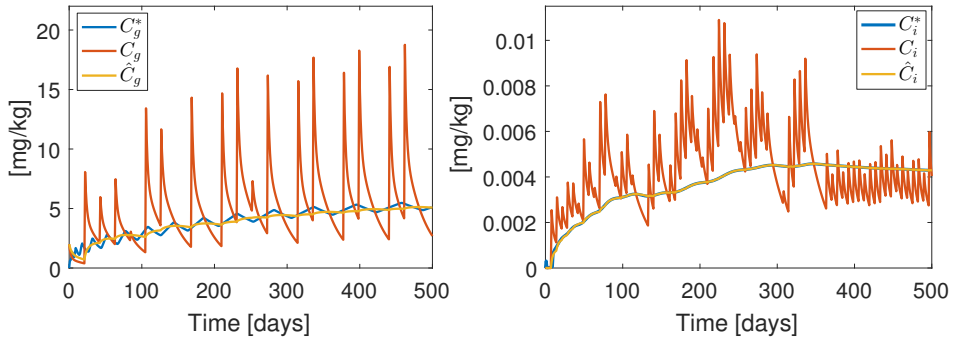


Figure 9.15: Designed bolus therapy for $C_g(t)$ with $d_g = 21$ days and $C_i(t)$ with $d_i = 7$ days.

It is noticeable that, in this test, unlike the previous one, the MAPE values for $C_i(t)$ are not so large since there are no abrupt changes in the concentration.

9.2.2 Dwell Time Variation

The simulations performed for the three different values of dwell time τ_D are illustrated in Figure 9.16 and its evaluation metrics in Table 9.4.

The obtained results allow to draw the same conclusions as the ones taken in Test A. That is, since both curves for $\tau_D = 0$ and 30 days are equal, their delays are exactly the time needed for the system to stabilize. In this case, only a minor difference around $t = 250$ days is obtained for the curve for $\tau_D = 75$ days, which also almost does not influence the following error, since the MAPE values are identical. In this way, more tests are needed to prove the influence of the dwell time.

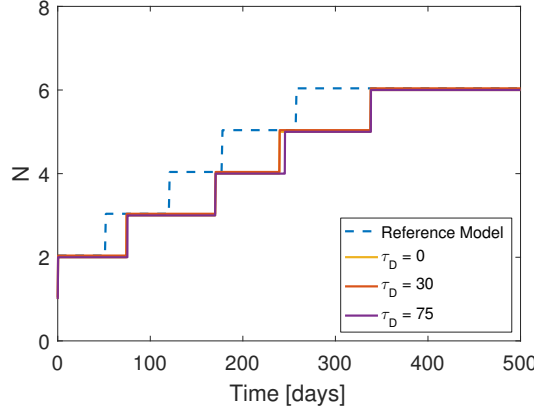


Figure 9.16: Selected patient dynamics depending on the value of the dwell time τ_D – Test B.

9.2.3 Pharmacodynamical Simulation Error Variation

The simulations performed in this test for different values of $\Delta\theta_{PS}$ – Figure 9.17 and Table 9.4 – show the same conclusions previously drawn for Test A. The drug concentrations increase for higher value of $\Delta\theta_{PS}$, as well as the toxicity levels, that follow the same behavior achieving values of $T_x = 3.7$ (life-threatening) for $\Delta\theta_{PS} = 150\%$ and $T_x = 49.9$ (death) for $\Delta\theta_{PS} = 250\%$.

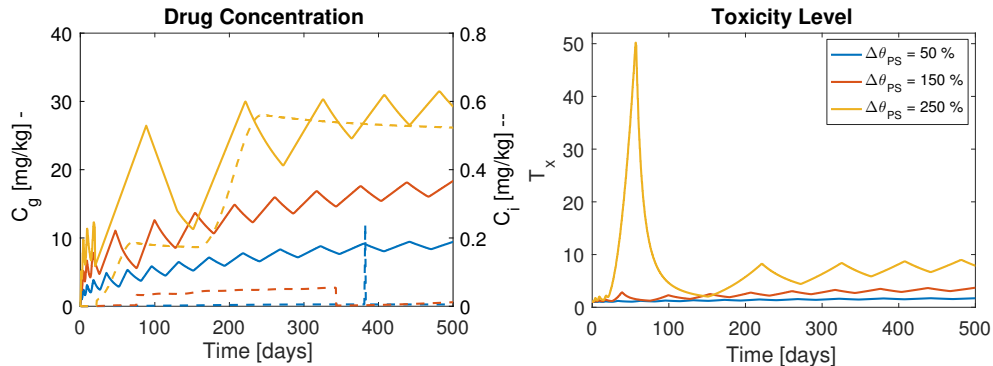


Figure 9.17: Drug concentration and toxicity level of therapies computed for different values of $\Delta\theta_{PS}$ – Test B. The dashed curves in the left plot represent $C_i(t)$ and the solid curves $C_g(t)$.

The same repercussions as in Test A were found, with an increase in the MAPE for larger values of $\Delta\theta_{PS}$, with the exception of $\Delta\theta_{PS} = 50\%$ with a decrease of 1.15 % in the following error. This situation indicates, once more, the possible existence of a small offset in the system, that is being dissipated by this small increase in the drug concentration.

9.2.4 Noise and Disturbance Variation

The simulations computed for the three different situations R_1 , R_2 , and R_3 are represented in Figure 9.18 and its evaluation metrics in Table 9.4.

The theory from Test A is proved, having higher MAPE, more false switches, and fewer true switches for situations with more noise and disturbance.

Contrary to the last section, there are no equivalence between the curves of the selected model for R_0 and R_1 . Aside from that, in the last test the number of true and false switches are the same

for R_0 and R_1 , which does not happen in this case, since R_0 has a rate of 5/5 true switches and 0 false switches, and R_1 a rate of 3/5 true switches and 5 false switches. This control system degradation indicates that the model time varying test is more sensitive in terms of noise and disturbance comparing with the model switch test.

For the situation R_3 , the MMAC system also does not react to any changes, except at the first instants, keeping the model M_2 during practically all the therapy period. This case happens again due to the situation of switch "stagnation" in the hysteresis condition.

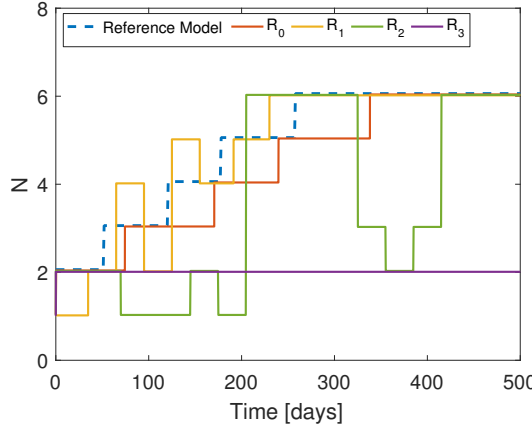


Figure 9.18: Selected patient dynamics for the three different uncertain situations – Test B.

Table 9.4: Evaluation metrics for all the simulations performed in Test B.

Algorithm	N_c	Test	MAPE [%]	True Switch	False Switch	τ_{min} [days]	τ_{mean} [days]	τ_{max} [days]
K-Means	6	-	3.0113	5/5	0	0.4	42.75	80.2
		$\tau_D = 0$	3.0113	5/5	0	0.4	42.47	80.2
		$\tau_D = 75$	3.0119	5/5	0	0.4	44.24	80.3
		$\Delta\theta_{PS} = 50\%$	2.9767	5/5	0	0.4	42.85	80.2
		$\Delta\theta_{PS} = 150\%$	3.1112	5/5	0	0.4	42.83	80.4
		$\Delta\theta_{PS} = 250\%$	5.1847	5/5	0	0.4	43.44	81.4
		$n = 0.1, d = 10^{-4}$	3.0336	3/5	5	13.4	27.22	35
		$n = 1, d = 10^{-3}$	3.0481	2/5	7	0.4	78.8	157.2
		$n = 10^3, d = 1$	16.4417	1/5	0	0.4	0.4	0.4
	12	-	3.0220	2/8	8	30.4	50.45	70.5
Complete Linkage	6	-	3.0178	2/2	0	0.4	12.9	25.4
Complete Linkage	12	-	3.0231	5/6	1	11.4	35.4	59

9.3 Test C – Model Non-Linear Time Varying

This last test is executed for a non-linear time variation of the model parameters, being the "true" models completely different from Test A and B, as well as, the chosen trajectory in the parameter space.

This variation, represented in the Figure 9.19, occurs in the following way: it takes 100 days from the model M_A to M_B , 50 days from the model M_B to M_C , and finally 350 days from M_C to M_D .

The simulations performed for the four methods are represented in Figures 9.20, 9.21, 9.22, and 9.23 and its evaluation metrics are described in Table 9.6.

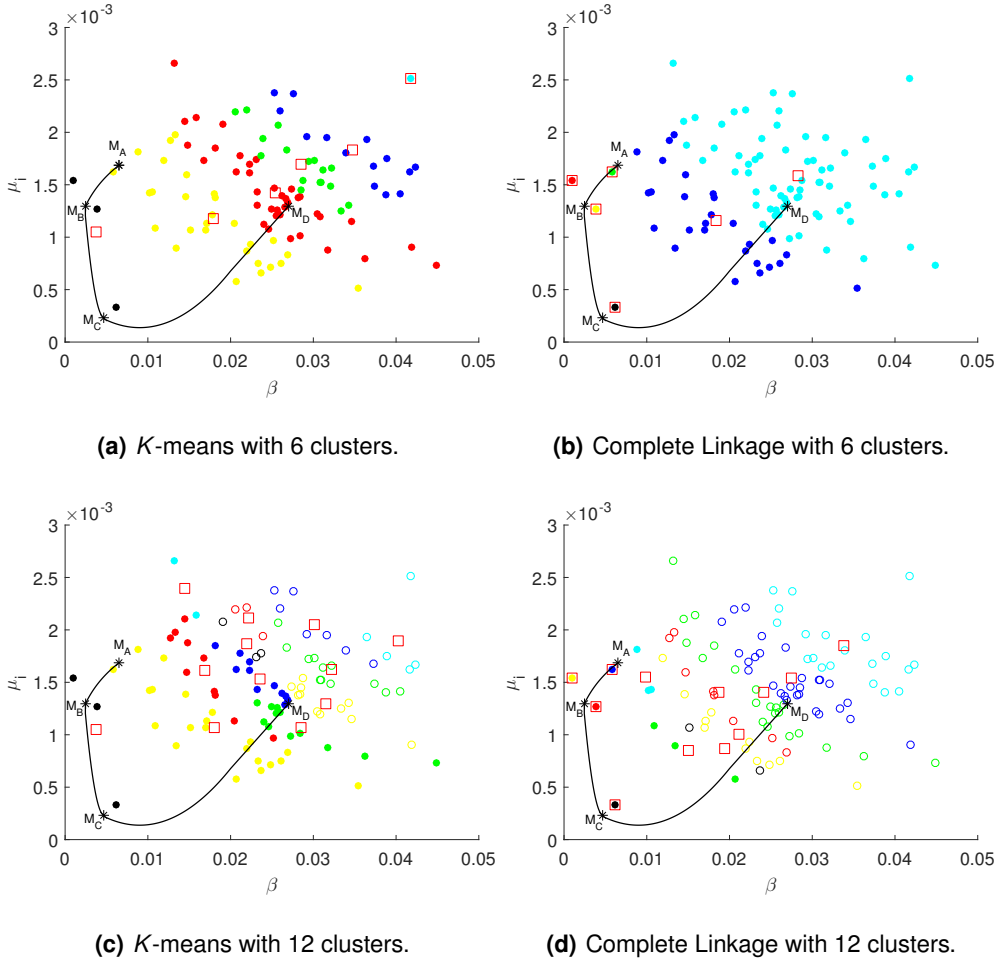


Figure 9.19: Partition of the model data set according to the four methods – Test C.

Although the parameter trajectory, illustrated as a solid black curve in Figure 9.19 – happens in sparse area in terms of models, all the simulations are satisfactory with values of MAPE around 3 % and low toxicity levels, as occurred in the previous sections.

The biggest difference is the non-existence of a full accuracy rate of true switches for the complete linkage with 6 clusters, having also false switches that are not a "bridge" to the cluster destination, as happened in the Test A. Those switch errors deteriorate the performance, causing the MAPE to be closer to the values of the 12 clusters' algorithms, which continue to have poor rates of true switches and a large number false switches.

The situation described in Test B also happened in this test for the 12 clusters' algorithms, being most of the false switches delayed true switches, since the changes in the patient dynamics are too fast to the system to stabilize.

The *k*-means algorithm with 6 clusters was, once more, the method that showed the best results, with 100 % accuracy of true switches, 0 false switches and the lowest MAPE. For these reasons, this method is used in the following subsections.

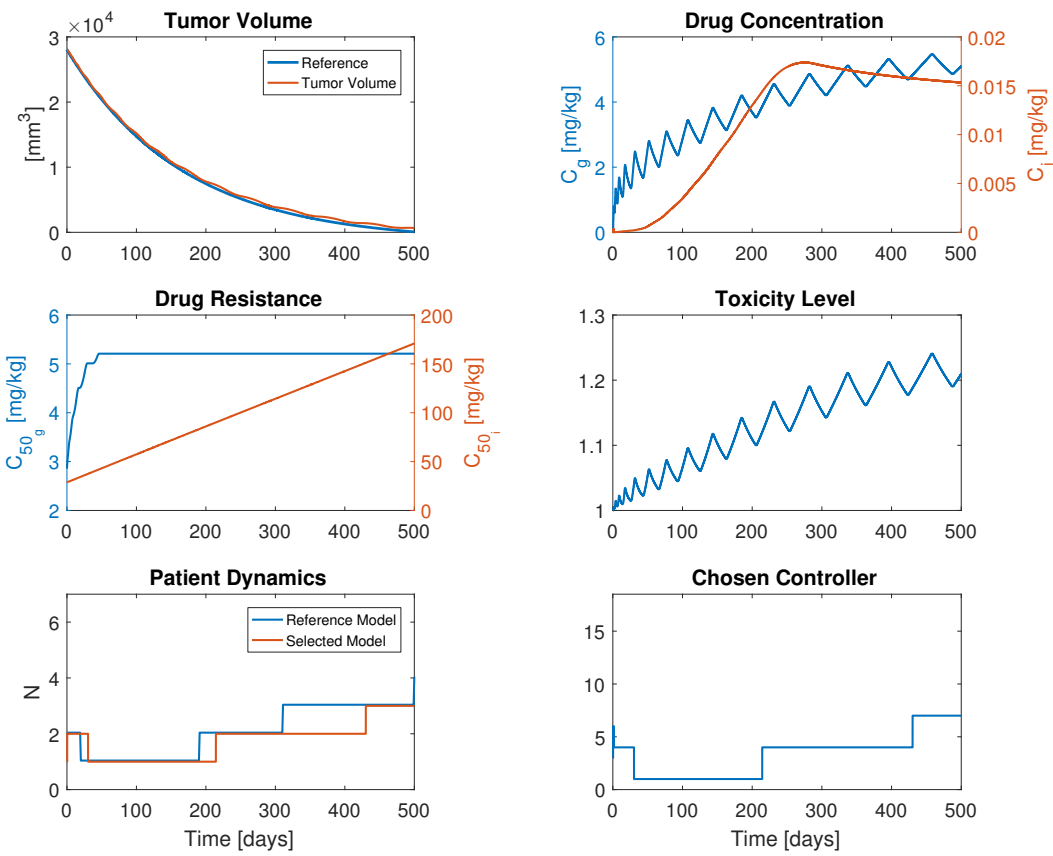


Figure 9.20: Simulation of the MMAC algorithm using the k -means with 6 clusters – Test C.

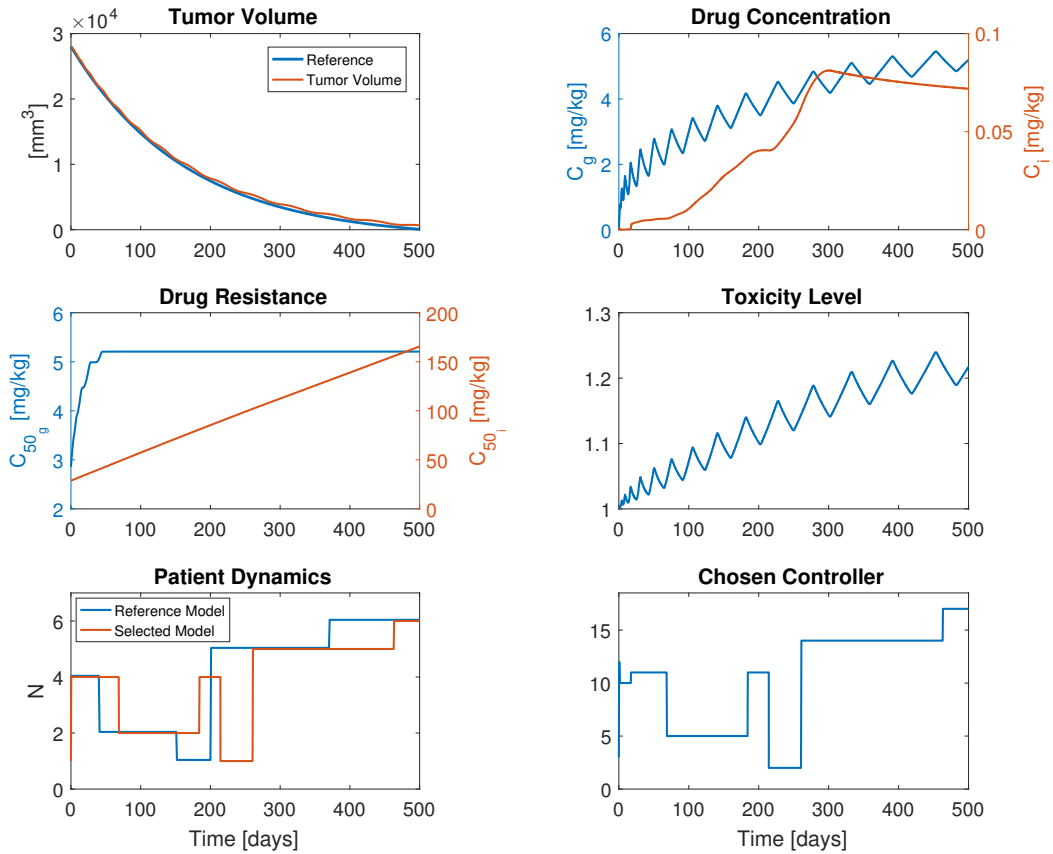


Figure 9.21: Simulation of the MMAC algorithm using the complete linkage with 6 clusters – Test C.

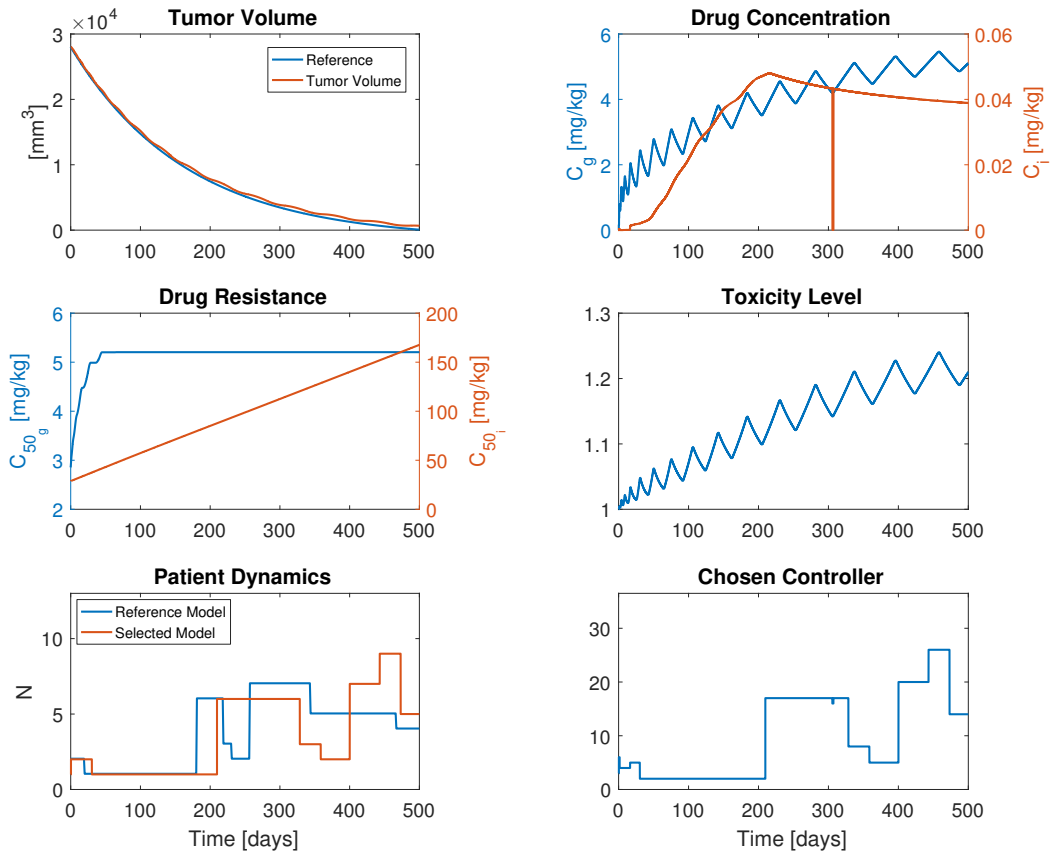


Figure 9.22: Simulation of the MMAC algorithm using the k -means with 12 clusters – Test C.

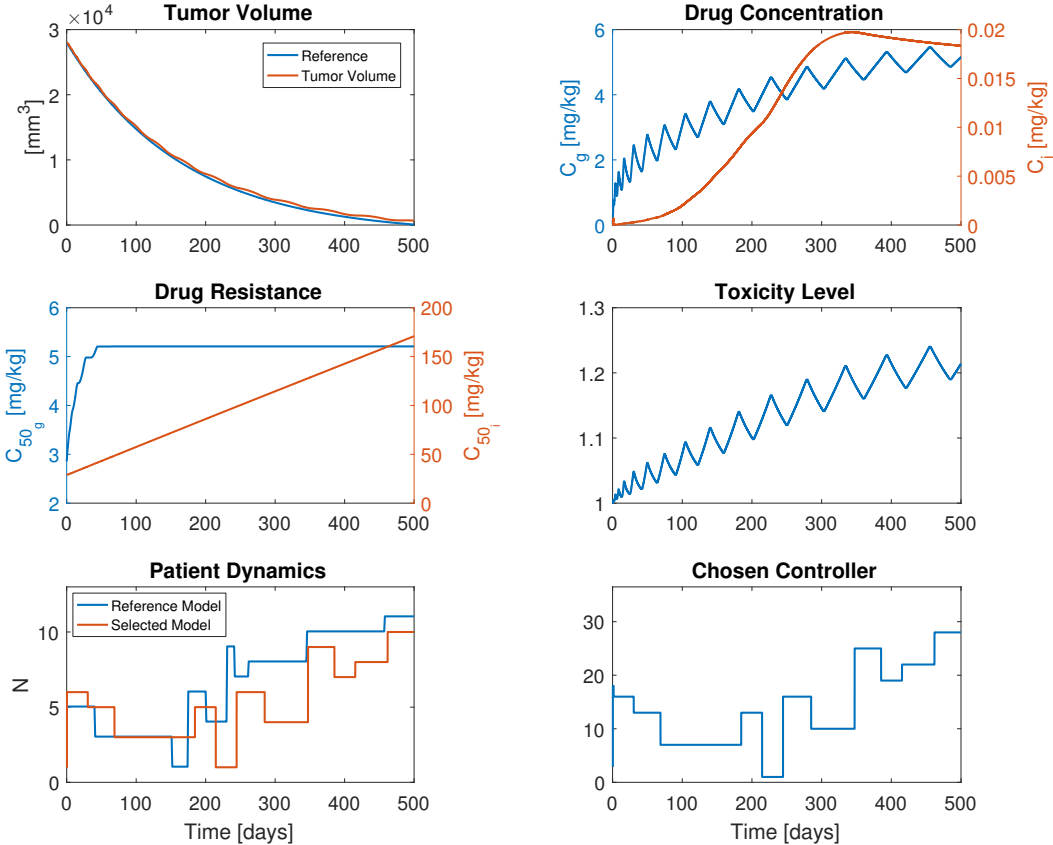


Figure 9.23: Simulation of the MMAC algorithm using the complete linkage with 12 clusters – Test C.

9.3.1 Bolus Computation

As before, a bolus therapy was computed for distinct values of the periodicity, being the results shown in Table 9.5.

Table 9.5: Evaluation metrics for the designed bolus therapies – Test C.

Periodicity [days]	$C_g(t)$			$C_i(t)$		
	7	21	42	7	21	42
MAPE [%]	10.06	7.23	16.39	3.56	6.54	13.55
Max Bolus [mg/kg]	15	15	15	0.0227	0.063	0.0993

Once more, the same conclusions can be drawn: an increase in the MAPE for larger values of the periodicity, except in $C_g(t)$ for $d_g = 21$ days. Aside from that, the maximum bolus dose is always maximum for $C_g(t)$ and increases with the growth in the periodicity.

For those reasons, a combined therapy of $C_g(t)$ with $d_g = 21$ days and $C_i(t)$ with $d_i = 7$ days was selected as the one with the best performance, as happened in the two previous tests.

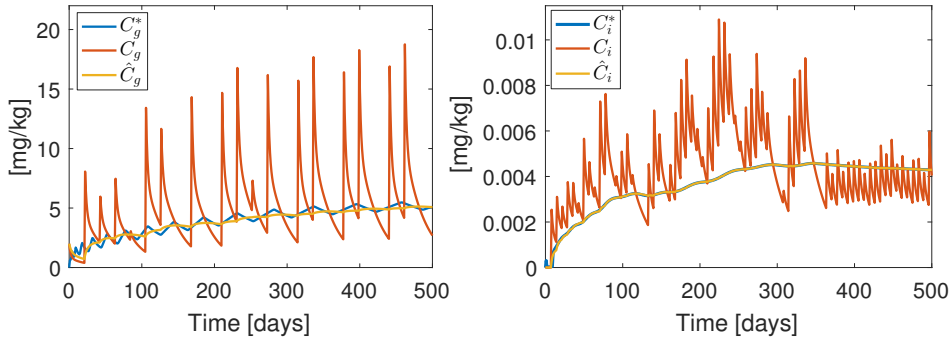


Figure 9.24: Designed bolus therapy for $C_g(t)$ with $d_g = 21$ days and $C_i(t)$ with $d_i = 7$ days – Test C.

9.3.2 Dwell Time Variation

The simulations performed for a varying dwell time τ_D are illustrated in Figure 9.25, as well as described in Table 9.6.

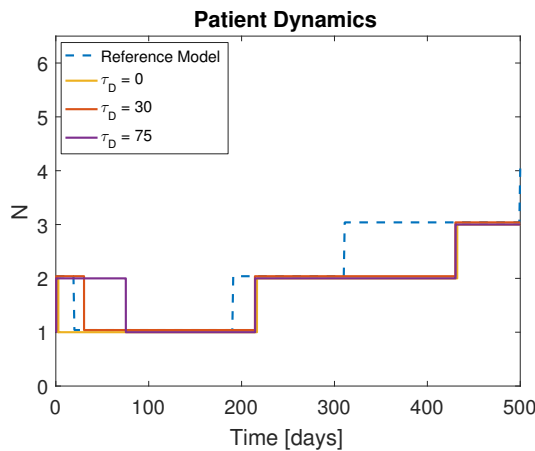


Figure 9.25: Selected patient dynamics depending on the value of the dwell time τ_D – Test C.

Contrary to what happened in the last two sections, in this test the effect of the dwell time can be

observed. All the three different curves are identical for $t \geq 75$ days, but different at the beginning of therapy. For $\tau_D = 30$ and 75 days, there is a switch from the model M_1^c to M_2^c , which is kept during their respective dwell times. However, for the case where $\tau_D = 0$ days, i.e. where no dwell time system is involved, there is a bump at $t = 0.4$ days, since after the last switch, the system returns to the initial model.

This was exactly what was intended to prevent with the dwell time method, since this bumps can strongly deteriorate the control system stability. Furthermore, the current situation represents a set of cases in which the initial switch is not an error, since the reference model is exactly M_2 . Therefore, dwelling in the model M_2 for τ_D contributes positively to the performance. This fact can be evidenced if the MAPE values for the three dwell time tests are compared. Without the dwell time method, i.e. for $\tau_D = 0$ days, the system presents the largest MAPE, since the model M_2^c was not kept during the first instants. The smallest MAPE was obtained for $\tau_D = 30$ days, having thus the best performance.

9.3.3 Pharmacodynamical Simulation Error Variation

The results obtained for the three different simulations are described in the Table 9.6 and illustrated in Figure 9.26.

As in the previous sections, the drug concentrations increase with the grow of $\Delta\theta_{PS}$ and the toxicity level follows the same behavior, achieving values of $T_x = 4.5$ (life-threatening), for $\Delta\theta_{PS} = 150\%$, and $T_x = 51.1$ (death), for $\Delta\theta_{PS} = 250\%$.

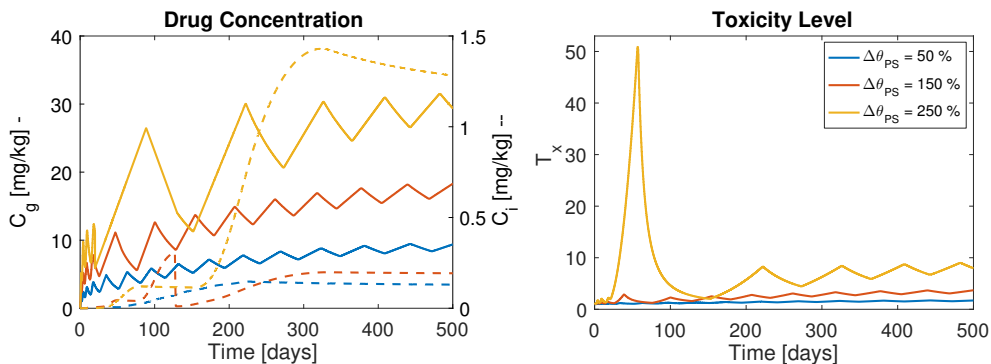


Figure 9.26: Drug concentration and toxicity level of therapies computed for different values of $\Delta\theta_{PS}$ – Test C. The dashed curves in the left plot represent $C_i(t)$ and the solid curves $C_g(t)$.

Regarding the MAPE levels, the same exception was found for $\Delta\theta_{PS} = 50\%$, being its error lower than in the test without uncertainty in the Pharmacodynamical Simulation parameters. In this way, the theory of the existence of an offset in the system is, once more, maintained.

9.3.4 Noise and Disturbance Variation

The results obtained for the three different situation R_1 , R_2 , and R_3 are described in Table 9.6 and illustrated in Figure 9.27.

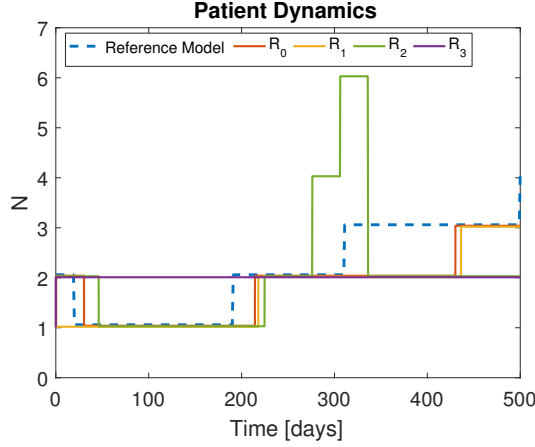


Figure 9.27: Selected patient dynamics for the three different uncertain situations – Test C.

The outcomes are similar to those of the last sections: the system deteriorates with the increase of noise, having larger values of MAPE and false switches and decreasing the number of true switches.

Once more, the situation R_1 presents acceptable metrics, having only 2 false switches since there is no switch from model M_1^c to M_2^c at the beginning. Aside from that, its curve is quite similar with the curve of R_0 . This case also happened for Test A, which indicates that the values of noise and disturbance of R_1 are acceptable for a good performance of the control system.

For situation R_3 , as previously, the switches "stagnates" in the hysteresis condition.

Table 9.6: Evaluation metrics for all the simulations performed in Test C.

Algorithm	N_c	Test	MAPE [%]	True Switch	False Switch	τ_{min} [days]	τ_{mean} [days]	τ_{max} [days]
K-Means	6	-	3.0119	4/4	0	0.4	38.58	119.1
		$\tau_D = 0$	3.0151	4/4	0	0.4	38.58	119.1
		$\tau_D = 75$	3.0124	4/4	0	0.4	49.69	119.4
		$\Delta\theta_{PS} = 50\%$	2.9748	4/4	0	0.4	38.7	119.4
		$\Delta\theta_{PS} = 150\%$	3.1118	4/4	0	0.4	37.74	115.6
		$\Delta\theta_{PS} = 250\%$	5.2044	4/4	0		39.85	121.8
		$n = 0.1, d = 10^{-4}$	3.0386	2/4	1	27	76.11	125.2
		$n = 1, d = 10^{-3}$	3.0474	3/4	3	0.4	20.45	33.8
	12	$n = 10^3, d = 1$	21.6715	1/4	0	0.4	0.4	0.4
Complete Linkage	6	-	3.0253	3/7	5	0.4	13.2	28.8
	12	-	3.0192	2/10	8	28.8	29.6	30.4

10

Conclusions and Future Work

Contents

10.1 Work and results analysis	88
10.2 Future Work	89

The aim of this dissertation was to develop a tool for clinical decision-making in mRCC cancer therapy design, using adaptive control techniques combined with unsupervised learning. Having accomplished this goal, some conclusions on the results are drawn in this chapter, as well as an overview of possible future work.

10.1 Work and results analysis

First of all, at the beginning of this master thesis a review of two promising therapies, anti-angiogenesis and immunotherapy, was performed. Aside from that, a new mathematical model of tumor growth was developed, having in consideration mRCC clinical results and the therapies previously mentioned. Subsequently, a patient model was built incorporating organism pharmacological aspects, as Pharmacokinetics (PK), Pharmacodynamics (PD), Drug Resistance (DR) and toxicity, into the developed tumor growth model.

The studies performed on the patient model allowed an analysis of the minimum values of dose, periodicity, and therapy duration for the tumor to be eradicated. It was found that the immunotherapy, when administered alone, cannot eradicate the tumor, on the contrary of anti-angiogenesis. However, the best results were obtained for a combination of both treatments, which indicates a possible synergy.

A feedback system was developed in order to control the patient by analyzing the tumor volume and intervening in the drug rates. This system has the ability of designing three distinct combinations of drugs. These three different therapies result from the tuning of the matrix R of the LQR control algorithm. In this way, at each time instant, the therapy with the least toxicity is chosen, as was intended in this work. This therapy selection is made through a decision software, Pharmacodynamical Simulation, that simulates the patient pharmacological features.

This control framework was adapted to work in environments where the patient characteristics are unknown, that is, where uncertainty in the system to control exists. A MMAC algorithm is then used that joins a controller bank, consisting of several controllers designed for different operating points, with a supervisor that decides instantaneously the best controller to use.

The controllers belonging to the controller bank are chosen through clustering techniques that select, from a data set of N models, N_c key models, each one describing an important class of patient features.

Finally, three distinct tests were performed in order to illustrate the system operation and to analyze its performance. All the tests showed very satisfactory results, not only in terms of treatment efficacy, but also due to the low toxicity levels achieved. In the three situations, without the addition of error in the system, the tumor is eradicated in less than a year and a half, and the toxicity levels are graded between mild and moderate.

The clustering algorithms have impact on the behavior of the control system, since the positioning and the number considered for the key models, *i.e.* the centroids, influence the way the system performs. In particular, with more clusters, and consequently more controllers, the system performance

tends to degrade, since the system does not have the capacity of reacting with the necessary speed. Therefore, one can conclude that the addition of the model clustering to the MMAC brought performance improvements. This conclusion is drawn because clustering main goal was exactly to reduce the numbers of controllers to operate.

Aside from that, the algorithm that showed the best results – k -means with 6 clusters – does not create clusters with a single model, which indicates that the centroids should be positioned in dense areas of models. This situation does not happen for the other method, *viz.* complete linkage, that have clusters in sparse areas of models.

The influence of the immunotherapy on the results is another question to be undertaken, since its concentration is always 150 to 1000 times lower than the anti-angiogenesis concentration. However, as mentioned before, it is believed that the combined therapy can achieve better results.

It was concluded that the dwell time is important in some situations of chattering that can occur but, at the same time, can harm the system when a fast reaction is necessary. Aside from that, what was described regarding the three different scenarios enumerated in Section 6.2.3, was demonstrated in Chapter 9, since Test A is an example of the **Scenario 1**, Test A (with noise and disturbance) is an example of the **Scenario 2**, and, lastly, Tests B and C (both with noise and disturbance) are cases of **Scenario 3**. All the mentioned tests showed great performance, except, as expected, when large values of noise and disturbance were applied, which indicates that the inclusion of the dwell time condition can result in additional stability conditions.

Finally, by adding error, noise and disturbance, the system limits were tested, having thus a good operating margin.

10.2 Future Work

As mentioned before, this work consists of a simulation of a CDSS. Although all the goals were accomplished, additional improvements can be made, ideally, rendering it possible to be applied in experimental or clinical studies.

The utilization of control techniques that allow the use of the non-linear tumor growth model or, the adaptation of the system to use the linear model in different operating points, are two solutions that can be implemented to better describe the patient behavior. Aside from that, this behavior can be also better characterized if more clinical results are used, not only to mRCC, but also to another kinds of cancer. In this way, additional tests could be made as, for example, the influence of the tumor initial conditions, or the patients characteristics on the therapy. Therefore, a direct collaboration with clinical institutions can possibly extend the scope of this work.

The evaluation of the toxicity involved in a therapy can be more precise if mathematical models are used. Since these kind of models were not found in the literature, they were not used. However, their development is suggested since the toxicity is a vital aspect in the therapy design.

The control system developed can be adapted in order to choose the most convenient therapy or mode of administration. For example, the system of offline bolus calculation developed can be

adapted to work in an online mode. Another hypothesis is also the consideration of the use of the CIT or PO, that can also achieve great results. Aside from that, the system can also be adjusted to work with tumor volume readings with fixed periodicities, that better simulate a real scenario.

In terms of the control system, several techniques can be tested in order to obtain the best performance. One of the possible solutions is the use of a bank of fixed models combined with an adaptive one. That is, a model that can adapt its parameters in accordance with the plant input and output, for example, through an identification system or a neuronal network, as proposed in [106]. On the other hand, since the results with the complete clustering were not the best, after the clustering process, the clusters with a single model may be considered as outliers and not as an important class of patients.

With those improvements, the use of the developed system in experimental trials can be closer to becoming a reality.

Bibliography

- [1] J. Ferlay, I. Soerjomataram, M. Ervik, R. Dikshit, S. Eser, C. Mathers, M. Rebelo, D. Parkin *et al.*, “Globocan 2012 v1.0, cancer incidence and mortality worldwide,” 2013, accessed on 2016 Nov 15, 17h39. [Online]. Available: <http://globocan.iarc.fr>
- [2] F. Bray, A. Jemal, N. Grey, J. Ferlay, and D. Forman, “Global cancer transitions according to the Human Development Index (2008-2030): a population-based study,” *Lancet Oncol.* 2012, vol. 13, no. 8, pp. 790–801, 2012.
- [3] A. Jemal, F. Bray, M. M. Center, J. Ferlay, E. Ward, and D. Forman, “Global Cancer Statistics,” *CA Cancer J Clin.*, vol. 61, no. 2, pp. 69–90, 2011.
- [4] “World Cancer Report 2014,” International Agency for Research on Cancer, WHO, 2014.
- [5] F. Biemar and M. Foti, “Global progress against cancer - challenges and opportunities,” *Cancer Biology and Medicine* 2013, vol. 10, pp. 183–186, 2013.
- [6] V. G. Brichard and D. Lejeune, “GSK’s antigen-specific cancer immunotherapy programme: Pilot results leading to Phase III clinical development,” *Vaccine*, vol. 25, no. 2, pp. B61–B71, 2007.
- [7] R. Munagala, P. Aqil, and R. C. Oupta, “Promising molecular targeted therapies in breast cancer,” *Indian J Pharmacol.*, vol. 43, no. 3, pp. 236–45, 2011.
- [8] L. Bombardelli and A. Berns, “The steady progress of targeted therapies, promising advances for lung cancer,” *Ecancermedicalscience*, vol. 10, no. 638, 2016.
- [9] A. P. Engelbrecht, *Computational Intelligence: An Introduction*, 2nd ed. Wiley, 2007.
- [10] M. R. AlRashidi and M. E. El-Hawary, “Applications of computational intelligence techniques for solving the revived optimal power flow problem,” *Electr. PowerSyst. Res.*, vol. 79, no. 4, pp. 694–702, 2009.
- [11] G. Cosma and G. Acampora, “A computational intelligence approach to efficiently predicting review ratings in e-commerce,” *Applied Soft Computing*, vol. 44, pp. 153–162, 2016.
- [12] L. N. de Castro and J. Timmis, *Artificial Immune Systems: A New Computational Intelligence Approach*, 1st ed. Springer Science & Business Media, 2002.

- [13] K. V. Varma, A. A. Rao, T. S. M. Lakshmi, and P. N. Rao, "A computational intelligence approach for a better diagnosis of diabetic patients," *Comput. Eletr. Eng.*, vol. 40, no. 5, pp. 1758–1765, 2014.
- [14] R. Da, *Computational Intelligence in Complex Decision Making Systems*, 1st ed. Springer Science & Business Media, 2010.
- [15] P. P. Reid, W. D. Compton, J. H. Grossman, and G. Fanjiang, *Building a Better Delivery System: A New Engineering/Health Care Partnership*, 1st ed. National Academies Press, 2005.
- [16] T. Kremmel, J. Kubalík, and S. Biffl, "Software project portfolio optimization with advanced multiobjective evolutionary algorithms," *Appl. Soft Comput.*, vol. 11, no. 1, pp. 1416–1426, 2011.
- [17] P. Berke and N. Stubbs, "Automated decision support systems for hurricane mitigation planning," *Simulations*, vol. 53, no. 3, pp. 101–109, 1989.
- [18] E. S. Bakhoun and D. C. Brown, "An automated decision support system for sustainable selection of structural materials," *Int. J. Sustain. Eng.*, vol. 8, no. 2, pp. 80–92, 2014.
- [19] S. Leatherman, D. Berwick, D. Iles, L. S Lewin, F. Davidoff, T. Nolan, and M. Bisognano, "The Business Case For Quality: Case Studies And An Analysis," *Health affairs (Project Hope)*, vol. 22, no. 2, pp. 17–30, 2003.
- [20] D. Fone, S. Hollinghurst, J. M. F. Temple, and S. R. Palmer, "Systematic review of the use and value of computer simulation modelling in population health and health care delivery," *Journal of Public Health Medicine*, vol. 25, no. 4, pp. 325–335, 2003.
- [21] J. Fox, A. Glowinski, C. Gordon, S. Hajnal, and M. O'Neil, "Logic engineering for knowledge engineering: design and implementation of the Oxford System of Medicine," *Artificial Intelligence in Medicine*, vol. 2, pp. 323–339, 2003.
- [22] D. L. Hunt, R. B. Haynes, and S. E. Hanna, "Effects of computer-based clinical decision support systems on physician performance and patient outcomes: a systematic review," *JAMA*, vol. 280, no. 15, pp. 1339–46, 1998.
- [23] A. Garg, N. Adhikari, H. McDonald, M. P. Rosas-Arellano, P. Devereaux, J. Beyene, J. Sam, and R. Haynes, "Effects of computerized clinical decision support systems on practitioner performance and patient outcomes: a systematic review," *JAMA*, vol. 293, no. 10, pp. 1223–38, 2005.
- [24] V. F. Reyna, W. L. Nelson, P. K. Han, and M. P. Pignone, "Decision Making and Cancer," *American Psychologist*, vol. 70, no. 2, pp. 105–118, 2005.
- [25] P. Knaup, T. Wiedemann, A. Bachert, U. Creutzig, R. Haux, and F. Schilling, "Eficiency and safety of chemotherapy plans for children: CATIPO - nationwide approach," *Artificial Intelligence in Medicine*, vol. 24, pp. 229–242, 2002.

- [26] B. Bonan, N. Martelli, M. Berhoune, L. A. Vidal, E. Sahin, and P. Prognon, “FabAct®: a decision-making tool for the anticipation of the preparation of anticancer drugs,” *J. Eval. Clin. Pract.*, vol. 16, no. 6, pp. 1129–35, 2010.
- [27] J. Bury, C. Hurt, A. Roy, L. Cheesman, M. Bradburn, S. Cross, J. Fox, and V. Saha, “LISA: a web-based decision-support system for trial management of childhood acute lymphoblastic leukaemia,” *Br. J. Haematol.*, vol. 129, no. 6, pp. 746–54, 2005.
- [28] H. Sbeity and R. Younes, “Review of Optimization Methods for Cancer Chemotherapy Treatment Planning,” *J. Comput. Sci. Syst. Biol.*, vol. 8, pp. 074–095, 2015.
- [29] S. Shackney, *Tumor growth, cell cycle kinetics, cancer treatment*, 1st ed. McGraw Hill, 1993.
- [30] R. Pearl, *Studies in Human Biology*, 1st ed. Williams & Wilkins, 1924.
- [31] B. Gompertz, “On the Nature of the Function Expressive of the Law of Human Mortality, and on a New Mode of Determining the Value of Life Contingencies,” *Philosophical Transactions of the Royal Society of London*, vol. 115, pp. 513–583, 1825.
- [32] B. Ribba, E. Watkin, M. Tod, P. Girard, E. Grenier, B. You, E. Giraudo, and G. Freyer, “A model of vascular tumour growth in mice combining longitudinal tumour size data with histological biomarkers.” *Eur. J. Cancer.*, vol. 47, no. 3, pp. 479–90, 2011.
- [33] H. Sbeity and R. Younes, “Quantitative laws in metabolism and growth,” *Q Rev Biol.*, vol. 32, no. 3, pp. 217–31, 1957.
- [34] A. R. A. Anderson and M. A. J. Chaplain, “Continuous and discrete mathematical models of tumor induced angiogenesis,” *Bull. Math. Biol.*, vol. 60, no. 5, pp. 857–899, 1998.
- [35] J. Xu, G. Vilanova, and H. Gomez, “A Mathematical Model Coupling Tumor Growth and Angiogenesis,” *PLoS ONE*, vol. 11, no. 2, p. e0149422, 1825.
- [36] D. McElwain and L. Morris, “Apoptosis as a volume loss mechanism in mathematical models of solid tumor growth,” *Mathematical Biosciences*, vol. 39, no. 1, pp. 147–157, 1978.
- [37] V. A. Kuznetsov and G. D. Knott, “Modeling Tumor Regrowth and Immunotherapy,” *Mathematical and Computer Modelling*, vol. 33, pp. 1275–1287, 2001.
- [38] A. R. Kansal, S. Torquato, G. Harshiv, E. A. Chiocca, and T. Deisboeck, “Simulated Brain Tumor Growth Dynamics Using a Three-Dimensional Cellular Automaton,” *Journal of Theoretical Biology*, vol. 203, no. 4, pp. 367–382, 2000.
- [39] P. Bonate, *Pharmacokinetic-Pharmacodynamic Modeling, Simulation*, 1st ed. Springer, 2006.
- [40] L. Rosso, C. S. Brock, J. M. Gallo, A. Saleem, P. M. Price, F. E. Turkheimer, and E. O. Aboagye, “A New Model for Prediction of Drug Distribution in Tumor and Normal Tissues: Pharmacokinetics of Temozolomide in Glioma Patients,” *Cancer Res.*, vol. 69, no. 1, pp. 120–7, 2009.

- [41] S. Goutellea, M. Maurinc, F. Rougierb, X. Barbautb, L. Bourguignona, M. Ducherb, and P. Mairea, “The Hill equation: a review of its capabilities in pharmacological modelling,” *Fundam Clin Pharmacol.*, vol. 22, no. 6, pp. 633–48, 2009.
- [42] D. E. Mager and W. J. Jusko, “Pharmacodynamic modeling of time-dependent transduction systems,” *Clin. Pharmacol. Ther.*, vol. 70, pp. 210–6, 2010.
- [43] J. H. Goldie and A. J. Coldman, “Quantitative model for multiple levels of drug resistance in clinical tumors,” *Cancer Treat. Rep.*, vol. 67, no. 10, pp. 923–31, 1983.
- [44] T. L. Jackson and H. M. Byrne, “A mathematical model to study the effects of drug resistance and vasculature on the response of solid tumors to chemotherapy,” *Mathematical Biosciences*, vol. 164, no. 1, pp. 17–38, 2000.
- [45] G. W. Swan and T. L. Vincent, “Optimal control analysis in the chemotherapy of IgG multiple myeloma,” *Bulletin of Mathematical Biology*, vol. 39, no. 3, pp. 317–337, 1977.
- [46] H. Schättler and U. Ledzewicz, *Optimal Control for Mathematical Models of Cancer Therapies*, 1st ed. Springer, 2015.
- [47] S. Zietz and C. Nicolini, “Mathematical approaches to optimization of cancer chemotherapy,” *Bulletin of Mathematical Biology*, vol. 41, no. 3, pp. 305–324, 1979.
- [48] D. V. Caiado and J. M. Lemos, “Optimal Control for Cancer Therapy Design,” *23rd Mediterranean Conference on Control and Automation*, 2015.
- [49] J. A. F. Jr., J. L. Eiseman, and R. S. Parker, “A Nonlinear Model Predictive Control Algorithm for Breast Cancer Treatment,” *IFAC Proceedings Volumes*, vol. 37, no. 9, pp. 929–940, 2004.
- [50] H. G. Silva, J. M. Lemos, and B. M. D. da Costa, “Adaptive predictive control based therapy of bone marrow cancer,” in *Preprints, 12th IFAC Int. Work. on Adaptation and Learning in Control and Signal Proc., June 29 - July 1, 2016. Eindhoven, The Netherlands.* IFAC, Jun. 2016, pp. 1–6.
- [51] N. Babaei and M. U. Salamci, “Personalized drug administration for cancer treatment using Model Reference Adaptive Control,” *J. Theor. Biol.*, vol. 371, pp. 24–44, 2015.
- [52] C. Yu, R. J. Roy, H. Kaufman, and B. W. Bequette, “Multiple-model adaptive predictive control of mean arterial pressure and cardiac output,” *IEEE Trans. Biomed. Eng.*, vol. 39, no. 8, pp. 765–78, 1992.
- [53] W. He, H. Kaufman, and R. Roy, “Multiple model adaptive control procedure for blood pressure control,” *IEEE Trans. Biomed. Eng.*, vol. 33, no. 1, pp. 10–9, 1986.
- [54] J. M. Lemos, H. Magalhães, T. Mendonça, and R. Dionísio, “Control of neuromuscular blockade in the presence of sensor faults,” *IEEE Trans. Biomed. Eng.*, vol. 52, no. 11, pp. 1902–11, 2005.

- [55] T. Mendonça, J. M. Lemos, H. Magalhães, P. Rocha, and S. Esteves, “Drug delivery for neuromuscular blockade with supervised multimodel adaptive control,” *IEEE Trans. Control System Technology*, vol. 17, no. 6, pp. 1237–1244, 2009.
- [56] P. Oliveira, J. P. Hespanha, J. M. Lemos, and T. Mendonça, “Supervised multi-model adaptive control of neuromuscular blockade with off-set compensation,” in *Proceedings of the European Control Conference 2009 , Budapest, Hungary, August 23-26, 2009*, Aug. 2009.
- [57] P. Maybeck and R. Stevens, “Reconfigurable flight control via multiple model adaptive control methods,” *IEEE Trans. on Aerospace and Electronic Sys.*, vol. 27, no. 3, pp. 470 – 480, 1990.
- [58] J. M. Lemos, P. S. Oliveira, J. S. Marques, and T. F. Mendonça, “Clustering in supervised multi-model adaptive control applied to neuromuscular blockade,” in *Proceedings of the 15th IFAC Symposium on System Identification Saint-Malo, France, July 6-8, 2009*. IFAC, Jul. 2009.
- [59] P. Bashivan, A. Fatehi, and E. Peymani, “Multiple-model control of ph neutralization plant using the som neural networks,” in *India Conference. INDICON 2008*. IEEE, Dec. 2008.
- [60] P. Rosa, T. Simão, J. M. Lemos, and C. Silvestre, “Multiple-model adaptive control of an air heating fan using set-valued observers,” in *Preprints of the 2012 20th Mediterranean Conference on Control & Automation (MED), Barcelona, Spain, July 3-6, 2012*. WeC3.3, Jul. 2012.
- [61] G. H. Heppner and F. R. Miller, “The Cellular Basis of Tumor Progression,” *International Review of Cytology*, vol. 177, pp. 1–56, 1998.
- [62] D. E. Gerber, “Targeted therapies: a new generation of cancer treatments,” *Am. Fam. Physician.*, vol. 77, no. 3, pp. 311–9, 2008.
- [63] E. L. Spurell and M. Lockley, “Adaptive immunity in cancer immunology and therapeutics,” *Ecancermedicalscience*, vol. 8, no. 441, 2014.
- [64] C. A. Janeway, J. P. Travers, M. Walport, and M. J. Shlomchik, *Immunobiology: the immune system in health and disease*. Garland Science, 2005.
- [65] D. S. Chen and I. Mellman, “Oncology meets immunology: The cancer-immunity cycle,” *Immunity*, vol. 39, no. 1, pp. 1–10, 2013.
- [66] P. E. Hughes, S. Caenepeel, and L. C. Wu, “Targeted therapy and checkpoint immunotherapy combinations for the treatment of cancer,” *Immunity*, vol. 37, no. 7, pp. 462–476, 2016.
- [67] S. A. Rosenberg, J. C. Yang, and N. P. Restifo, “Cancer immunotherapy: moving beyond current vaccines,” *Nature Medicine*, vol. 10, pp. 909–915, 2004.
- [68] L. M. Weiner, R. Surana, and S. Wang, “Antibodies and cancer therapy: versatile platforms for cancer immunotherapy,” *Nat. Rev. Immunol.*, vol. 10, no. 5, pp. 317–327, 2010.
- [69] C. Fellner, “Ipilimumab (yervoy) prolongs survival in advanced melanoma,” *Pharmacy and Therapeutics*, vol. 37, no. 9, pp. 503–511, 2012.

- [70] H. X. Chen, "Expanding the clinical development of bevacizumab," *The Oncologist*, vol. 9, no. 1, pp. 27–35, 2004.
- [71] E. Lanitis, M. Irving, and G. Coukos, "Targeting the tumor vasculature to enhance t cell activity," *Immunology*, vol. 33, pp. 55–63, 2015.
- [72] J. D. Peske, A. B. Woods, and V. H. Engelhard, "Control of cd8 t-cell infiltration into tumors by vasculature and microenvironment," *Adv. Cancer Res.*, vol. 128, pp. 263–307, 2015.
- [73] B. Steege, C. Baeten, V. Thijssen, S. Satijn, I. Verhoeven, H. Hillen, J. Wagstaff, and A. Griffioen, "Angiogenic profile of breast carcinoma determines leukocyte infiltration," *Clin. Cancer Res.*, vol. 10, no. 21, pp. 7171–8, 2004.
- [74] L. Zhang, J. R. Conejo-Garcia, D. Katsaros, P. A. Gimotty, M. Massobrio, G. Regnani, A. Makrigiannakis, H. Gray *et al.*, "Intratumoral t cells, recurrence, and survival in epithelial ovarian cancer," *N. Engl. J. Med.*, vol. 348, no. 3, pp. 203–13, 2003.
- [75] D. Gabrilovich, H. Chen, K. R. Girgis, H. T. Cunningham, G. M. Meny, S. Nadaf, D. Kavanaugh, and D. P. Carbone, "Production of vascular endothelial growth factor by human tumors inhibits the functional maturation of dendritic cells," *Nature Medicine*, vol. 2, pp. 1096 – 1103, 1996.
- [76] T. Voron, O. Colussi, E. Marcheteau, S. Pernot, M. Nizard, A.-L. Pointet, S. Latreche, S. Bergaya *et al.*, "Vegf-a modulates expression of inhibitory checkpoints on cd8 +t cells in tumors," *J. Exp. Med.*, vol. 212, no. 2, pp. 139–148, 2015.
- [77] M. Terme, S. Pernot, E. Marcheteau, F. Sandoval, N. Benhamouda, O. Colussi, O. Dubreuil, A. Carpentier *et al.*, "Vegfa-vegfr pathway blockade inhibits tumor-induced regulatory t-cell proliferation in colorectal cancer," *Cancer Res.*, vol. 73, no. 2, pp. 539–49, 2013.
- [78] K. Garber, "Promising early results for immunotherapy-antiangiogenesis combination," *J. Natl. Cancer Inst.*, vol. 106, no. 11, 2014.
- [79] J. Wallin, J. Bendell, R. Funke, M. Sznol, K. Korski, S. Jones, G. Hernandez, J. Mier *et al.*, "Atezolizumab in combination with bevacizumab enhances antigen-specific t-cell migration in metastatic renal cell carcinoma," *Nat. Commun.*, vol. 7, no. 12624, 2016.
- [80] A. Amin, E. R. Plimack, J. R. Infante, M. S. Ernstooff, B. I. Rini, D. F. McDermott, J. J. Knox, S. K. Pal *et al.*, "Nivolumab (anti-pd-1; bms-936558, ono-4538) in combination with sunitinib or pazopanib in patients (pts) with metastatic renal cell carcinoma (mrcc)." *J. Clin. Oncology*, vol. 32, no. 15_suppl, pp. 5010–5010, 2014.
- [81] B. I. Rini, S. Halabi, J. E. Rosenberg, W. M. Stadler, D. A. Vaena, L. Archer, J. N. Atkins, J. Picus *et al.*, "Phase iii trial of bevacizumab plus interferon alfa versus interferon alfa monotherapy in patients with metastatic renal cell carcinoma: Final results of calgb 90206," *Cancer Res.*, vol. 28, no. 13, pp. 2137–43, 2010.

- [82] F. S. Hodi, D. Lawrence, C. Lezcano, X. Wu, J. Zhou, T. Sasada, W. Zeng, A. Giobbie-Hurder *et al.*, “Bevacizumab plus ipilimumab in patients with metastatic,” *Cancer Immunol. Res.*, vol. 2, no. 7, pp. 632–642, 2014.
- [83] A. Takahashi, H. Sasaki, S. J. Kim, K. ichi Tobisu, T. Kakizoe, T. Tsukamoto, Y. Kumamoto, T. Sugimura, and M. Terada, “Markedly increased amounts of messenger rnas for vascular endothelial growth factor and placenta growth factor in renal cell carcinoma associated with angiogenesis,” *Cancer Res.*, vol. 54, no. 15, pp. 4233–4237, 1994.
- [84] P. Hahnfeldt, D. Panigrahy, J. Folkman, and L. Hlatky, “Tumor Development under Angiogenic Signalling: A Dynamical Theory of Tumor Growth, Treatment Response, and Postvascular Dormancy,” *Cancer Research*, vol. 59, pp. 4770–4775, 1999.
- [85] N. Stepanova, “Course of the immune reaction during the development of a malignant tumour,” *Biophysics*, pp. 917–923, 1980.
- [86] U. Ledzewicz, M. S. F. Mosalman, and H. Schättler, “Optimal controls for a mathematical model of tumor-immune interactions under targeted chemotherapy with immune boost,” *Disc. and Cont. Dyn. Sys.-S. B*, vol. 18, no. 4, pp. 1031–1051, 2013.
- [87] M. A. Hedaya, *Basic Pharmacokinetics*, 2nd ed. CRC-Press, 2012.
- [88] J. Lu, R. Bruno, S. Eppler, W. Novotny, B. Lum, and J. Gaudreault, “Clinical pharmacokinetics of bevacizumab in patients with solid tumors,” *Cancer Chem. Pharm.*, vol. 62, no. 5, pp. 779–86, 2008.
- [89] M. Stroh, H. Winter, M. Marchand, L. Claret, S. Eppler, J. Ruppel, O. Abidoye, S. L. Teng, and other, “The clinical pharmacokinetics and pharmacodynamics of atezolizumab in metastatic urothelial carcinoma,” *Clin. Pharmacol. Ther.*, vol. 102, pp. 305–312, 2016.
- [90] H. Mizugaki, N. Yamamoto, H. Murakami, H. Kenmotsu, Y. Fujiwara, Y. Ishida, T. Kawakami, and T. Takahashi, “Phase i dose-finding study of monotherapy with atezolizumab, an engineered immunoglobulin monoclonal antibody targeting pd-l1, in japanese patients with advanced solid tumors,” *Invest New Drugs*, vol. 34, pp. 596–603, 2016.
- [91] L. Liu, H. Yu, X. Huang, H. Tan, S. Li, Y. Luo, L. Zhang, S. Jiang *et al.*, “A novel engineered vegf blocker with an excellent pharmacokinetic profile and robust anti-tumor activity,” *BMC Cancer*, vol. 15, p. 170, 2015.
- [92] J. K. Leighton, “Pharmacology review - tecentriq (atezolizumab),” 2016, accessed on 2017 Feb 19, 00h39. [Online]. Available: <https://www.accessdata.fda.gov/>
- [93] M. M. Gottesman, “Mechanisms of cancer drug resistance,” *Annu. Rev. Med.*, vol. 53, pp. 615–27, 2002.

- [94] S. Loges, T. Schmidt, and P. Carmeliet, "Mechanisms of resistance to anti-angiogenic therapy and development of third-generation anti-angiogenic drug candidates," *Genes Cancer.*, vol. 1, no. 1, pp. 12–25, 2010.
- [95] S. Kelderman, T. N. Schumacher, and J. B. Haanen, "Acquired and intrinsic resistance in cancer immunotherapy," *Mol. Oncol.*, vol. 8, no. 6, pp. 1132–9, 2014.
- [96] J. M. Lemos, J. V. Pinheiro, and S. Vinga, "A nonlinear mpc approach to minimize toxicity in hiv-1 infection multi-drug therapy," in *10th Portuguese Conference on Automatic Control. CONTROLO'2012*, Jul. 2012, pp. 315–320.
- [97] F. Elice and F. Rodeghiero, "Side effects of anti-angiogenic drugs," *Thrombosis Research 2012*, vol. 129, no. 1, pp. 50–53, 2012.
- [98] J. S. Weber, J. C. Yang, M. B. Atkins, and M. L. Disis, "Toxicities of immunotherapy for the practitioner," *J. Clin. Oncol.*, vol. 33, no. 18, pp. 2092–2099, 2015.
- [99] "Common terminology criteria for adverse events (ctcae)," 2009, u.S. Dep. of Health and Human Service. Accessed on 2017 Jun 10, 9h11. [Online]. Available: <https://evs.nci.nih.gov/ftp1/CTCAE>
- [100] "Highlights of prescribing information - tecentriq (atezolizumab)," 2016, genentech Inc. Accessed on 2017 Fev 1, 13h10. [Online]. Available: <https://www.gene.com>
- [101] "Highlights of prescribing information - avastic (bevazizumab)," 2014, genentech Inc. Accessed on 2017 Fev 2, 16h19. [Online]. Available: <https://www.gene.com>
- [102] F. L. Lewis, D. Vrabie, and V. L. Syrmos, *Optimal Control*, 3rd ed. Wiley, 2012.
- [103] K. Ogata, *Modern Control Engineering*, 5th ed. Prentice-Hall, 2009.
- [104] G. F. Franklin, J. D. Powell, and A. Emami-Naeini, *Feedback Control of Dynamic Systems*, 7th ed. Pearson, 2015.
- [105] A. S. Morse, "Supervisory control of families of linear set-point controllers - part 1: Exact matching," *IEEE Trans. on Aut. Control*, vol. 41, no. 10, pp. 1413–1431, 1996.
- [106] K. S. Narendra, J. Balakrishnan, and M. K. Ciliz, "Adaptation and learning using multiple models, switching, and tuning," *IEEE Control Systems*, vol. 15, no. 3, pp. 37–51, 1995.
- [107] J. M. Lemos, R. Neves-Silva, and J. M. Igreja, *Adaptive Control of Solar Energy Collector Systems*, 1st ed. Springer, 2014.
- [108] J. P. Hespanha, D. Liberzon, and A. S. Morse, "Overcoming the limitations of adaptive control by means of logic-based switching," *Systems & Control Letters*, vol. 49, no. 1, pp. 49–65, 2003.
- [109] K. Narendra and J. Balakrishnan, "Improving transient response of adaptive control systems using multiple models and switching," *IEEE Trans. on Auto. Control*, vol. 39, no. 9, pp. 1861–1866, 1994.

- [110] ——, “Intelligent control using fixed and adaptive models,” in *Proceedings of 1994 33rd IEEE Conference on Decision and Control, Lake Buena Vista, FL, USA*. IEEE, Dec. 1994.
- [111] J. M. Lourenço and J. M. Lemos, “Predictive adaptive control of plants with online structural changes based on multiple models,” *Int. J. of Adap. Cont. and Sig. Proc.*, vol. 22, no. 8, 2008.
- [112] R. Middleton, G. C. Goodwin, D. Hill, and D. Mayne, “Design issues in adaptive control,” *IEEE Trans. on Aut. Control*, vol. 33, pp. 50 – 58, 02 1988.
- [113] A. S. Morse, D. Q. Mayne, and G. C. Goodwin, “Applications of hysteresis switching in parameter adaptive control,” *IEEE Trans. on Aut. Control*, vol. 37, no. 9, pp. 1343–1354, 1992.
- [114] A. Morse, “Supervisory control of families of linear set-point controllers - part 1: Exact matching,” *IEEE Transactions on Automatic Control*, vol. 41, no. 10, pp. 1413–1431, 1996.
- [115] ——, “Supervisory control of families of linear set-point controllers. 2. robustness,” *IEEE Transactions on Automatic Control*, vol. 42, no. 11, pp. 1500–1515, 1997.
- [116] J. Hespanha, D. Liberzon, A. S. Morse, B. D. O. Anderson, T. S. Brinsmeadand, and F. D. Bruyne, “Multiple model adaptive control. part2: switching,” *Int. J. Robust Nonlinear Control*, vol. 11, no. 5, pp. 479–496, 2001.
- [117] A. Loría and E. Panteley, “Uniform exponential stability of linear time-varying systems: revisited,” *Systems & Control Letters*, vol. 47, no. 1, pp. 13–24, 2002.
- [118] M. C. Turner and D. J. Walker, “Modified linear quadratic bumpless transfer,” in *Proceedings of the 1999 American Control Conference*, vol. 4, 1999, pp. 2285–2289.
- [119] R. Hanus, M. Kinnaert, and J. L. Henrotte, “Conditioning technique, a general anti-windup and bumpless transfer method,” *Automatica*, vol. 23, no. 6, pp. 729–739, 1987.
- [120] K. J. Åström and T. Hägglund, *Advanced PID Control*, 1st ed. ISA, 2006.
- [121] K. J. Åström and B. Wittenmark, *Computer-Controlled Systems: Theory and Design*, 3rd ed. Pearson, 1997.
- [122] P. Oliveira, “Controlo com Múltiplos Modelos do Bloqueio Neuromuscular,” Master’s thesis, Instituto Superior Técnico, Portugal, 2008.
- [123] A. L. Coito, B. M. D. da Costa, and J. M. Lemos, “Model identification for control of patients subject to general anesthesia,” INESC-ID, Tech. Rep. 30, Jun. 2011.
- [124] B. D. O. Anderson, T. S. Brinsmeadand, F. D. Bruyne, J. Hespanha, D. Liberzon, and A. S. Morse, “Multiple model adaptive control. part1: Finite controller coverings,” *Int. J. Robust Nonlinear Control*, vol. 10, pp. 909–929, 2000.
- [125] A. K. El-Sakkary, “The gap metric: Robustness of stabilization of feedback systems,” *IEEE Trans. on Aut. Control*, vol. 30, no. 3, pp. 240–247, 1995.

- [126] G. Vinnicombe, "Frequency domain uncertainty and the graph topology," *IEEE Trans. on Aut. Control*, vol. 38, no. 9, pp. 1371–1383, 1993.
- [127] J. MacQueen, "Some methods for classification and analysis of multivariate observations," *Proc. Fifth Berkeley Symp. on Math. Statist. and Prob.*, vol. 1, pp. 281–297, 1967.
- [128] B. King, "Step-wise clustering procedures," *J. of the Amer. Sta. Ass.*, vol. 62, no. 317, pp. 86–101, 1967.
- [129] J. Y. Lee, C. K. Kim, D. Choi, and B. K. Park, "Volume doubling time and growth rate of renal cell carcinoma determined by helical ct: a single-institution experience," *Eur Radiol*, vol. 18, pp. 731–737, 2008.

A

Approximation of Patient Model to Metastatic Renal Cell Carcinoma

In order to approximate the patient model to clinical values, some clinical results of mRCC were used - Tables A.1 and A.2. This information include: tumor's initial volume, growth rate of 30 patients with mRCC [129], and the variation of the sum of the tumor largest diameters, for 10 patients in 9 different time instants [79].

First of all, the model was adapted taking into consideration the initial conditions of the clinical results. According to the values in [129], tumor's initial volume were between 0.3 cm^3 and 494.7 cm^3 , with mean 28.7 cm^3 and median 5.2 cm^3 . Since 70 % of the initial volumes belong to the range $[0.3; 10] \text{ cm}^3$, this interval was considered as acceptable for being the tumor's initial volume in the patient model. Aside from that, the average growth rate for the 30 patients was $19.1 \text{ cm}^3/\text{year}$.

Using the previous information, the parameters of the general tumor growth model composed by equations (2.7),(2.8) and (2.9) were adjusted, except the sensibilities η and κ . In this way, in absence of therapy, the model can behave as the referred clinical results.

The tumor's diameter variation obtained from [79] allows to adapt the model response to treatment. However, it is intended to calculate the volume variations from the diameter variation, which implies the consideration of the shape of the tumor as a sphere.

By having the information of the reaction of all the patients to treatment, a behavior window can be established if one consider the best and the worst therapy response from the sample. It needs to be pointed out that this sample does not include an outlier patient, whose treatment was discontinued after less than 3 months due to his death.

Using the information of the 9 distinct time instants, two fitted 4th order curves were calculated, as illustrated in Figure A.1.

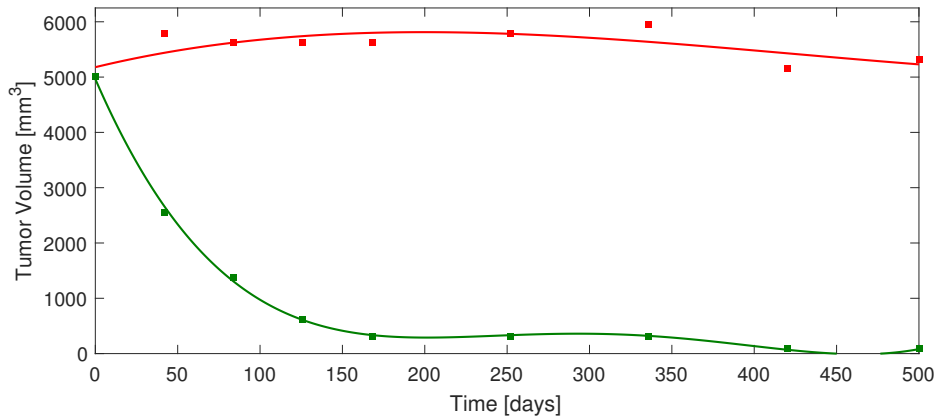


Figure A.1: Tumor behavior window according to [79] for $V_0 = 5000 \text{ mm}^3$. Maximum curve with a fit.

In the circumstance of the clinical results being considered in this work, a therapy of 15 mg/kg of bevacizumab and 20 mg/kg of atezolizumab with periodicities $d_g = d_i = 21 \text{ days}$, was administered to patients. This means that, by considering exactly the same therapy and varying the tumor's initial volume in the interval previously defined, the therapy sensibilities η and κ can be adjusted. In this way, using the fitted curves as the minimum and the maximum allowed volume, results $\eta \in [1.35, 11.25]$ and $\kappa \in [0.1, 0.5]$.

Table A.1: Values of tumor's initial volume and volume growth described in [129].

Tumor Initial Volume [cm^3]	Volume Growth Rate [$cm^3/year$]
0.8	0.6
2.2	0.61
2.3	3.1
4.5	3.2
2.6	2.9
8.6	2.7
99.1	89.1
1.3	2.2
74.5	36.0
5.2	15.9
6.7	6.9
11.1	15.2
2.0	1.5
17.9	9.1
2.2	0.6
2.4	0.8
2.2	1.3
5.2	1.8
25.7	17.7
1.6	2.6
11.8	3.4
0.3	0.7
7.1	1.6
9.9	15.6
7.4	5.8
16.8	65.3
30.9	56.8
494.7	203.8
1.0	1.1
2.0	3.9

Table A.2: Values of the diameter variation for patients with the best and the worst tumor response with the respective time instants. Information described in [79].

Time Instant [days]	Best Scenario Variations [%]	Worst Scenario Variations [%]
0	0	0
42	-20	5
84	-35	4
126	-50	4
168	-60	4
252	-60	5
336	-60	6
420	-75	1
500	-75	1

